Studies of the Atmosphere Using Aerospace Probes - 1975

A REPORT

from the space science and engineering center
the university of wisconsin-madison
madison, wisconsin

Studies of the Atmosphere Using
Aerospace Probes - 1975

STUDIES OF THE ATMOSPHERE

USING AEROSPACE PROBES

1975

Annual Report, NOAA Grant 04-3-158-61

The research reported in this document has been supported by the National Oceanic and Atmospheric Administration.

August 1976

Published for the

Space Science and Engineering Center

by the

University of Wisconsin Press

Published 1976
The University of Wisconsin Press
Box 1379, Madison, Wisconsin 53701

The University of Wisconsin Press, Ltd.
70 Great Russell Street, London

First Printing

Printed in the United States of America

ISBN 0-299-97056-6

This work is a result of research sponsored by the NOAA National Environmental Satellite Service, Department of Commerce, under Grant No. 04-3-158-61. The U.S. Government is authorized to produce and distribute reprints for governmental purposes notwithstanding any copyright notation that may appear hereon.

Correspondence concerning editorial matters should be addressed to
Space Science and Engineering Center
University of Wisconsin
1225 West Dayton Street
Madison, Wisconsin 53706

Orders for copies of this report should be addressed to
The University of Wisconsin Press.

Principal Investigator: Verner E. Suomi

Contributors: W. R. Barchet

K. G. Bauer

S. Limaye

C. S. Lo

J. A. Young

University of Wisconsin

CONTENTS

PREFACE

Once again I have the opportunity to express my appreciation to the scientists and students who have performed the work and authored the papers presented here. I think I should also point out that the efforts of many persons, in addition to the authors, are actually involved. These papers would not have been written without the help of computer programmers and operators, draftsmen, secretaries, mechanicians, librarians, administrators, and many others.

My thanks to all members of the team and my especial gratitude to the National Oceanic and Atmospheric Administration for the support which makes our work possible.

Verner E. Suomi
Principal Investigator

WIND OBSERVATIONS FROM THE U.S.N.S. VANGUARD DURING GATE PHASE I*

John A. Young

ABSTRACT

The U.S.N.S. Vanguard provided a set of high quality upper-air wind data during GATE which should be uniquely valuable to researchers. The figures in this note are intended to illustrate the excellent vertical resolution and apparent accuracy of these observations, which were obtained by a high precision tracking radar. The examples have been chosen from Phase I when the ship was positioned at the center of the B array (8.5°N, 23.5°W). The natural evolution of some jet and "wave" features is portrayed in detail as a function of height over periods of a few hours and a few days respectively. In addition to possible stratospheric "waves" identified in previous studies, the data show that features with 1 km vertical wavelengths are present which may be associated with planetary inertia-gravity waves.

1. INTRODUCTION

The U.S.N.S. Vanguard, a large N.A.S.A. satellite tracking ship, participated in all three phases of GATE with a small (8-10) meteorological crew. Its primary contribution was to provide a series of high resolution, accurate radar wind observations in the B array. The quality of these observations was excellent, and they represent a uniquely useful data set for basic GATE research and intercomparison studies. Examples of highly accurate wind profile sequences have been presented in the literature previously (eg. Weinstein, et al., 1966; DeMandel and Scoggins, 1967). However, the present data is unique in that it was obtained on a ship platform as part of a major integrated field experiment. The purposes of this note are (a) to present examples of the data illustrating the resolution and apparent accuracy of the Vanguard wind data and (b) to give insight into the natural variability of some typical GATE wind features. An appreciation of these char-

*This article appeared in the March 1976 issue of the Monthly Weather Review, Vol. 104, No. 3, published by the American Meteorological Society, Boston.

acteristics should be helpful to scientists utilizing the wind data either directly or indirectly.

Most observations were obtained by tracking a 10-inch aluminum corner reflector attached to the train immediately below the balloon. The C-Band radar has a position accuracy of about 2 m in range and 1×10^{-4} to 5×10^{-4} radians in azimuth. The radar data was combined in the central data processing system with navigation data which utilized satellite fixes and an inertial unit. Three-dimensional balloon motion vectors (relative to a fixed point on the earth) were plotted at 2-s intervals after having been filtered using a 20-s weighted mean (equivalent to about 100 m in altitude).[1] Low level resolution and early acquisition characteristics were improved in some rawin runs by the utilization of 100-gram balloons (515 g lift) and decreasing ballasts provided by leaking milk cartons. During period C (see below) the median altitude for initial radar lock was 150 m for rawins and 280 m for rawinsondes; the lowest altitude was 67 m. Median burst altitude for the rawins and rawinsondes was 14 and 29 km respectively.

The Vanguard was positioned at the center of the B array (Position 1: 8.5°N, 23.5°W) near the NOAA ship Oceanographer from 28 June through 16 July.[2] The wind observations fell into three subperiods during Phase I:

A. Intercomparison Period with Oceanographer (29 June - 4 July)
   A total of 29 rawinsondes and 4 rawins launched by either the Oceanographer or Vanguard were tracked by the Vanguard.
B. Quasi-Operational Period (5 July - 13 July)
   4 rawinsondes were launched and tracked by the Vanguard each day.
C. Special Observation Period (13 July - 16 July)

The cross-equational voyage originally scheduled was cancelled in order that the Vanguard remain at the center of the B array. A

---

[1]An error estimate for 20-s weighted winds can be made as follows: The above figures indicate instantaneous position errors of a few meters for typical balloon ranges; these are reduced by averaging the high-volume radar position estimates over 20-s. When compared with typical 20-s balloon displacements of a few hundred meters, we find the balloon motion errors to be about 1% or less, which are comparable to the values quoted by DeMandel and Scoggins (1967) for high precision radar measurements over Cape Kennedy, Fla. Primary wind errors would thus be associated with aerodynamically induced balloon oscillations.

[2]During Phases II and III the Vanguard was stationed at Position 2 (10°N, 23.5°W) and normally made 8 rawinsonde observations per day.

series of special rawin observations was then established for the last 3.5 days of Phase I. During this time the interval between successive wind observations was 3 h or less; a total of 16 rawins and 17 rawinsondes were tracked.

2. SAMPLE RESULTS

Figures 1-3 show wind profile information with excellent vertical resolution. Traces are taken directly from plots of filtered vectors at 2 s (10 m) intervals and could be smoothed further, if necessary. Alternatively, the original taped data could be used without any smoothing. Features which could be noted in traces such as these include boundary layer wind structure, shear layers at the trade inversion, small-scale structures of convective or gravity wave origin, lower tropospheric wind speed maxima, the upper tropospheric easterly jet, lower stratospheric wave structures, and the stratospheric easterly jet.

The solid trace in Fig. 1 allows comparison of wind direction and speed variations with height in the troposphere and stratosphere. The direction changes indicate a predominance of veering in the lower troposphere; the wind direction changes by 90° throughout an apparent planetary boundary layer of thickness 2.7 km. Backing is indicated in two layers a few thousand feet thick; associated speed maxima are found at nearby levels. Pronounced direction and speed fluctuations were commonly found above the Tropical Easterly Jet (13 km); they represent fluctuating vector fields with vertical wavelengths of about 1-3 km superimposed upon the climatological easterly flow. On some occasions the associated speed profiles indicated a succession of layers with alternately strong and very light winds.

The solid and dotted traces of Fig. 1 show stratospheric profiles 36 h apart. The stratospheric easterlies appear to be strong, uni-directional, and deep. The variability appears to be comparable to that found on the smallest scales in the troposphere.

Figs. 2 and 3 illustrate the replicability of wind speed observations from sequences closely spaced in time. Examples are taken from two successive days; time increments between profiles vary from 1 to 3 h. Differences are thought to primarily represent natural variability rather than observational inaccuracies. Several features of small vertical scale appear to be somewhat persistent, lending qualitative support to their reality. Note, for example, the speed profiles in the layers at 0-3 km and at 5.5-9.0 km in Figs. 2 and 3. Fig. 2 shows the evolution of the

tropospheric easterly jet toward a sharply defined structure from 13 to 15 km; the thin "wave" structures above the jet appear to intensify simultaneously. The jet is seen to persist into the next day (Fig. 3), while the small-scale "waves" (vertical wavelengths of 1 km) give way to a broader feature (3 km wavelength) with larger amplitude (14 m s^{-1} range). Inspection of Fig. 1 (12 GMT 14 July) indicates that these small-scale features are still present above 18 km.

Figs. 4 and 5 place the height-time wind variations in better synoptic perspective. Contours have been smoothed somewhat because the time resolution is often poorer than the height resolution. The smoothing has eliminated fine structures with wavelengths less than about 300 m. The wave structures discussed above have not been smoothed out, but are less obvious due to the relatively large contour intervals of Figs. 4 and 5. Both figures show variations with typical periods in the range 3-5 days. The tendency for tilting contours above 14 km indicates downward phase propagation in the stratosphere; this seems consistent with previous observations of stratospheric waves and the upward propagation of wave energy from the troposphere (Wallace, 1973). This phase propagation seems most clear above 15 km where Figs. 1-3 show the "wave" activity is centered. The clearest example of this propagation seems to be in the u-field through the first week in July.

The easterly jet is often found in the u-field (Fig. 4) near 13 km; its descent in time is accompanied by thickness and intensity changes. Intermediate time periods are marked by light easterlies or even westerlies, lasting on the order of 2 days. The "wave" fluctuations are often associated with reversals in the sense of this wind component.

The v-field (Fig. 5) shows that the meridional wind is usually northward in the upper troposphere (12 km), but its sense is more variable at greater altitudes (18 km). Its fluctuations are strongest near the tropopause, where they account for much of the wind direction changes noted in Fig. 1. The vertical phase propagation is much less distinct than that shown for the u-component in Fig. 4.

The extent to which these fields may be associated with various tropical waves cannot be determined conclusively by this limited study. Nevertheless, some broad comparisons are useful:

1. A large amount of variability appears to be associated with periods of 3-5 days and vertical wavelengths of about 3 km. This seems broadly consistent with observations of mixed Rossby-

gravity waves summarized in Wallace (1973), except that the present scales are smaller by a factor of approximately 2. Madden and Zipser (1970) commented on related "layering" of the v-field during the Line Islands Experiment in the Pacific and noted that the largest wind shears were found in this same altitude range (14-18 km).

2. The shorter wavelengths of about 1 km are not well documented by normal rawinsonde observations, but appear from this data to be significant in the lower stratosphere. Wallace (1973) indicates that planetary inertia-gravity waves would be expected to have these properties and could be identified if higher resolution soundings were available; this Vanguard data may have fulfilled this wish. The wind direction changes shown in Fig. 1 for 12 GMT on 14 July are not inconsistent with this interpretation. Similar mesoscale structures at these altitudes were found by DeMandel and Scoggins (1967) and Weinstein, et al. (1966); the latter speculated that they might be manifestations of "quasi-inertial oscillations."

3. The possible presence of equatorial Kelvin waves in this data is difficult to assess. They would be indicated by fluctuations in only the u-component. Fig. 4 suggests that a slow variation in u, over a long period of 2-3 weeks, may be present, whereas none is apparent in the v-field (Fig. 5). This period is of the same order as that ascribed to Kelvin waves by Wallace (1973). Thus the present data do not rule out the possibility of Kelvin waves.

3. CONCLUDING REMARKS

The examples indicate that the Vanguard wind observations will provide researchers with data of unique reliability and vertical resolution. Its high apparent reliability should be useful in direct intercomparison studies and as a guide in judging questionable data from other sources. A catalogue of Vanguard wind profiles could prove useful as a "quick-look" summary of upper-air winds for the entire GATE period.

The replicability and vertical detail of the observations presented here suggest that synoptically significant wind features existed in layers only a few thousand feet thick during GATE, and that the Vanguard data set resolves these structures well. Thus the data should be useful for (a) documenting boundary layer wind profiles above tethered balloon levels, (b) studying the evolution of jet structures in vertical detail, and (c) defining the behavior of the lower stratospheric "waves."

ACKNOWLEDGMENTS

The author participated as Chief Scientist aboard the Vanguard during Phase I of GATE. His personal thanks go to the dedicated and hard-working members of the meteorological observing crew: Wallace Demaurice and Chris Horseman of NOAA; Joseph Alfieri (U.S.A.F.); and UCAR students Lesley Julian, Donald Norquist, Andrew Sullivan, and Winfield Sylvester. Special thanks go to Station Director Otto Thiele and Captain Harry Anderson, Jr. for their interest and support. The exceptional cooperation of the men and women of the NASA technical staff, the officers, and the marine crew was greatly appreciated.

The author's participation in GATE and subsequent research was funded additionally by NSF Grant GA-38811. Mr. Eueng-nan Yeh assisted in the plotting of duplicate computer output. The U.S.N.S. Vanguard is operated for the National Aeronautics and Space Administration by the Goddard Space Flight Center; we are grateful for the commitment of the ship to the entire experiment.

REFERENCES

DeMandel, R.E. and J.R. Scoggins, 1967: Mesoscale wave motions as revealed by improved wind profile measurements. J. Appl. Met., 6, pp. 617-620.

Madden, R.A., and E.J. Zipser, 1970: Multi-layered structure of the wind over the equatorial Pacific during the Line Islands Experiment. J. Atmos. Sci., 27, pp. 336-343.

Wallace, J.M., 1973: General circulation of the lower tropical lower stratosphere. Reviews of Geophysics and Space Physics, 11, pp. 191-222.

Weinstein, A.I., E.R. Reiter, and J.R. Scoggins, 1966: Mesoscale structure of 11-20 km winds. J. Appl. Met., 5, pp. 49-57.

FIGURE LEGENDS

Figure 1 Sample vertical profiles of wind speed and direction for two separate days. Solid line (12 GMT 14 July 1974) shows detail in the troposphere and stratosphere. Dotted line (00 GMT 13 July 1974) shows stratospheric detail 36 h previously.

Figure 2 Sequence of vertical profiles of wind speed during the day 13 July 1974. Time intervals between observations are 2 or 3 h. The abscissa for each time (identified in parenthesis) is shifted so that the origin is indicated by dashed lines.

Figure 3 Sequence of vertical profiles of wind speed during the day 14 July 1974. Time intervals between observations vary from 1 to 3 h. The abscissa for each time (identified in parenthesis) is shifted so that the origin is indicated by dotted lines.

Figure 4 Time-height section of eastward wind component (u) in the vicinity of the tropopause during Phase I. Contours have been smoothed slightly. Contour interval is 12.2 m s^{-1} (40 ft s^{-1}). Shaded vertically hatched regions denote eastward motion. Horizontally hatched regions denote westward motion in excess of 24.4 m s^{-1} (80 ft s^{-1}). Heavy contour is -12.2 m s^{-1} (-40 ft s^{-1}).

Figure 5 Time-height section of northward wind component (v) in the vicinity of the tropopause during Phase I. Contours have been smoothed slightly. Contour interval is 6.1 m s^{-1} (20 ft s^{-1}). Shading denotes northward motion, with vertically hatched areas enclosing maxima. Horizontally hatched regions denote southward motion in excess of 6.1 m s^{-1} (20 ft s^{-1}). Heavy contour separates northward from southward flow.

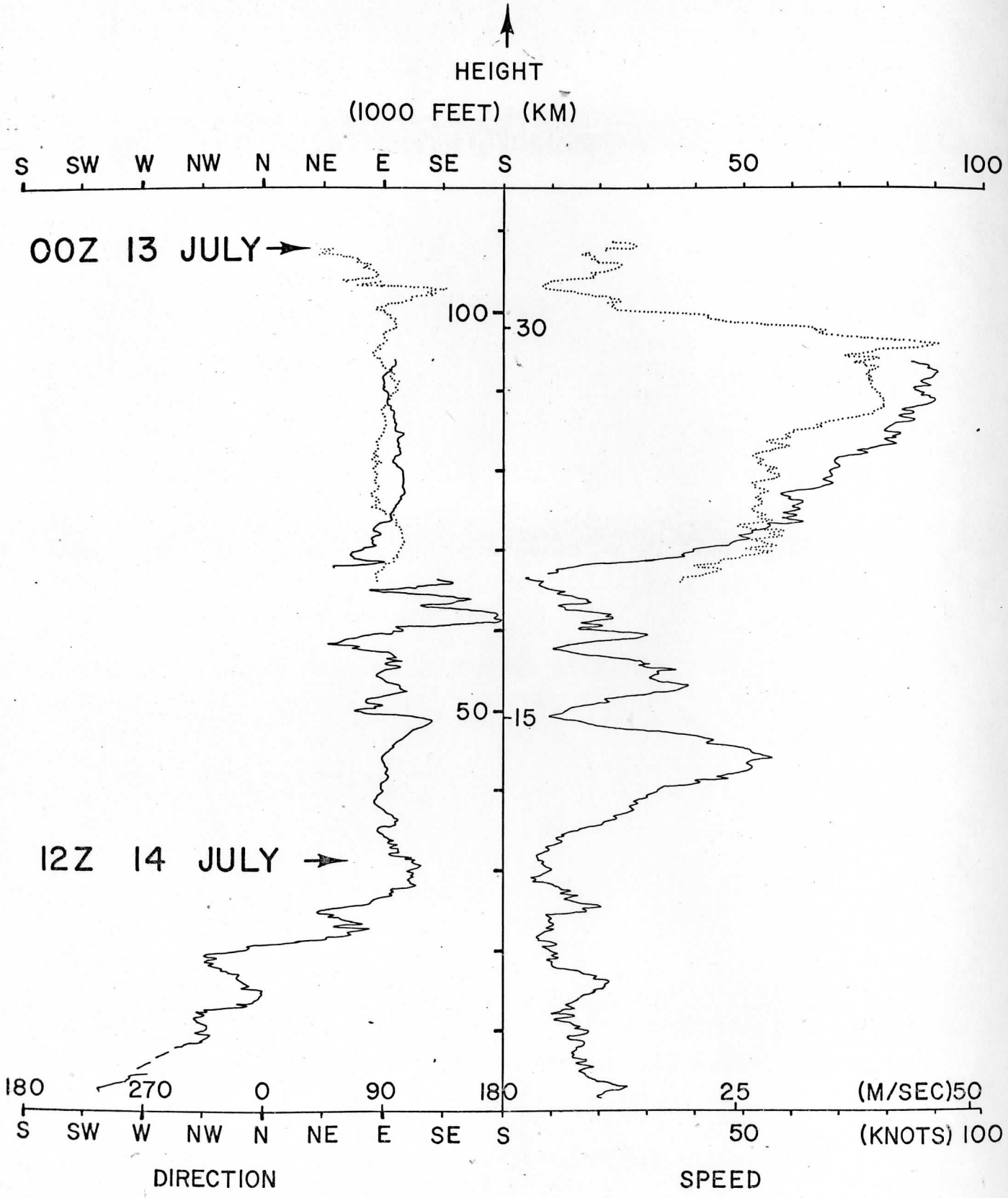
HEIGHT
(1000 FEET) (KM)
S SW W NW N NE E SE S
50
100
00Z 13 JULY
100
30
50
15
12Z 14 JULY
180 270 0 90 180
25
(M/SEC)50
S SW W NW N NE E SE S
50
(KNOTS) 100
DIRECTION
SPEED

Figure 1

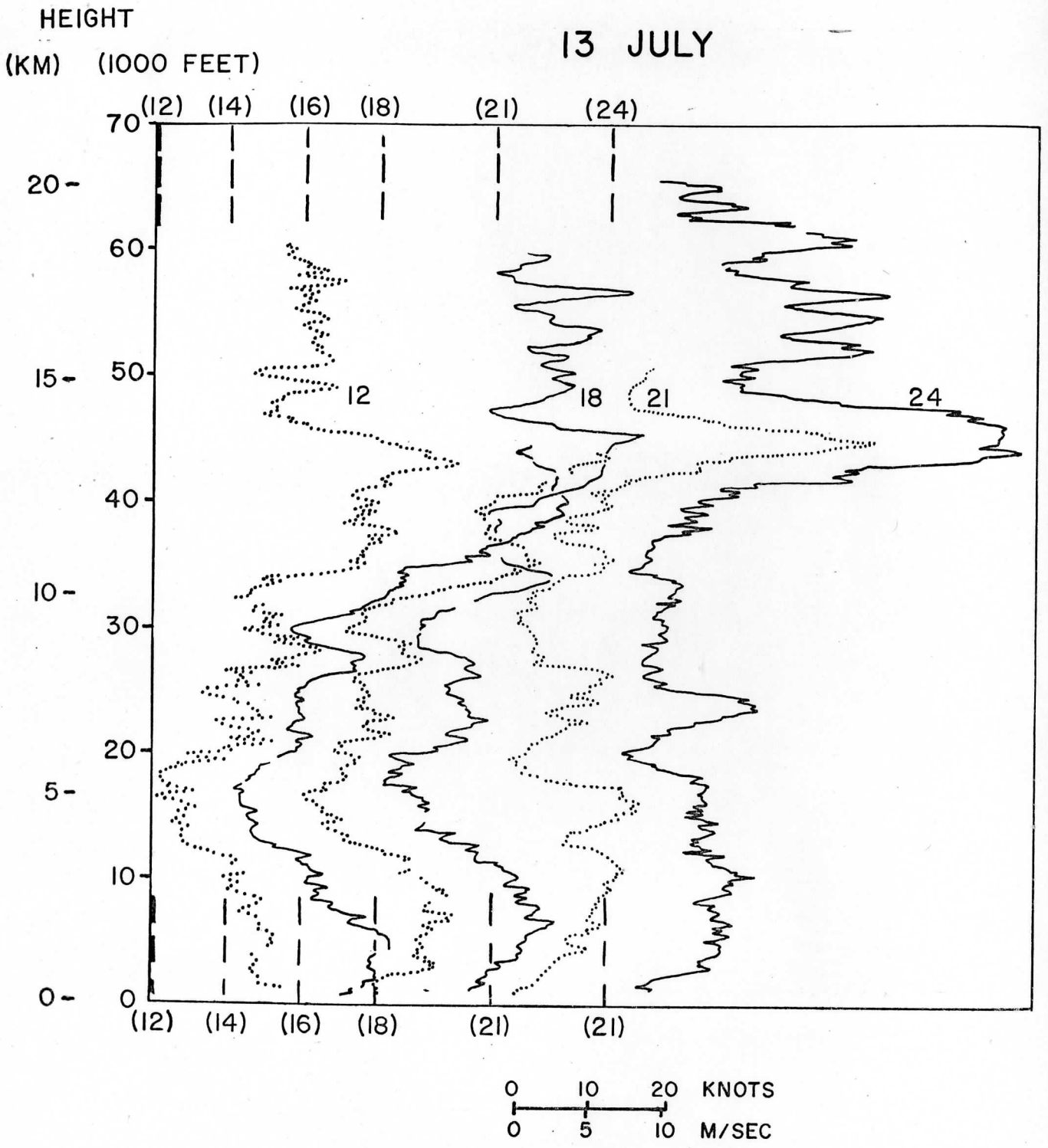
HEIGHT
(KM) (1000 FEET)
13 JULY
(12) (14) (16) (18) (21) (24)
70
20
60
15
50
12
18
21
24
40
10
30
20
5
10
0
0
(12) (14) (16) (18) (21) (21)
0 10 20 KNOTS
0 5 10 M/SEC

Figure 2

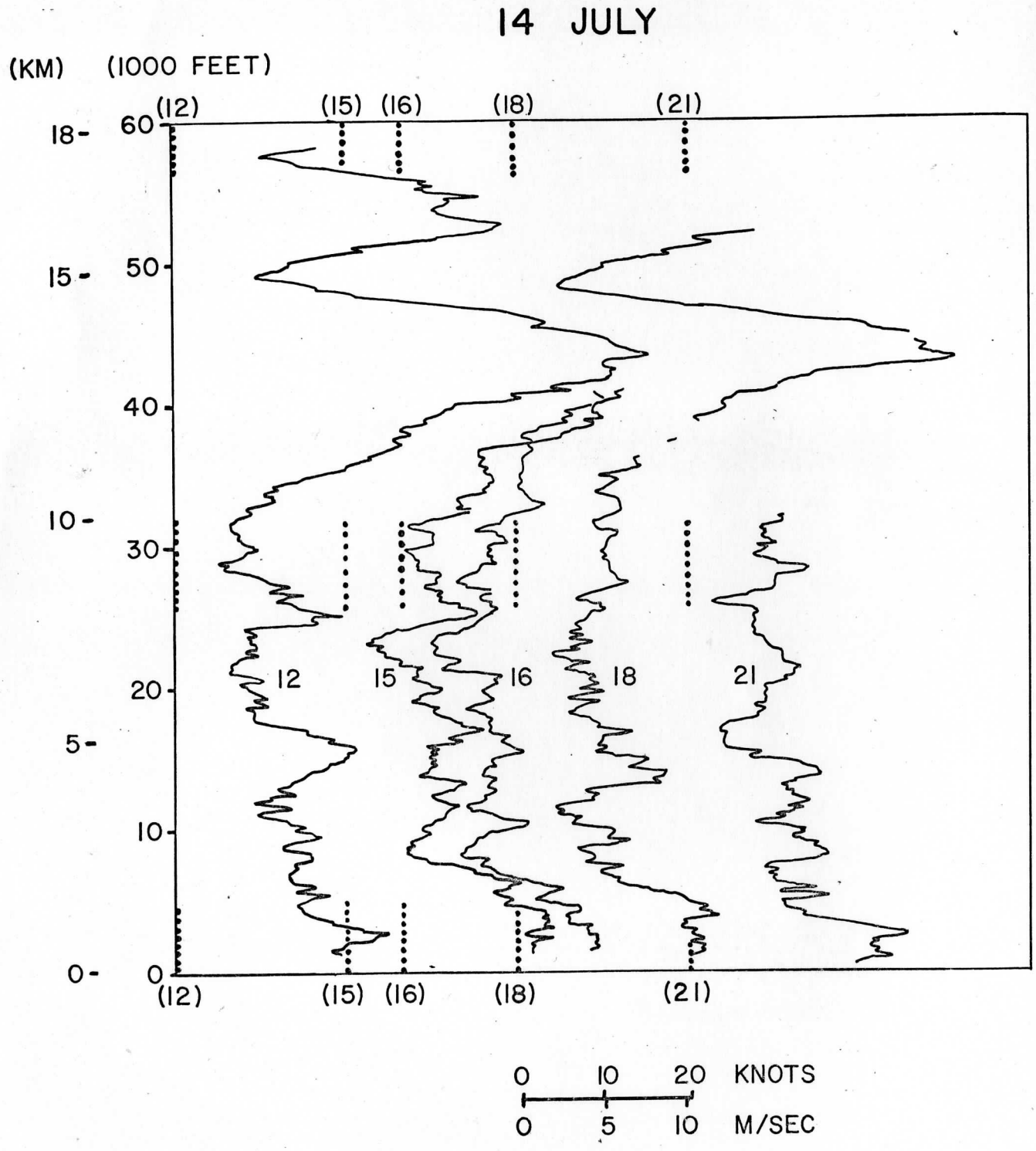
14 JULY
(KM)
(1000 FEET)
(12)
(15)
(16)
(18)
(21)
18-
60
15-
50
40
10-
30
20
5-
10
0-
0
12
15
16
18
21
0
10
20
KNOTS
0
5
10
M/SEC

Figure 3

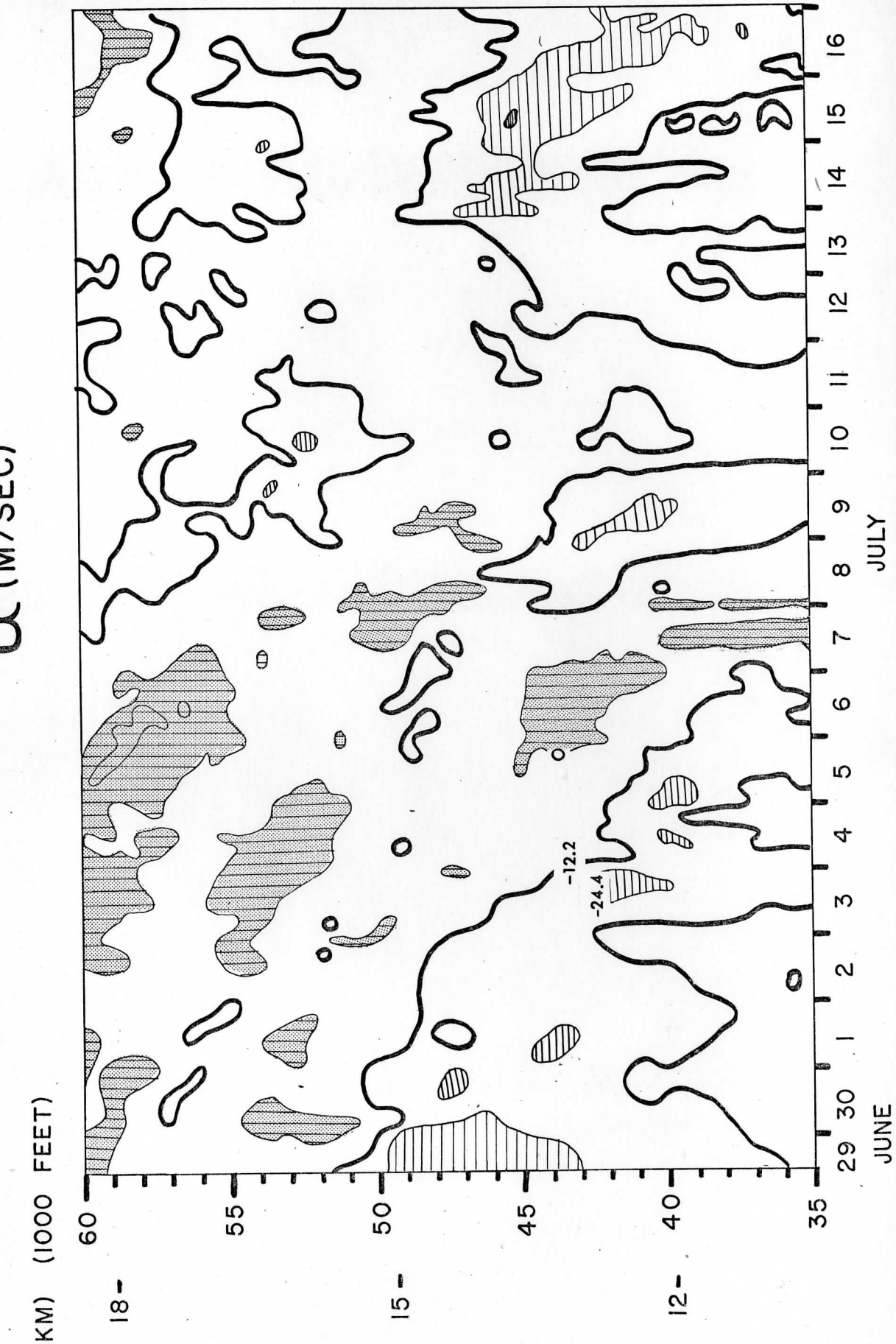
U (M/SEC)
(KM) (1000 FEET)
18-
15-
12-
60
55
50
45
40
35
-12.2
-24.4
29 30 1 2 3 4 5 6 7 8 9 10 11 12 13 14 15 16
JUNE
JULY

Figure 4

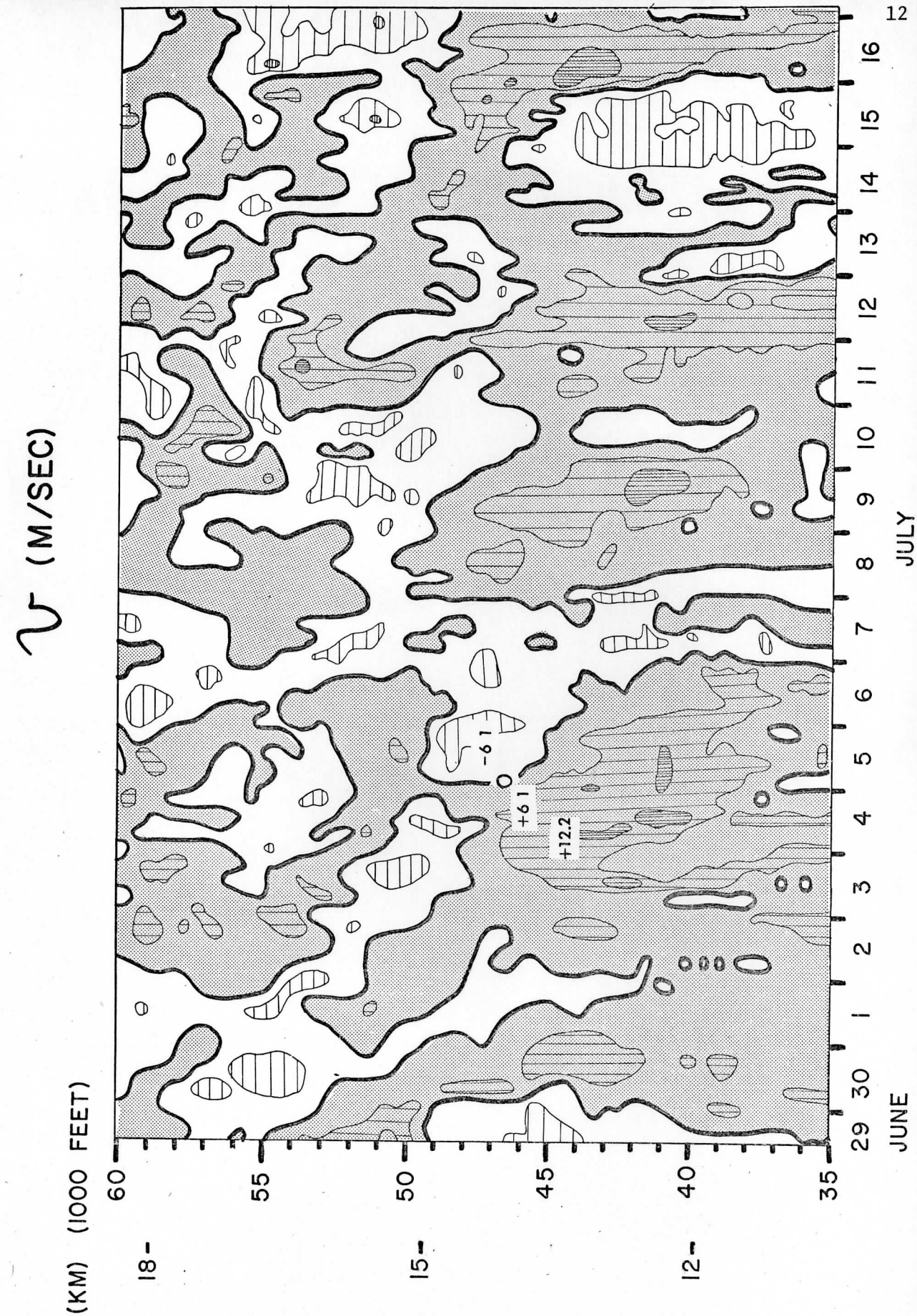
υ (M/SEC)
(KM) (1000 FEET)
60
55
50
45
40
35
18-
15-
12-
-6 1
0
+6 1
+12.2
29 30 1 2 3 4 5 6 7 8 9 10 11 12 13 14 15 16
JUNE
JULY

Figure 5

PROPAGATION OF CLOUD PATTERNS OVER THE TROPICAL EASTERN PACIFIC, SOUTH AMERICA, AND THE ATLANTIC

W. R. Barchet and C. S. Lo

ABSTRACT

The two-dimensional propagation of large-scale cloud patterns over the tropical eastern Pacific, South America, and Atlantic is examined by forming time series of average opaque cloudiness in 5° latitude by 10° longitude rectangles from ESSA III satellite cloud photograph mosaics. Zonal and meridional trace speeds of cloud deviation patterns across the rectangular grid are measured on time-longitude and time-latitude sections, respectively, of the response of the deviations from mean cloudiness to bandpass filters centered at 4, 6, and 10 day periods, prominent periods characteristic of tropical disturbances. The principle of pattern recognition is used to measure the slope of banded patterns found on the time sections. Statistics showing the dominant zonal and meridional propagation modes are derived from the slope time series. Using a plane wave model of cloud pattern propagation, zonal and meridional components are combined to yield a two-dimensional sense of motion to the deviation patterns. Eastward motion is common near the equator and at the latitudinal extremes of the study area at 25°N and 25°S, while westward movement dominates in other latitudes. Northward movement is prominent in both hemispheres implying a cross-equator movement of cloud patterns. The results are also discussed from the viewpoint of a zonally propagating cloud pattern with a horizontal tilt to its axis. An orientation from SW to NE is dominant in most regions except over northern South America, the Carribean, and the north Atlantic, where a NW to SE tilt prevails for disturbances with a 6-day period. This study concludes that pattern recognition can be used to extract from satellite data the major features of cloud disturbance propagation.

1. INTRODUCTION

In a sequence of reports, Sikdar et al. (1972), Young and Sikdar (1973, 1974), and Heinricy and Young (1974) presented the spectral characteristics of cloud patterns derived from ESSA III mosaics. The principal investigations and study areas determined spectral statistics for the central Pacific Ocean (Sikdar et al., 1972), the eastern Pacific and

Atlantic Oceans (Young and Sikdar, 1974), and western Africa (Heinricy and Young, 1974). Time series analysis were also made of the longitudinal variations of zonal means and deviations from the zonal mean of cloud amount over these areas. All of these studies included the summer period of 1 March 1967 to 31 August 1967 although Young and Sikdar (1974) and Heinricy and Young (1974) considered longer periods in observing annual and interannual trends in the power spectra.

Numerous studies of disturbances in the circulation patterns of the tropics overlapped with or included the same time interval. Spectral characteristics of the wind field over the central and western Pacific Ocean, studied by Yanai and Maruyama (1966), Yanai et al. (1968), Wallace and Chang (1969), and Nitta (1970) revealed prominent peaks in the power spectra at periods of 4-5 days, 6-7 days, and 10-15 days. Gruber (1975) using satellite derived winds found spectral peaks at similar periods. Chang (1970) and Wallace (1970) presented the first time-longitude series of zonal cloud cover using zonal strips of ESSA III mosaics and noted that an apparent 4-day periodicity in the cloud patterns displayed wavelengths similar to those found in the wind field analyses. The spectral studies of cloud distributions by Sikdar and by Young, with emphasis on periods of 4, 6, and 10 days, soon followed. Gruber (1974) used satellite-measured cloud brightness over a study area which was circumglobal in the tropics and found transient and quasistationary waves with periods and wave numbers in agreement with previous studies.

This study focuses attention on the tropical eastern Pacific and Atlantic Oceans, including Central and South America and the extreme western portion of Africa (see Fig. 1). Spectral statistics of cloudiness patterns in this region were presented by Young and Sikdar (1974). However it appears useful to take the time-longitude series analyses by Young and Sikdar (1973) for the central Pacific and extend them into the eastern regions to see the effect of land areas on cloud pattern propagation. Also the cloud data are examined in time-latitude series to determine a more complete two dimensional sense of propagation of the disturbance patterns.

2. DATA

The study area shown in Fig. 1, lying between 25°N and 25°S latitude and 120°W and 0° longitude, is divided into 120 rectangles, each 5° latitude wide and 10° longitude long. Daily values of the percentage of opaque cloud cover (excluding the lowest 30% of the ESSA III gray scale) in each of these small rectangles is estimated as described by Sikdar et al. (1972) from ESSA III mosaics for the 184 day period from 1 March 1967 to 31 August 1967. Heinricy and Young (1974) discuss in detail the accuracy and application of this method of cloud cover estimation. This data is the same as that used by Young and Sikdar (1974) to obtain spectral statistics for cloud amount over the study area.

3. ZONAL DEVIATIONS

The cloud amount data for each zonal strip is decomposed into a zonal time mean and deviations from the time mean. Bandpass filters with center periods near 4, 6, and 10 days and half power widths of 0.0625 cpd are applied to the zonal deviations following the procedures outlined in Young and Sikdar (1973). This is done to form time-longitude series of the zonal deviations from the mean zonal cloudiness and of the response of these deviations to the bandpass filters. Characteristic examples out of the ten time-longitude series obtained are shown in Fig. 2 for 10-15°N and in Fig. 3 for 0-5°S latitudes.

Two features of the filtered patterns stand out. Brief periods exist during which the banded patterns are arranged in uniformly sloping groups. During such periods the patterns exhibit a zonal coherence that can be interpreted as a sense of propagation of a disturbance feature in the cloud amount along the zonal band. The slope of the band provides an estimate of the trace speed of a departure pattern along the zonal strip. In Fig. 2, for example, such patterns stand out in the 4-day filter response in early April (eastward propagation) and in the 6- and 10-day filtered data in late August (westward propagation). Such coherent banded features are apparent in all filtered displays at all latitudes with both eastward and westward propagation present at various times. Even the deviation patterns (unfiltered data) display sloping bands as seen, for example, in Fig. 2 in April (eastward) or in July (westward).

The second noticeable feature of these patterns is the apparent lack of organization of the filtered responses into any longitudinally or temporally coherent pattern for significant portions of the time series. Such noisy patterns may exist for one filter only, i.e., near 1 August in Fig. 2 for the 4-day filter, or may be seen in all filter responses at various times and latitudes. This intermittence of coherent disturbance propagation led Wallace and Chang (1972) to conclude that such time series usually do not yield reliable statistics if objectively analysed.

In contrast to the time-longitude series presented by Young and Sikdar (1973) for the central Pacific, the area under study here does include land areas. In both Figs. 2 and 3 the longitudes occupied by land are identified. Visual inspection of the time series in Fig. 3, for instance, reveals that the banded features often show kinks in the vicinity of the coast of the land areas; however, it is important to recognize the limited spatial resolution afforded by averaging cloud amount over 10° longitude. The response to the 6-day filter in early April shows zig-zag bands which imply eastward propagation over South America and westward propagation over the oceans east and west of the

continent. Similar patterns exist in early May in the 4-day filter series. One episode of apparent standing wave activity is found during the latter half of July where it appears that the longitudinal width of South America establishes the zonal wavelength. Not all propagation bands are as markedly perturbed by land areas as in these examples. However, the number, duration, and longitudinal extent of patterns of consistent propagation in either direction are less in latitudes containing extensive land areas.

Even the unfiltered cloud amount deviation patterns show the effect of land areas. The position of maximum positive departure shows a westward shift with time at all latitudes. Over South America this shift takes place between May and June and moves the region of maximum cloudiness from a position over the continent in April to a position off the west coast of South America in June. Young and Sikdar (1973) found no noticeable westward drift of maximum cloudiness departure in the central Pacific. However, this shift is seen in the maximum cloud brightness fields presented by Hubert et al. (1969).

Dominant zonal trace speeds and directions are determined from the time-longitude series by measuring the slope of the banded patterns at each day for each filter period. The slope of the banded patterns is averaged over a 40° wide longtiude strip along each latitude band: 0-40°W, 40-80°W, and 80-120°W longitudes. Statistics on the frequency with which a given slope is observed in the 178 day series are compiled for each filter at each latitude. The probability density of observing a given slope is given in Fig. 4 for the three filter periods and three longitude strips as a function of the time interval of propagation in a zonal direction across 10° longitude (days/10°). At any latitude the integral of the probability density is unity. Propagation time scales for the three filters are different reflecting the inherently slower propagation rates of the longer period disturbances. Time resolution for the estimation of the slope of the bands is 1/4 day for the 4-day filter, 1/2 day for the 6-day filter, and 1 day for the 10-day filter. This decrease in time resolution as filter period increases is due to the greater width of the banded patterns at longer periods (see Figs. 2 and 3) which makes estimating the slope of these bands less precise. Such resolution limitations along with the average over 40° longitude effectively filters high speed disturbances out of the slope data. The zonal trace speed in degrees longitude per day is equal to 10 times the inverse of the propagation time interval.

The contour patterns clearly indicate the dominant propagation times at each latitude. Westward propagation dominates the tropical belt from 15°N to 15°S latitude although at 0-5°N in the 4-day filter over the Atlantic and at 0-5°S in the 6-day filter over the eastern Pacific significant periods of eastward propagation occur. The influence of

disturbances in the westerlies is evident in the large eastward probability densities found at both latitudinal extremes, especially in the 4-day filter responses. The frequency of patterns with zero propagation time, usually assigned when no clear slope could be determined or when the banded patterns were chaotic over the 40° longitude strip, is greatest in the 10-day filter data in the southern hemisphere. The propagation time intervals associated with probability densities in excess of 0.25 day^{-1} are given in Table I for the three longitude regimes and filter periods. No clear distinction between the three longitudinal regimes can be seen, although propagation speeds are slightly higher in the Pacific and South American regimes than over the Atlantic at all filter periods.

The zonal trace speeds and wave numbers given in Table I compare favorably with the results of Gruber (1974) and Zangvil (1975), summarized in Table II, when similar wave periods are considered. The technique of averaging the slope of the bands found in the time series over 40° longitude has the effect of filtering very high and very low speed waves out of the propagation data; the time resolution for determining the slope also reduces the sensitivity of this analysis to high speed disturbances in cloud amount. These effects are the most likely explanation for the slow propagation speeds found to be dominant in this study and which, at first glance, contradict the large coherency magnitudes found by Young and Sikdar (1974) in the eastern Pacific and Atlantic regimes at very high trace speeds. In Young and Sikdar's analysis the phase coherency between adjacent 10° longitude wide rectangles was used to calculate the trace speed, hence higher speed waves could be detected. A similar failure to resolve the high speed waves identified by Zangvil (1975) is attributed to this same shortcoming. While the approach used here discriminates against the high speed, low wave number disturbances, it accentuates those disturbances which exhibit patterns on large space scales. These are the patterns which Wallace and Chang (1972) indicated should be emphasized. The zonal trace speeds found here, as displayed in Fig. 4 and highlighted in Table I, do fall within the range of speeds given by Wallace and Chang for westward propagating Rossby waves and eastward propagating Kelvin-like waves near the equator.

4. MERIDIONAL DEVIATIONS

A logical extension of the zonal analysis is to treat the cloud amount data as though it were composed of meridionally propagating disturbances. In a fashion similar to the zonal deviations, the cloud amount data for each meridional slice of 10° longitude width is decomposed into a meridional time mean and a deviation from the meridional mean. The three bandpass filters are applied to this data to form a time-latitude series of the response of the meridional deviations to the filters.

Three examples from the set of twelve are presented here and represent different regimes: the Atlantic (Fig. 5), the South American (Fig. 6), and the eastern Pacific (Fig. 7).

The unfiltered meridional deviations presented in the time-latitude series indicate the position in each regime of the zone of maximum cloudiness (Sadler, 1975) and show its seasonal south to north migration during the study period. Over the South American continent the northward movement of the zone of maximum cloudiness begins in April and continues through the end of May. In contrast, the eastern Pacific and Atlantic show a very abrupt northward shift of the zone of maximum cloudiness in mid-April and mid-May, respectively. The 5° latitude resolution of cloud amount is the most likely reason preventing the double maximum of cloud brightness found by Hubert et al. (1969) from appearing in the Pacific regime series.

Examination of the filter responses indicates persistent banded patterns are present in the time-latitude series which imply that brief intervals exist during which the deviation patterns are propagating north- or southward. Northward propagation, e.g. 10-day filter in the eastern Pacific during July, 6-day filter over South America in late March, and 4-day filter in the Atlantic for the months of June and July, appears to be more common than southward propagation, e.g. 6-day filter over South America in August or 4-day filter in the eastern Pacific in late May. The banded features in the meridional sections show greater irregularity than the zonal patterns making the impact of land areas on the patterns less apparent. In fact, the zone of maximum cloudiness is more often associated with kinks or organized patterns in the bands than are land areas.

If a sloping band can be interpreted as a moving disturbance feature in the cloudiness, then the V-shaped features opening toward increasing time seen in Figs. 5, 6, and 7 (as well as in the zonal patterns of Figs. 2 and 3) may indicate the presence of disturbances diverging from a common origin at the vertex of the "V". Such V-shaped patterns frequently appear to be associated with the zone of maximum cloudiness, e.g. 6-day filter over the Atlantic in April. The very strong response to the 10-day filter in this same diagram occurs at the time the zone of maximum cloudiness abruptly shifts northward. A similar pattern in the 4-day filter for the eastern Pacific appears at the time the transition northward occurs there. One V-shaped pattern observed early in June over the Atlantic in the 4-day filter is associated with a negative departure from the meridional mean cloudiness, i.e., an area of less than average cloud amount.

Occasionally checkerboard patterns indicative of quasi-stationary oscillations of cloud amount appear in the meridional deviation series,

e.g. 10-day filter over South America in early May, 6-day filter in the eastern Pacific in April, and 4-day filter in the Atlantic during early August. Except for the 6-day filter case, the equator appears as a nodal point and the wavelength apparently exceeds 25° latitude.

Longitudinal statistics on the meridional propagation of departures from the mean cloudiness are determined in the same manner as the zonal propagation statistics. The slopes of the banded patterns are measured on a daily basis and frequency statistics are determined for each meridional slice from the time series of propagation intervals across each hemispheric portion of each meridional slice. The propagation times here represent an average over 25° latitude and hence resolution of high propagation rates and small meridional wave numbers will be poor. Also, the resolution of the propagation time, which is the same for zonal propagation at each filter period, further reduces sensitivity of this analysis to high speed disturbances.

Propagation statistics for the two hemispheres are presented for each filter period in Fig. 8 where the contours represent equal probability density (day^{-1}) of observing a given propagation time across 10° latitude. The subjective conclusions which can be drawn from a visual examination of the time-latitude series of Figs. 5, 6, and 7 are confirmed by these quantitative assessments of the propagation statistics. The disturbance patterns at nearly all longitudes and in both hemispheres show a dominance of northward propagation. The longitudes and meridional trace speeds for the most prominent, i.e., persistent, propagation features are summarized in Table III; only longitudes with probabilities density peaks in excess of 0.25 day^{-1} are included in this table.

Comparing Table III with Table I for the zonal propagation demonstrates that the meridional propagation is generally slower than zonal movement and has correspondingly larger meridional wave numbers. The number of distinct cases of northward propagation is clearly larger than those with southward displacement. Quasi-stationary patterns are more abundant in the meridional data than in the zonal data and show up both in the 6-day and 10-day filtered results. The frequent mention of longitudes 40-50°W and 70-80°W or adjacent longitude slices in this table is an indication of the strong interaction between the South American coast and meridional propagation of cloud amount disturbances.

5. PROPAGATION OF PATTERNS

The discussions of the time-longitude and time-latitude series deal with the zonal and meridional movement of cloud amount deviation patterns as though these patterns are independent of each other. A synthesis of these patterns, presented in this section, is necessary to gain a two-dimensional view of the propagation of the disturbances producing the

patterns. Nearly all previous studies of tropical cloud patterns have concentrated on describing zonal propagation modes. Meridional propagation has been ignored or considered to be an artifact resulting from a tilt to the axis of a zonally propagating disturbance (Young and Sikdar, 1973). While such a tilt may indeed give rise to an apparent sense of meridional movement the possibility that meridional propagation, independent of wave axis tilt, may be present in the deviation patterns can not be unequivocally ruled out.

Propagation times in the preceding sections represent averages over rectangles 25° latitude wide by 40° longitude long. Within each of these rectangles the zonal trace speed is available at five latitudes and the meridional trace speed at 4 longitudes. These quantities can be combined to yield twenty (5 x 4) separate estimates of daily disturbance propagation within each of the six large rectangles shown in Fig. 1; an average over these twenty values gives an average disturbance propagation within each rectangle. Although such an average drastically reduces the zonal and meridional resolution, the effect is to give better contrast between the six major geographical regions in the study area. From the time series of daily zonal and meridional propagation times, the statistics for which are given separately in Figs. 4 and 8, a distribution of apparent disturbance propagation in 2-dimensions can be assembled. These statistics are presented in Fig. 9 for each filter period with individual diagrams for each of the six rectangles arranged as in Fig. 1. The contours represent equal joint probability density (day^{-2}) of observing a specific combination of zonal and meridional propagation times within each rectangle. An integral of the probability density over the area of each diagram is unity.

Before discussing these diagrams it is useful to consider their interpretation. The propagation time intervals (Δt_x or Δt_y) relate the slope of the bands found on the time-longitude or -latitude series to the zonal (c_x) or meridional (c_y) trace speed, the speed at which the disturbance appears to travel across a zonal or meridional grid with spacing Δx or Δy, respectively: $c_x = \Delta x/\Delta t_x$ and $c_y = \Delta y/\Delta t_y$. However, if it is assumed that the disturbance, over the dimensions of the grid, propagates as a plane wave, the 2-dimensional phase speed (V) of this wave is given by

$$V = [c_x^{-2} + c_y^{-2}]^{-1/2} = [(\Delta t_x/\Delta x)^2 + (\Delta t_y/\Delta y)^2]^{-1/2}$$

and the direction of propagation (θ) normal to the plane wave is

$$\theta = \text{Arc tan } (c_x/c_y) = \text{Arc tan } \left[\frac{\Delta t_x}{\Delta x}\ \frac{\Delta y}{\Delta t_y}\right]$$

The appropriate quadrant for θ, measured clockwise from north, is determined by the algebraic sign of c_x and c_y, east and north positive. For the data given in Fig. 9, the zonal and meridional propagation times are given with $\Delta x = \Delta y = 10°$ and are expressed as days/10° on the diagrams.

The accuracy to which V and θ can be determined from the data is dependent on the resolution with which Δt_x and Δt_y can be determined from the time series. The error (σ) in the estimate of the propagation time can, as a first approximation, be set equal to the time resolution of the estimate for propagation across the grid (i.e., 1/4, 1/2, and 1 day/10° for the 4-, 6-, and 10-day filters, respectively). An analysis of the relative error in V and of the error in radians for θ yields $V\sigma$ as the magnitude of the error associated with these quantities. For example, if V = 10°/day, the relative error in V is 25% while the angular error in θ is 14° for the 4-day filter data.

The diagrams in Fig. 9 demonstate that there is a correlation between the time-latitude and time-longitude banded patterns. Closed isolines of probability density surround maxima in the joint observance probability of simultaneous zonal and meridional propagation. These maxima are most clearly present in the 4-day filter diagrams and degrade as the filter period increases until in the 10-day filtered results the maxima are small and lie on the coordinate axes. Maxima on coordinate axes indicate purely zonal (x-axis) or meridional (y-axis) propagation is prominent. Where the maximum lies off axis, the apparent dominant propagation mode is not along a principal coordinate direction.

Examination of the diagrams reveals that propagation with a northward and westward component is usually found in the 4-day filter results. However, over South America westward and eastward propagation with a northward component is found with about the same frequency. In both hemispheres northward propagation is present in all regimes indicating that there is cross-equator movement of cloud amount disturbances from south to north. This agrees with the observations of Young and Sikdar (1973) for the eastern Pacific (120-130°W). The 6-day filter results show considerably more variation (broader patterns); propagation containing a westward component is commonly found. In general, the oceanic regimes show a dominance of propagation away from the equator and westward (or eastward over the Atlantic). Over most of South America northward movement generally dominates, although both north and south moving patterns are associated with westward propagation over northern South America. For the 10-day filter results the patterns are very broad (low probability densities) with maxima mainly on the axes. Northward propagation (and hence cross-equator movement) is common in all except the southern Atlantic regime where eastward propagation dominates and in the southeastern Pacific where westward propagation is prominent. Quasi-stationary disturbances

(or chaotic patterns) have large probability densities over northern South America in the 6-day filter data. In the 10-day filter results this occurs everywhere except in the northern South American and Atlantic regimes. This is not surprising since the very broad bands found in the time-latitude and -longitude series at these filter periods makes estimating a value for the slope difficult. When no clear slope exists a value of zero is given to the slope for that day.

The prominent two-dimensional propagation modes identifiable in Fig. 9 are given in Table IV along with the corresponding phase speed and direction of plane wave propagation. In comparison of Tables I and III for zonal and meridional propagation, the speeds given in Table IV are noticeably smaller because of the inverse sum of the squares of the trace speeds used to calculate the phase speed. Because of the increase in the range of propagation time intervals as the filter period increases, the probability densities also become smaller. Hence the threshold probability density for inclusion in Table IV is 0.05, 0.04, and 0.02 day^{-2} for the 4-, 6-, and 10-day filtered data, respectively. Propagation data for each region are given in order of decreasing probability density.

6. HORIZONTAL TILT TO ZONALLY PROPAGATING DISTURBANCES

The assumption that the banded patterns seen in the time-latitude or -longtidue sections are the result of a propagating plane wave has its limitations. The inferred motion of the plane wave does not imply that individual cloud elements propagate in the same manner. Such elements can not be identified because of the averaging of cloud amount over the 5 x 10° rectangles used to formulate the time series. Several authors refer to propagation of cloud systems or wind field disturbances in terms of a tilt to zonally propagating features, for example, Nitta (1970), Krishnamurti (1971), and Young and Sikdar (1973). The results presented here can also be viewed in this fashion with but minor alterations.

For westward propagating disturbances, a two-dimensional propagation vector in the NW quadrant of the diagram in Fig. 9 implies the plane wave is oriented in a SW-NE fashion while a vector in the SW quadrant produces a plane wave with a tilt oriented from NW to SE. A propagation vector to the NE for eastward movement of a disturbance also implies a NW-SE tilt and a SE vector gives rise to a SW-NE tilt to an eastward moving disturbance.

With this interpretation most westward propagating disturbances for all filters show a tendency for a SW-NE tilt. An exception is found in

the 6-day filter results in the southeastern Pacific and southern Atlantic regimes in which the tilt is mainly NW-SE. Eastward propagation in the 4-day filter data is also associated with a NW-SE tilt but this mode is relatively scarce in the 6-day filter diagrams except in the north Atlantic regime. With the 10-day filter, tilted patterns become less frequent although even here a SW-NE tilt is present, especially in the north Atlantic and southeastern Pacific regimes. Over South America a SW-NE tilt appears to dominate in the northern hemisphere while no clear cut sense of tilt is apparent in southern South America. The purely meridional propagation modes found in the 10-day filtered results can not be reconciled with tilted zonally propagating waves.

7. CROSS-EQUATOR MOVEMENT OF CLOUD PATTERNS

Large maxima of probability density for northward propagation of cloud amount deviation in both hemispheres, as found in Fig. 8, are not a unique demonstration of cross-equator propagation of cloud patterns. It is possible to arrive at these statistics without having the necessary temporal correlation between the meridional propagation found in each hemisphere to yield northward cross-equator movement. Fig. 10 gives, in a very compact form, contingency tables for each filter period and longitudinal regime which show the correlation between meridional propagation in both hemispheres and also between zonal motion in the two latitude belts adjacent to the equator.

The meaning of the various boxes in Fig. 10a is clarified by Figs. 10b and 10c. The squares within the double lined boxes (with one box for each longitudinal regime and filter period) give the correlation between meridional propagation in the two hemispheres. The y-axis (northward positive, up) applies to the northern hemisphere while the x-axis (northward, right) applies to the southern hemisphere. Numbers within the diamonds (Fig. 10b) give the frequency of simultaneous observation of a particular pair of meridional propagation directions in each hemisphere. Frequencies for a given box do not add to unity because quasi-stationary and chaotic modes are excluded from these tables. Each square within a box has within it a contingency table for the simultaneous observation of zonal motion in the 0-5°S (x-axis) and 0-5°N (y-axis) latitude bands with eastward propagation positive (right and up, respectively; see Fig. 10c). Also quasi-stationary and chaotic modes are eliminated from these tables so the frequencies do not add to unity. The appropriate maximum values are underlined in each box.

Seven out of nine boxes show that northward propagation occurs simultaneously in both hemispheres indicating that northward, cross-

equator movement of cloud amount deviation patterns dominates in these longitude regimes and filter periods. This is especially true for the 4-day filter results. Only the 6-day filter results for the South American and Atlantic regimes are different; both show a divergence of patterns away from the equator. Simultaneous westward propagation in both hemispheres most frequently accompanies the northward movement. However, cyclonic and anticyclonic shears (northern hemisphere perspective) to the zonal motion near the equator are also prevalent. Only for the 6-day filter results in the South American regime does eastward motion dominate along with the predominant northward propagation.

The contingency table relating meridional and zonal motion of cloud deviation patterns in the two hemispheres in Fig. 10a can also yield information on preferred tilts to the disturbance axis. In the 4-day filter results, northward movement with concurrent westward movement implies a SW-NE cross-equator tilt in the eastern Pacific and Atlantic regimes. This pattern continues for the 6-day filter diagrams in the eastern Pacific region and for the 10-day filter diagrams in the Atlantic region. Over South America, in the 6-day filter table, eastward propagation dominates but the tilts are opposite in each hemisphere, with a NW-SE tilt in the northern hemisphere. In the 6-day filter results over the Atlantic, eastward (southern hemisphere) and westward (northern hemisphere) waves have the same SW-NE tilt. Several regimes show dissimilar zonal motion (east- versus westward) across the equator. It is difficult to visualize these opposing motions arising from the same wave disturbance acting in both hemispheres.

These results, by and large, parallel those of Young and Sikdar (1973) for the eastern Pacific. Nitta (1970), in a study of wave disturbances over the tropical central Pacific ocean using rawindsonde data, identified a SW-NE tilt to westward propagating waves in the northern hemisphere and a NW-SE tilt for such waves in the southern hemisphere. This would imply that Nitta would have found apparent poleward meridional motion on either side of the equator rather than the mostly northward, cross-equator propagation found here. Krishnamurti (1971), in an analysis of 200 mb wind data for the tropics, found ultra-long, quasi-stationary waves which showed a SW-NE tilt in the northern hemisphere but found little tilt in the same sense in the southern hemisphere. These results are difficult to compare with those herein since the ultra-long waves are not resolved in the limited geographic area studied. Krishnamurti found transient short waves, wave-number 5, had a NW-SE tilt in the southern hemisphere which would agree with the tilts found here in the southern oceanic regimes.

8. CONCLUSIONS

Statistics on the movement of deviation patterns of opaque cloud amount, estimated from ESSA III photo-mosaics, can be obtained by semi-objective analysis of time series of the zonal or meridional

deviations. Pattern recognition, as suggested by Wallace and Chang (1972), is used to estimate the slope of banded patterns which are commonly found on the bandpass filtered time sections of both zonal and meridional deviation from mean cloud amount. This yields trace speeds at each of three different filter center periods which are consistent with those found by objective analysis of the wind field or of similar cloud data. The major difference is a loss of high trace speeds through spatial averaging and a limit on the time resolution to which slopes can be measured. Zonal propagation modes representing westward propagating Rossby waves (mainly at non-equatorial latitudes) and eastward moving Kelvin waves (in equatorial latitudes) are resolved.

A synthesis of zonal and meridional propagation produces a two-dimensional representation of the movement of cloud amount deviation patterns. This representation can be interpreted in two ways. The suggestion that propagation of disturbances in cloud amount as a plane wave of extensive spatial dimension must be rejected as being physically unrealistic; too many constraints are placed on the behavior of a natural system for this model to adequately represent cloud pattern propagation. Nevertheless, the plane wave is conceptually useful for the preliminary analysis of the data. The interpretation that all disturbances which affect cloud amount show only zonal movement also has its difficulties but these can be ameliorated by permitting a latitudinal tilt to the axis of the disturbance. The plane wave model and the two-dimensional propagation vector derived therefrom permits a quantitative estimation of the tilt associated with the zonal propagation of wave-like disturbances. The tilts identified here are generally consistent with those found by Nitta (1970), Krishnamurti (1971), and Young and Sikdar (1973).

ACKNOWLEDGEMENTS

This work would not have been possible without the data set made available to us by Dr. D. N. Sikdar, whose early guidance and continued encouragement are appreciated. The discussion between the authors and Drs. J. A. Young, D. Martin, and B. Hinton are also valued. This research was also partially sponsored by NSF Grant GA-40494.

REFERENCES

Chang, C. P., 1970: Westward Propagating Cloud Patterns in the Tropical Pacific as Seen from Time-Composite Satellite Photographs. J. Atmos. Sci., (27), 133-138.

Gruber, A., 1974: The Wave Number-Frequency Spectra of Satellite Measured Brightness in the Tropics. J. Atmos. Sci., (31), 1675-1680.

_____, 1975: The Wave Number-Frequency Spectra of the 200 mb Wind Field in the Tropics. J. Atmos. Sci., (32), 1615-1625.

Heinricy, D. J. and J. A. Young, 1974: Long-Term Variations in Cloud Activity Over the East Atlantic-West Africa Region. Studies of the Atmosphere Using Aerospace Probes, Annual Report 1973, Space Science and Engineering Center, Madison, Wisconsin, 28-82.

Hubert, L. F., A. G. Krueger, and J. S. Winston, 1969: The Double Intertropical Convergence Zone: Fact or Fiction? J. Atmos. Sci., (26), 771-773.

Krishnamurti, T. N., 1971: Observational Study of the Tropical Upper Tropospheric Motion Field During the Northern Hemisphere Summer. J. Appl. Meteor., (10), 1066-1096.

Nitta, T., 1970: Statistical Study of Tropospheric Wave Disturbances in the Tropical Pacific Region. J. Meteor. Soc. Japan, (48), 47-59.

Sadler, J. C., 1975: The Monsoon Circulation and Cloudiness Over the GATE Area. Mon. Wea. Rev., (103), 369-387.

Sikdar, D. N., J. A. Young, and V. E. Suomi, 1972: Time-Spectral Characteristics of Large-Scale Cloud Systems in the Tropical Pacific. J. Atmos. Sci., (29), 229-239.

Wallace, J. M., 1970: Time-Longitude Sections of Tropical Cloudiness (December 1965 - November 1967). ESSA Tech. Report NESC 56, U. S. Dept. of Commerce, Washington, D.C.

_____ and C. P. Chang, 1969: Spectrum Analysis of Large-Scale Wave Disturbances in the Tropical Lower Troposphere. J. Atmos. Sci., (26), 1010-1025.

_____ and L. A. Chang, 1972: On the Application of Satellite Data on Cloud Brightness to the Study of Tropical Wave Disturbances. J. Atmos. Sci., (29), 1400-1403.

Yanai, M. and T. Maruyama, 1966: Stratospheric Wave Disturbances Propagating Over the Equatorial Pacific. J. Meteor. Soc. Japan, (44), 291-294.

_____, _____, T. Nitta, and Y. Hayashi, 1968: Power Spectra of Large-Scale Disturbances Over the Tropical Pacific. J. Meteor. Soc. Japan, (46), 308-323.

Young, J. A. and D. N. Šikdar, 1973: A Filtered View of Fluctuating Cloud Patterns in the Tropical Pacific. J. Atmos. Sci., (30), 392-407.

Young, J. A. and D. N. Sikdar, 1974: Temporal Cloud Statistics Over the Tropical Atlantic and Pacific During Summer and Winter. Studies of the Atmosphere Using Aerospace Probes, Annual Report 1973, Space Science and Engineering Center, Madison, Wisconsin, 1-27.

Zangvil, A., 1975: Temporal and Spatial Behavior of Large-Scale Disturbances in Tropical Cloudiness Deduced from Satellite Brightness Data. Mon. Wea. Rev., (103), 904-920.

FIGURE LEGENDS

Figure 1: The study area over which daily cloud amount is estimated from ESSA III mosaics in each 5° latitude by 10° longitude rectangle. The three larger rectangles in bold lines are used in pattern propagation statistics.

Figure 2: Time-longitude section for 10-15°N latitude giving, from left to right, the deviation from the zonal time mean, and the responses of the deviations to 10-, 6-, and 4-day bandpass filters. Shaded areas enclosed by heavy lines are regions of positive deviation, cloudier than average. Contour interval for deviations is 20% and for filtered data, 10%. Land is found east of 20°W and between 85-90°W longitudes.

Figure 3: Same as Figure 2 for 0-5°N latitude with South America occupying longitudes between 40-80°W.

Figure 4: Latitudinal statistics of zonal propagation showing contours of the probability density (day^{-1}) of observing propagation times over 10° longitude within each regime. Contour intervals begin at 5% and increase by 10% thereafter. Note the different zonal propagation time scales for each filter period.

Figure 5: Time-latitude section for 30-20°W longitude giving, from left to right, the deviations from the meridional time mean, and the responses of the deviations to 10-, 6-, and 4-day bandpass filters. Shaded areas enclosed by heavy lines are regions of positive deviations, cloudier than average. Contour interval for deviations is 20% and for filtered data 10%. No land area is present in the Atlantic regime.

Figure 6: Same as Figure 5 but for 70-60°W longitude with land (South America) southward of 10°N latitude.

Figure 7: Same as Figure 5 but for 110-100°W with land partially occupying latitudes northward of 15°N latitude in the eastern Pacific regime.

Figure 8: Longitudinal statistics of meridional propagation showing contours of the probability density (day^{-1}) of observing propagation times over 10° latitude for each hemisphere. Contour intervals begin at 5% and increase by 10% thereafter. Note the different meridional propagation time scales for each filter period.

Figure 9: Joint probability density (units of 0.001 day^{-2}) for simultaneous observation of zonal and meridional propagation in the six large rectangles arranged here as in Figure 1:
(a) 4-day filtered response, contour intervals at 5, 25, 50, 75, and 100 units;
(b) 6-day filtered response, contour intervals at 5, 20, 40, and 60 units;
(c) 10-day filtered response, contour intervals at 5, 15, 25, 35, and 45 units.

Figure 10: Composite meridional and zonal, cross-equator contingency tables:
(a) boxes for three longitudinal regimes and three filter periods;
(b) an example of one box with the correlation frequency (percent) of hemispheric meridional propagation shown in diamonds;
(c) one quadrant of meridional contingency table giving the associated zonal correlation frequencies (per cent) for latitude bands 0-5°N and 0-5°S.

TABLE I

LATITUDE, ZONAL TRACE SPEED, AND WAVE NUMBER OF DOMINANT ZONAL PROPAGATION

Propagation Direction	Filter Period Days	Pacific 80-120°W			South America 40-80°W			Atlantic 0-40°W		
		Latitude	Speed $^{\circ}day^{-1}$	Wave Number	Latitude	Speed $^{\circ}day^{-1}$	Wave Number	Latitude	Speed $^{\circ}day^{-1}$	Wave Number
Westward	4	20-25N	10	9	5-10N	10	9	15-20N	10	9
		10S-20N	5-15	6-18	5-10S	10	9	5-10N	8	11
		15-20S	10	9	15-20S	6	15	5-15S	8	11
	6	5S-15N	4-13	1-15	15-20N	7	9	15-20N	5	12
		15-20S	10	6				5-10S	10	6
	10	10-15N	3.5	10	15-25N	6	6	15-20N	5	7
		5-10S	4	9						
Eastward	4	20-25S	8	11	15-20N	6	6	15-20N	5	7
					20-25S	8	11	0-5S	6	15
								20-25S	10	9
	6	0-5S	7	9	--			20-25S	10	6
		10-15S	9-20	3-20						
	10	--			--			5-10S	3.5	10
Quasi-Stationary	10	5-10N			5-10S			20-25S		
		10-15S								

TABLE II

ZONAL PROPAGATION INFERRED FROM SPECTRAL ANALYSIS BY OTHERS

Propagation Direction	Gruber (1974)				Zangvil (1975)			
	Latitude	Period Days	Speed $^{\circ}day^{-1}$	Wave Number	Latitude	Period Days	Speed $^{\circ}day^{-1}$	Wave Number
Westward	10N	6-12	6-15	4-5	20-30N	10-15	4-12	3-6
		6	7	9	20N	8	3-6	7-15
	5N	12.5	6	5	10N	5	5-10	7-15
						6	10-20	3-6
						4.8	37-75	1-2
						12.5	5-10	3-6
Eastward	10N	50	7	1	10N	4	6-13	7-15
	5N	10	7-12	3-5		5.5	33-65	1-2
						9	20-40	1-2
						40	5-9	1-2
Quasi-Stationary								

TABLE III

LONGITUDE AND MERIDIONAL TRACE SPEED AND WAVE NUMBER OF DOMINANT MERIDIONAL PROPAGATION

Propagation Direction	Filter Period Days	Northern Hemisphere 0 - 25°N			Southern Hemisphere 0 - 25°S		
		Longitude W	Speed $^{\circ}day^{-1}$	Wave Number	Longitude W	Speed $^{\circ}day^{-1}$	Wave Number
Northward	4	10-30	5-10	9-18	0-100	3.5-20	4.5-26
		40-50	7	13	30-40	6	15
		70-80	4-7	13-22	110-120	10	9
		90-100	4	22			
		110-120	4-6	15-22			
	6	20-60	2.5-10	6-24	40-60	2.5-10	6-24
		20-30	3.5	17			
		50-60	5-6	10-12			
		70-80	5	12			
		110-120	2.5	24			
	10	30-40	2.5	14	80-90	1.25	29
		70-80	2.5	14	90-100	10	3.6
		100-110	2.5	14	100-110	2.5	14
Southward	4	0-10	5-20	4.5-18	0-30	4-20	4.5-22
		30-40	6	15	40-50	5-10	9-18
		50-60	10-20	4.5-9	70-90	4-20	4.5-22
	6	60-70	5	12	10-20	5	12
					110-120	3.5	17
	10	20-30	0.8	30	50-60	1.25	29
		40-50	0.8	30			
Quasi-Stationary	6	80-90			30-40		
	10				30-50		
					90-100		

TABLE IV

PROMINENT TWO-DIMENSIONAL PROPAGATION MODES IN THE SIX GEOGRAPHIC REGIMES IDENTIFIED IN FIGURE 1

Filter Period Days	Hemisphere	Pacific		South America		Atlantic	
		Speed$_{-1}$ °day	θ	Speed$_{-1}$ °day	θ	Speed$_{-1}$ °day	θ
4	North	3.6	333	6.0	27	5.5	326
		5.5	214	5.5	326	5.5	34
		3.7	22	8.9	243	5.5	214
						5.1	140
	South	5.5	326	5.1	320	4.7	315
		8.9	243	5.5	34	5.5	34
		5.5	34	5.3	337	5.1	220
						5.5	146
6	North	2.4	346	3.8	41	3.5	315
				Quasi-stationary		4.0	37
				4.5	206		
	South	10.0	270	3.3	350	4.5	206
		2.6	203			4.9	166
		4.9	166				
10	North	Quasi-stationary		2.5	0	2.5	0
		2.5	0	Quasi-stationary			
				2.2	333		
	South	Quasi-stationary		Quasi-stationary		3.3	90
		3.3	270	1.7	0	Quasi-stationary	
		1.3	0				

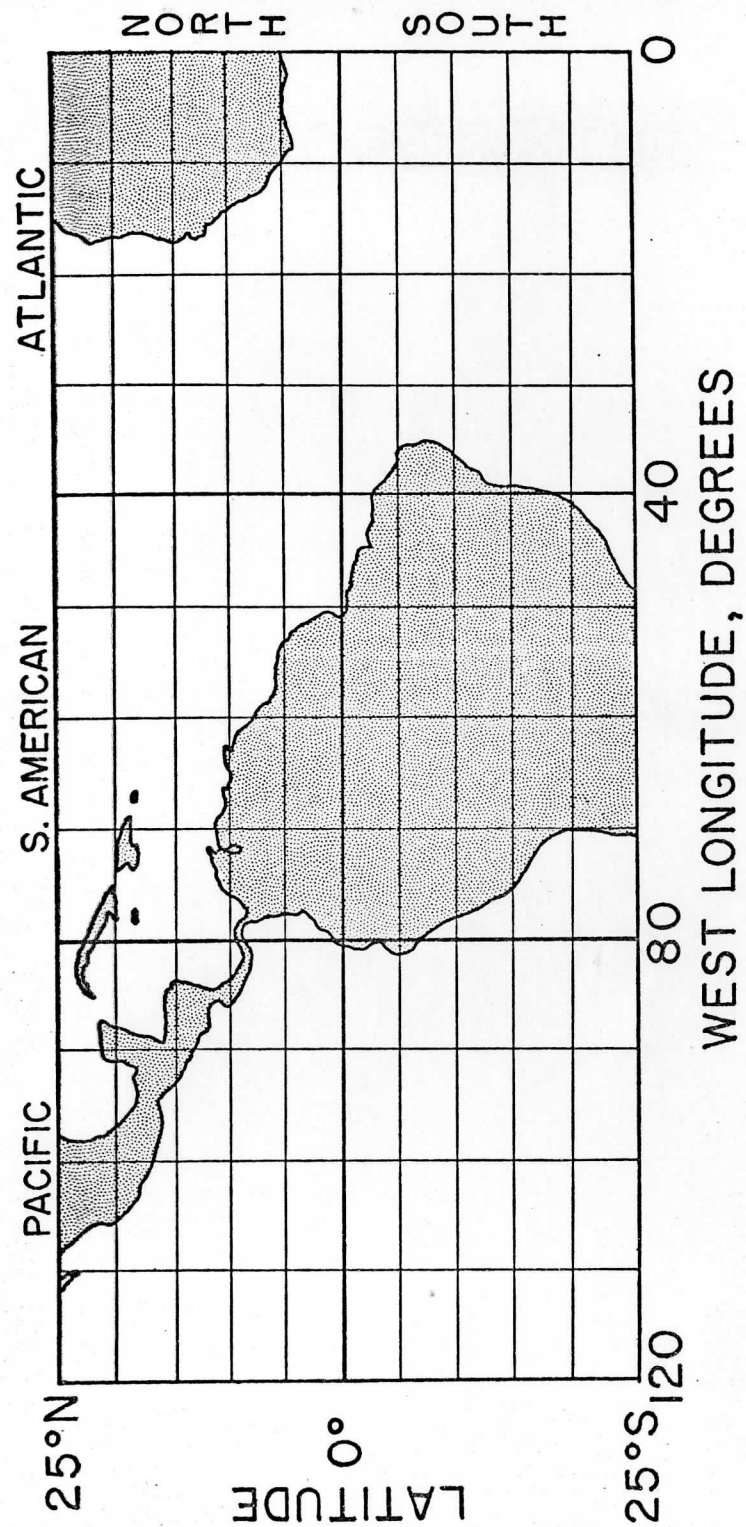
NORTH
SOUTH
ATLANTIC
S. AMERICAN
PACIFIC
0
40
80
120
WEST LONGITUDE, DEGREES
25°N
0°
25°S
LATITUDE

Figure 1

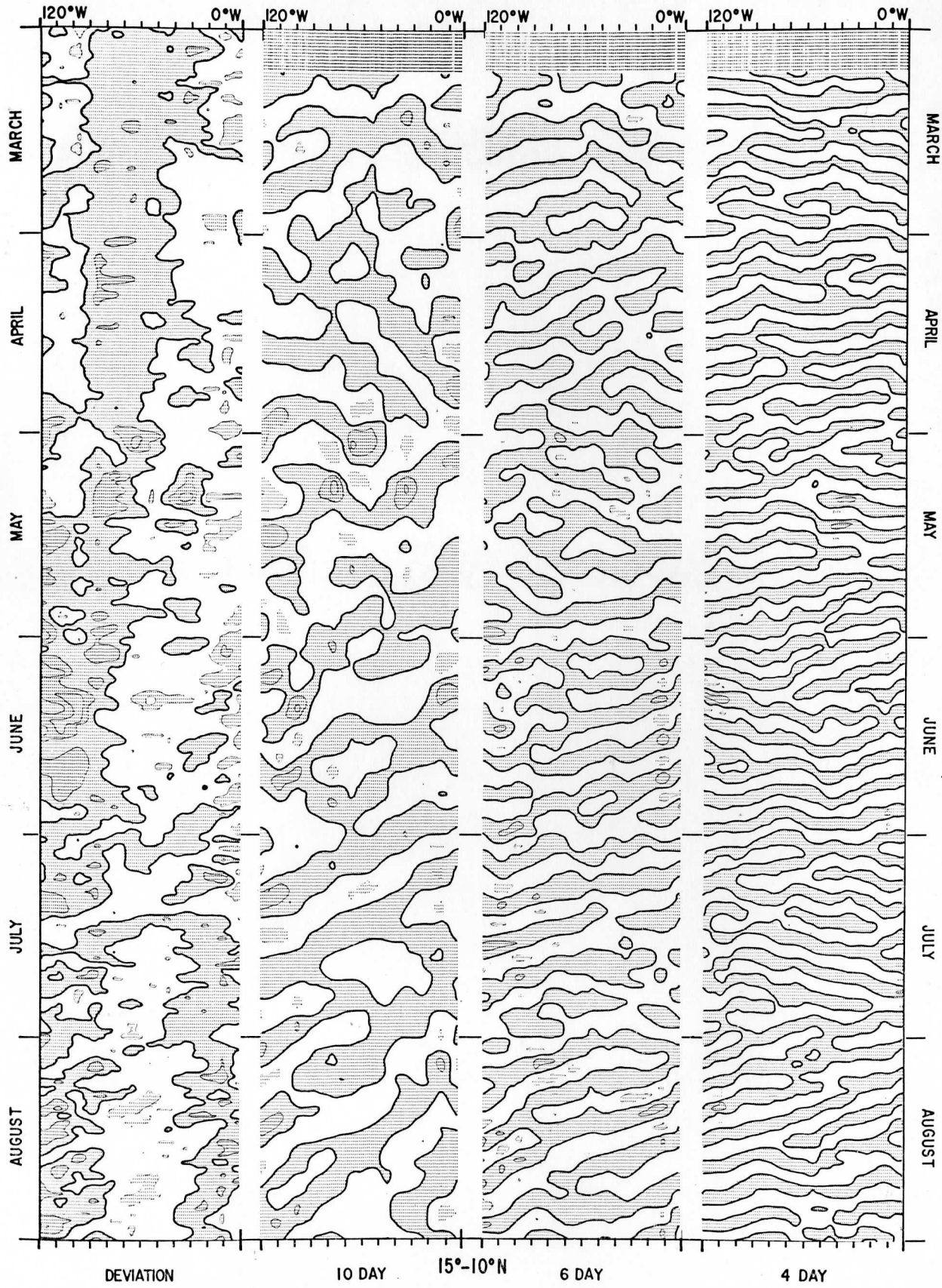
120°W
0°W
MARCH
APRIL
MAY
JUNE
JULY
AUGUST
DEVIATION
10 DAY
15°-10°N
6 DAY
4 DAY

Figure 2

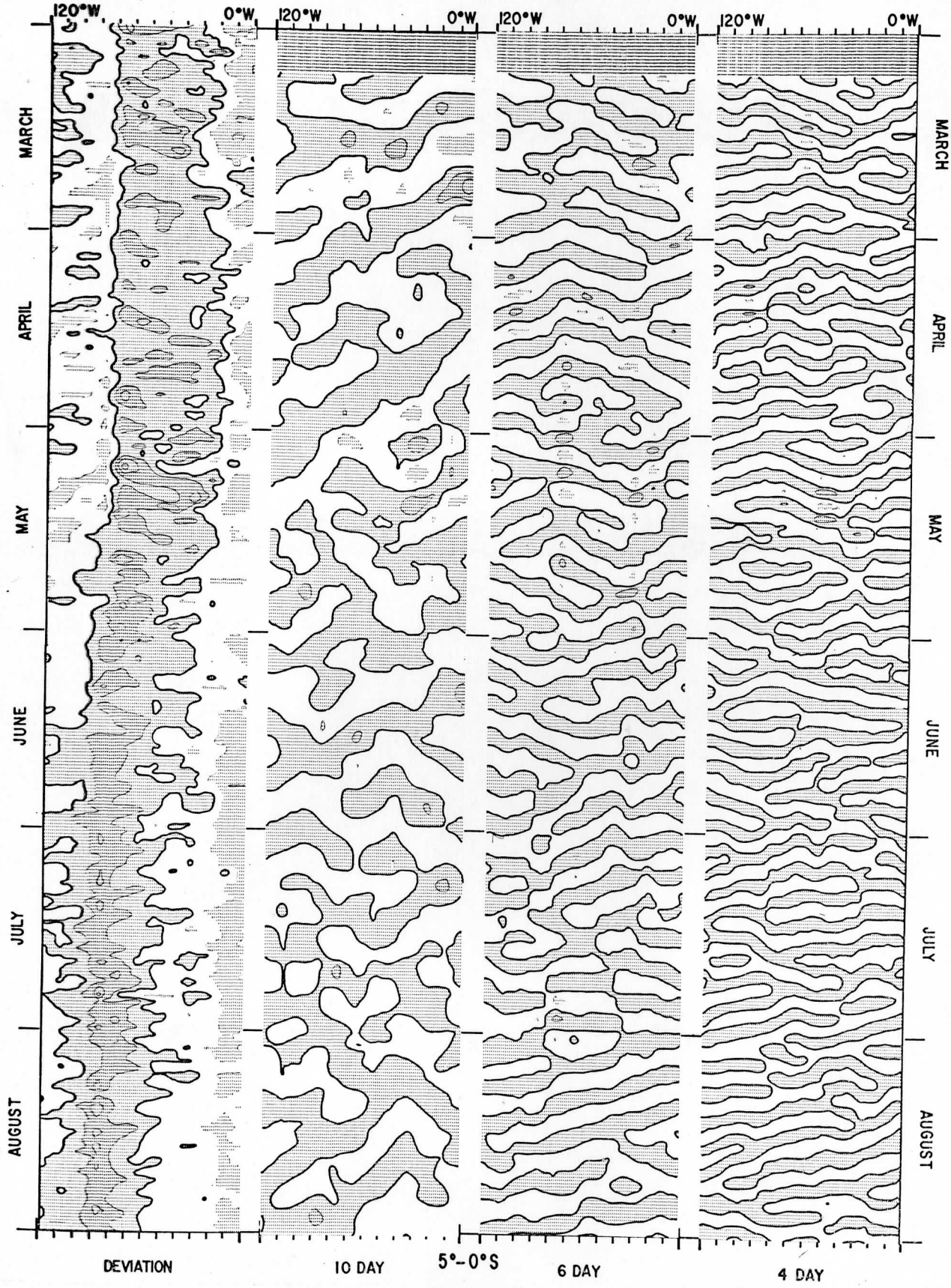
120°W
0°W
120°W
0°W
120°W
0°W
120°W
0°W
MARCH
APRIL
MAY
JUNE
JULY
AUGUST
MARCH
APRIL
MAY
JUNE
JULY
AUGUST
DEVIATION
10 DAY
5°-0°S
6 DAY
4 DAY

Figure 3

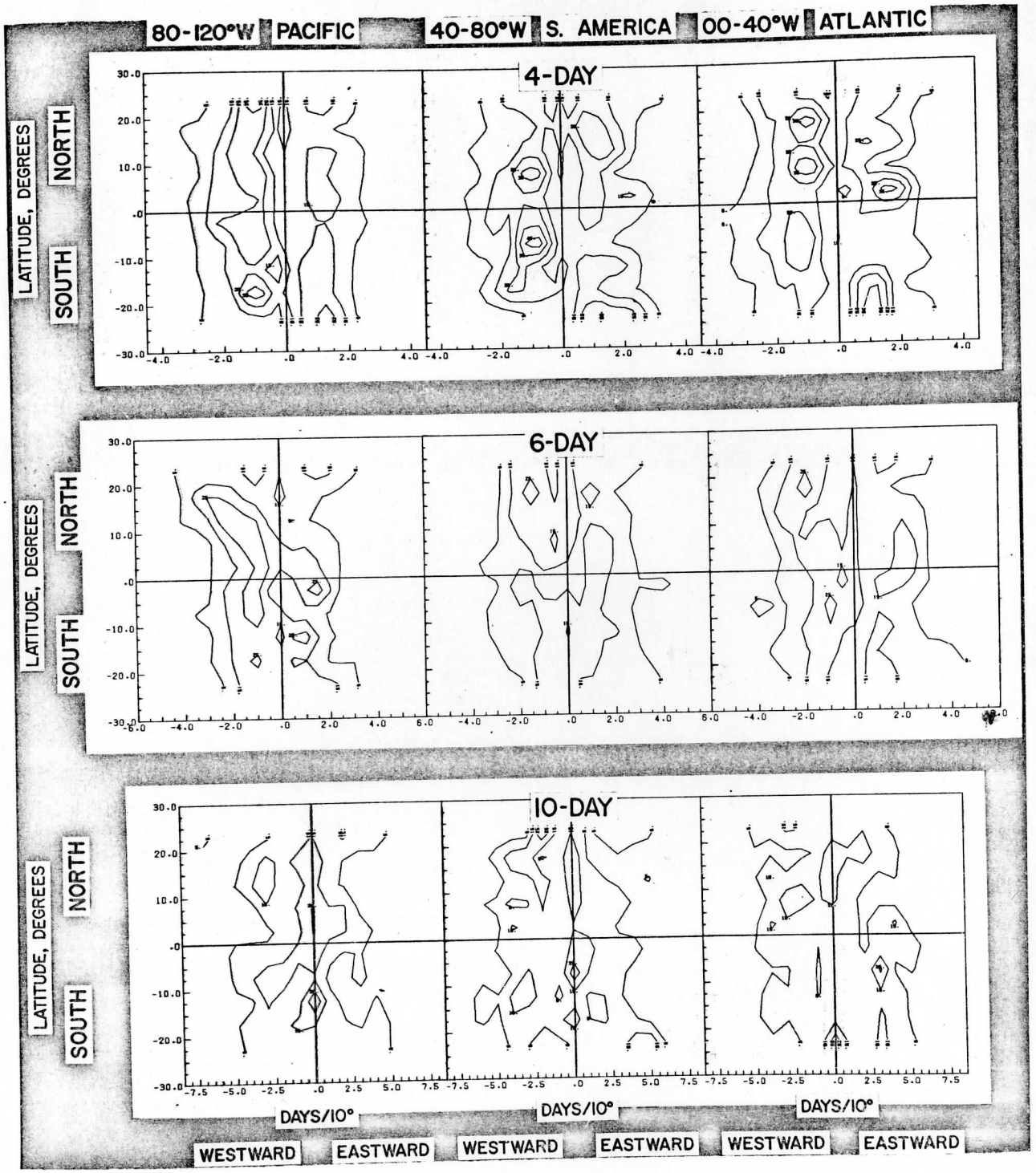
80-120°W PACIFIC
40-80°W S. AMERICA
00-40°W ATLANTIC
4-DAY
6-DAY
10-DAY
LATITUDE, DEGREES
NORTH
SOUTH
DAYS/10°
WESTWARD
EASTWARD

Figure 4

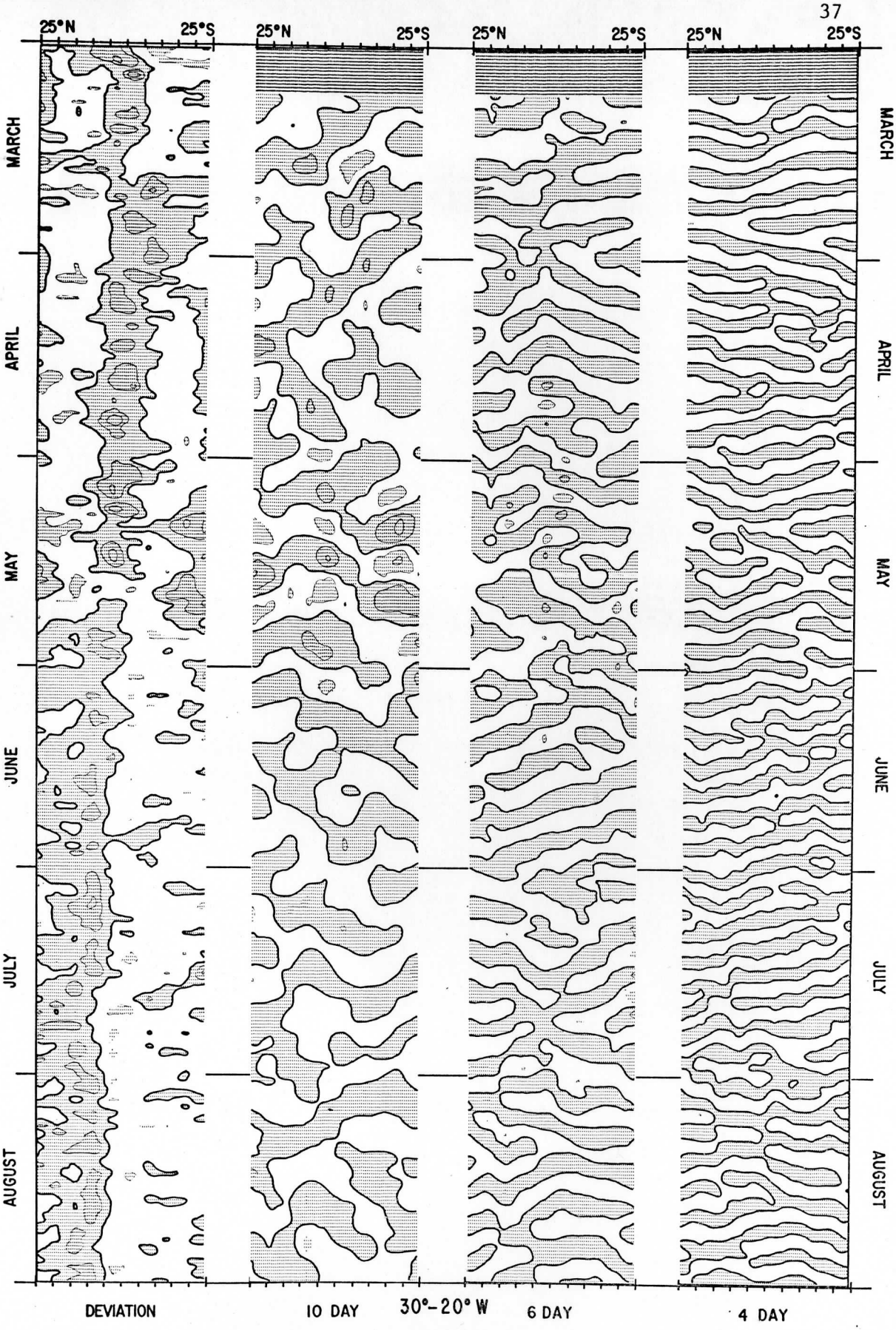
25°N
25°S
MARCH
APRIL
MAY
JUNE
JULY
AUGUST
DEVIATION
10 DAY
30°-20° W
6 DAY
4 DAY

Figure 5

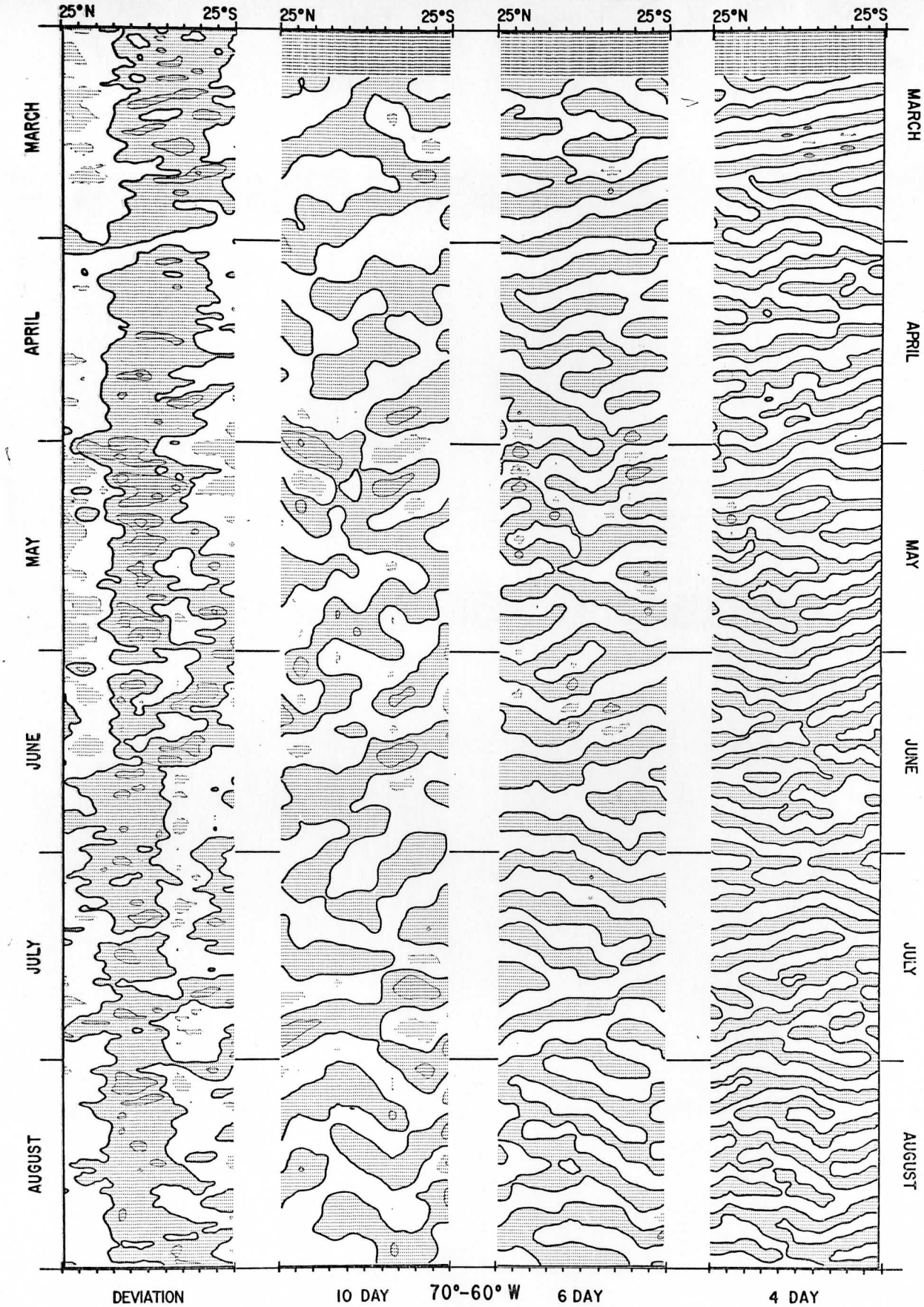
25°N
25°S
MARCH
APRIL
MAY
JUNE
JULY
AUGUST
DEVIATION
10 DAY
70°-60° W
6 DAY
4 DAY

Figure 6

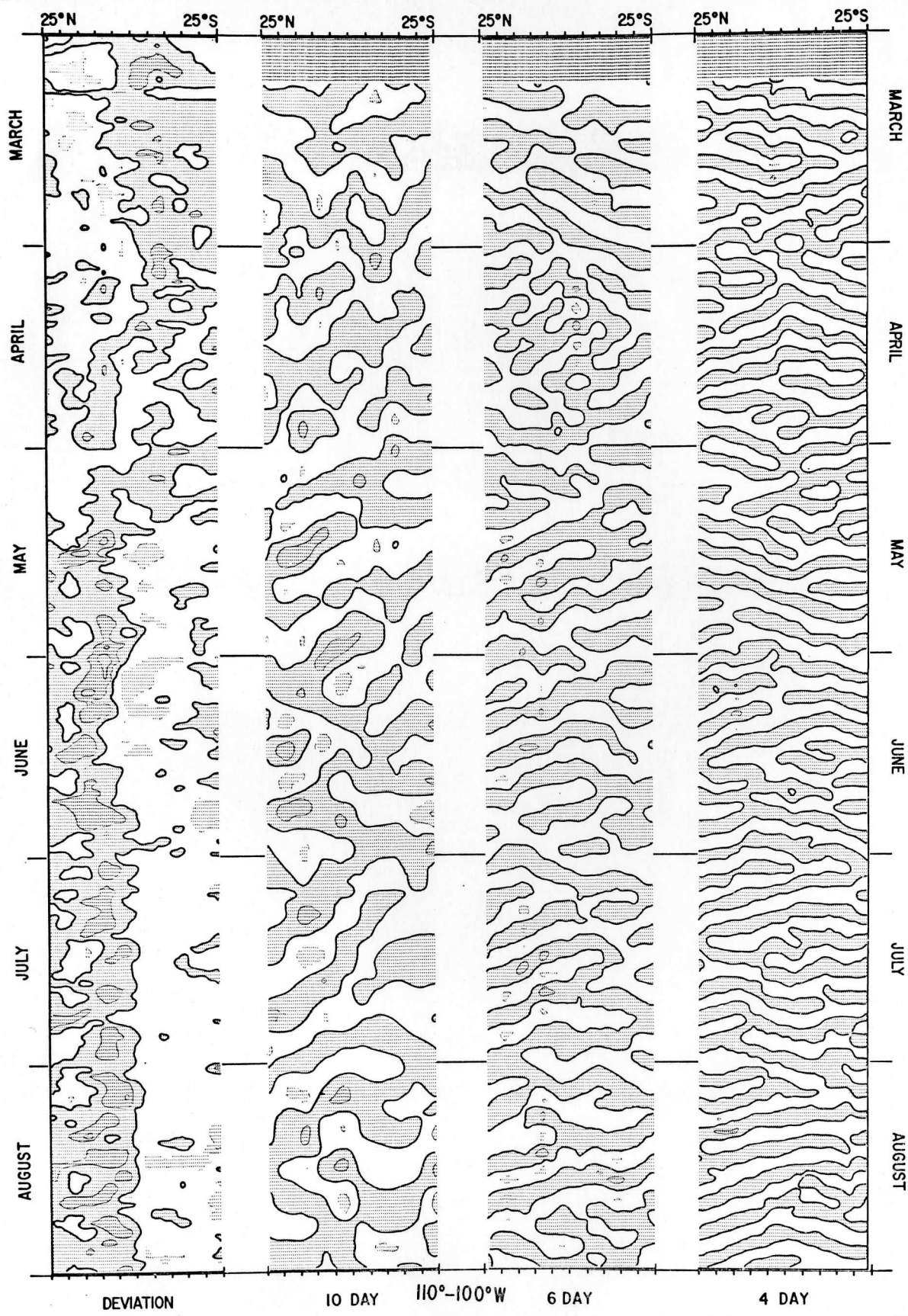
25°N
25°S
MARCH
APRIL
MAY
JUNE
JULY
AUGUST
DEVIATION
10 DAY
110°-100°W
6 DAY
4 DAY

Figure 7

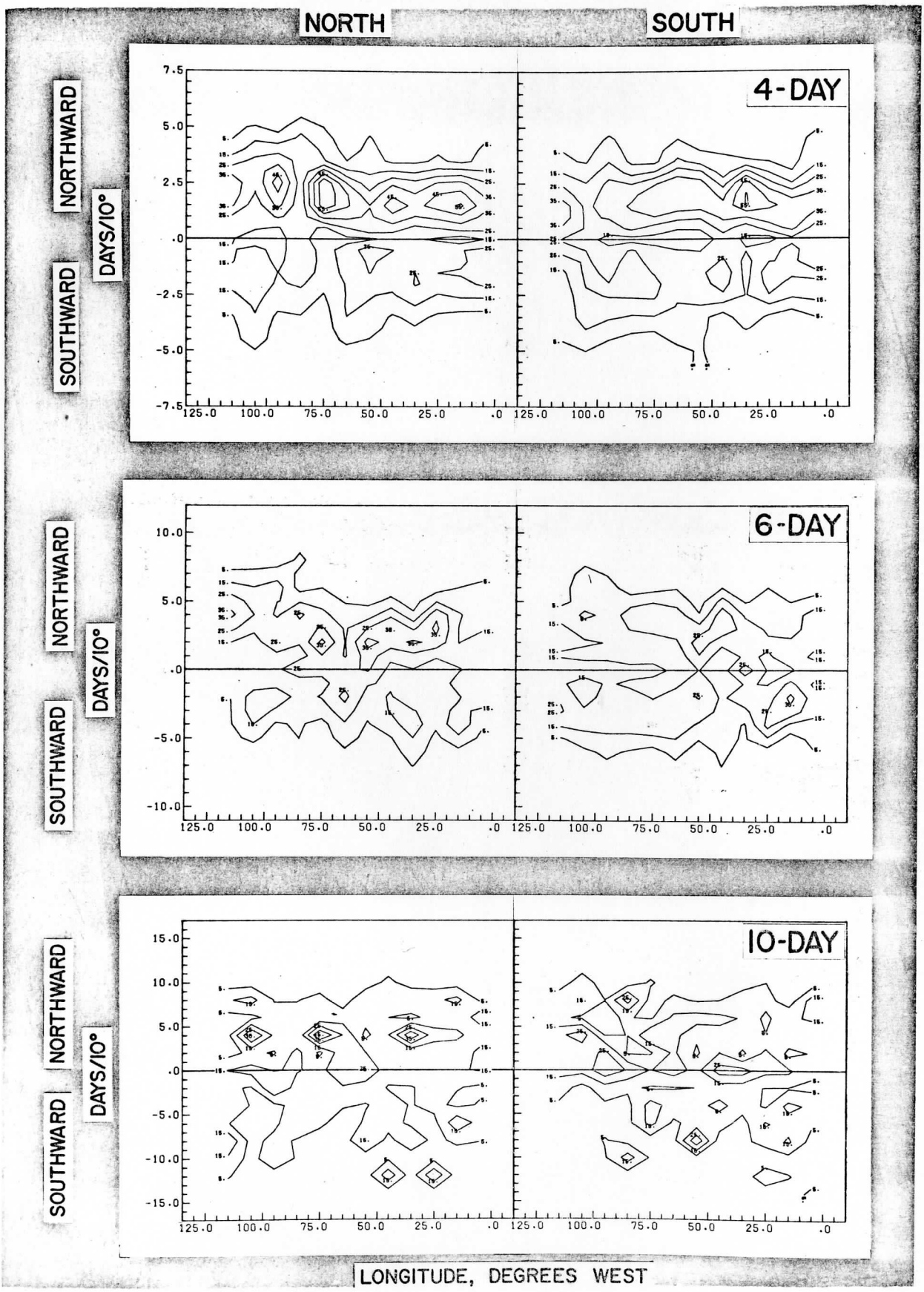

Figures 8a, 8b, 8c

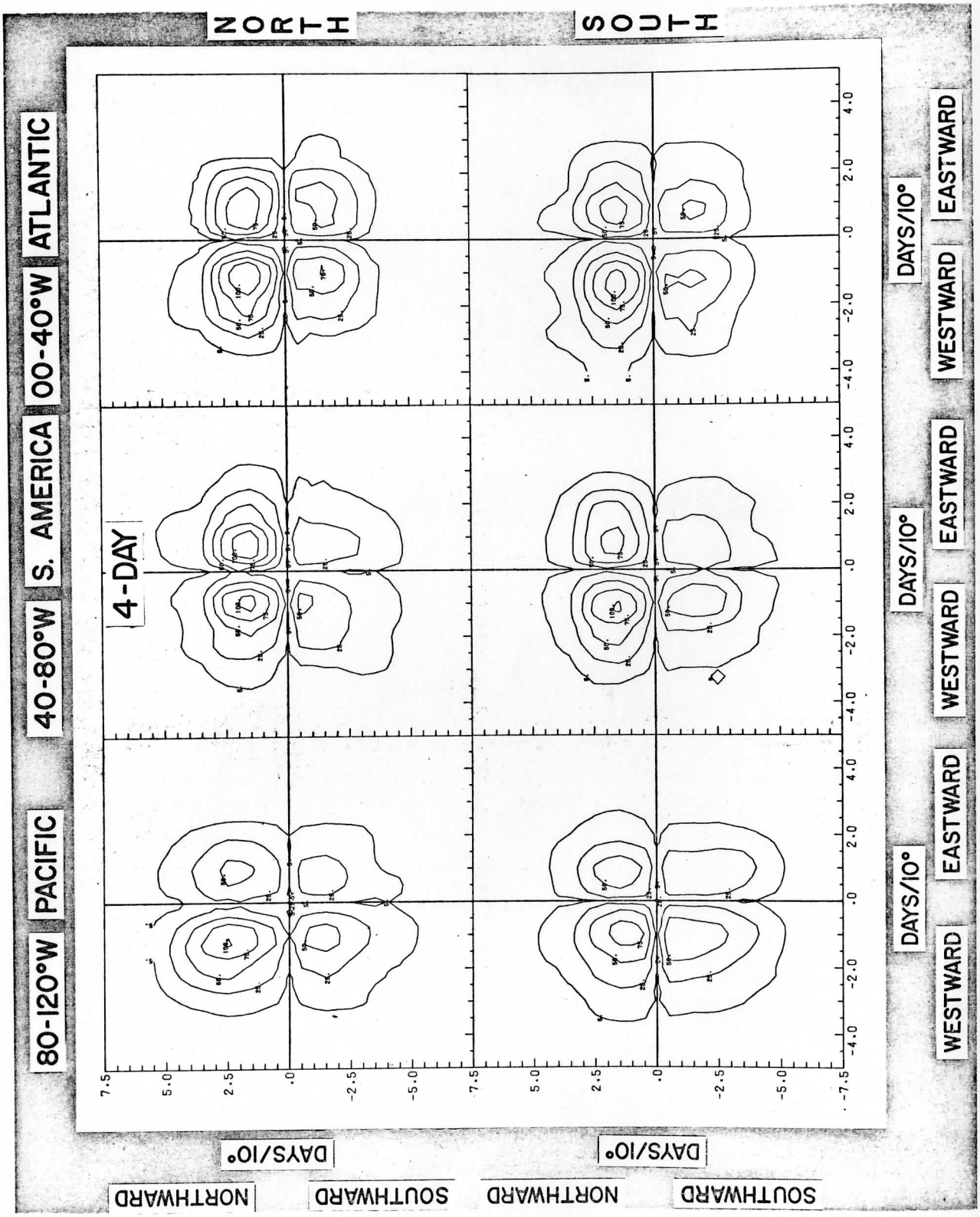
NORTH
SOUTH
80-120°W PACIFIC
40-80°W S. AMERICA
00-40°W ATLANTIC
4-DAY
7.5
5.0
2.5
.0
-2.5
-5.0
-7.5
4.0
2.0
-2.0
-4.0
DAYS/10°
NORTHWARD
SOUTHWARD
WESTWARD
EASTWARD

Figure 9a

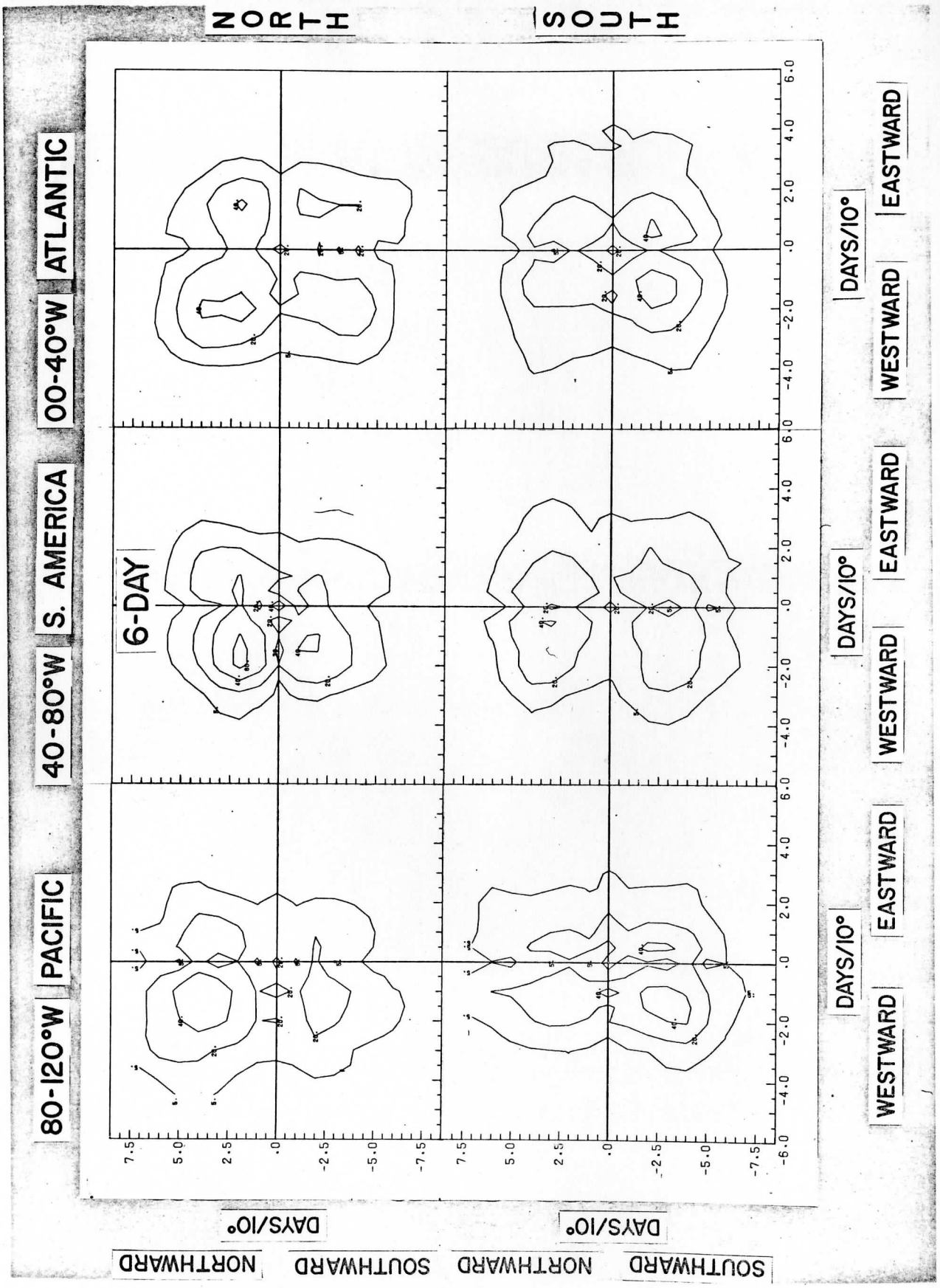
80-120°W
PACIFIC
40-80°W
S. AMERICA
00-40°W
ATLANTIC
NORTH
SOUTH
6-DAY
DAYS/10°
DAYS/10°
DAYS/10°
DAYS/10°
WESTWARD
EASTWARD
WESTWARD
EASTWARD
WESTWARD
EASTWARD
WESTWARD
EASTWARD
SOUTHWARD
NORTHWARD
SOUTHWARD
NORTHWARD

Figure 9b

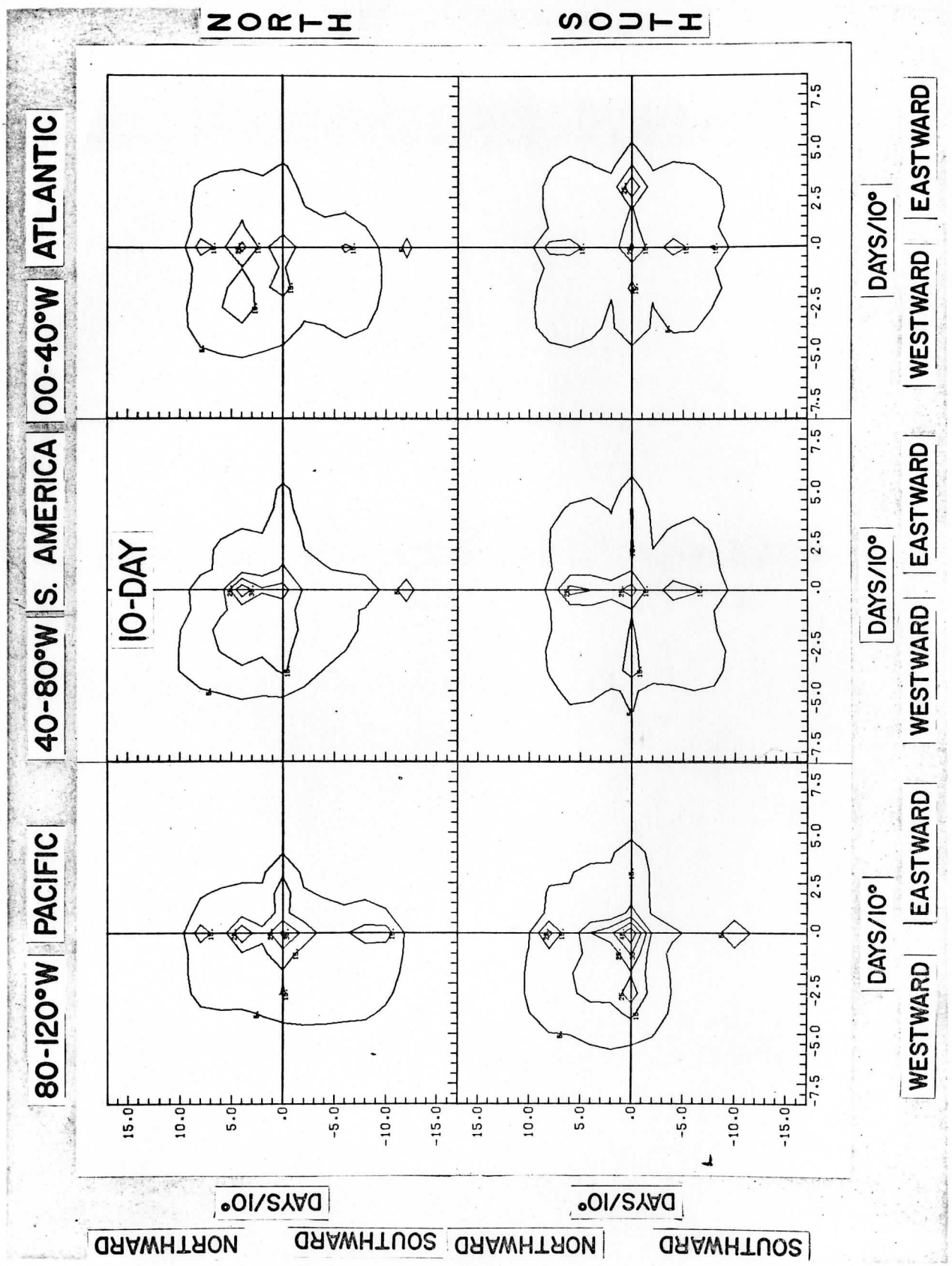
NORTH
SOUTH
80-120°W
PACIFIC
40-80°W
S. AMERICA
00-40°W
ATLANTIC
10-DAY
DAYS/10°
WESTWARD
EASTWARD
NORTHWARD
SOUTHWARD

Figure 9c

	Pacific				South America				Atlantic			
4-day filter	9	12	16	3	30	7	41	8	29	8	15	15
		9		32		19		26		19		20
	27	17	40	22	23	12	15	11	15	23	41	8
	24	3	18	4	4	8	26	27	35	19	25	39
		10		11		7		13		7		11
	38	10	28	14	25	6	54	31	21	4	25	0
6-day filter	2	14	6	7	8	25	2	23	3	17	13	2
		15		16		18		16		22		18
	30	6	17	17	16	19	19	13	7	27	24	12
	12	25	4	16	9	4	13	12	10	28	5	36
		11		8		7		12		9		8
	18	9	21	23	23	8	26	3	10	9	5	10
10-day filter	25	5	36	7	8	3	12	5	13	28	13	11
		21		24		21		22		7		26
	18	3	14	4	13	35	21	22	28	11	34	20
	12	16	9	3	0	3	7	5	18	42	23	28
		14		13		10		14		9		22
	10	10	14	1	27	29	24	23	27	8	26	8

Figure 10a

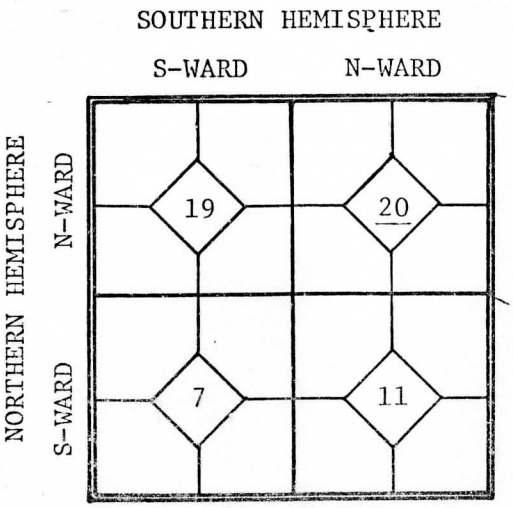

Figure 10b

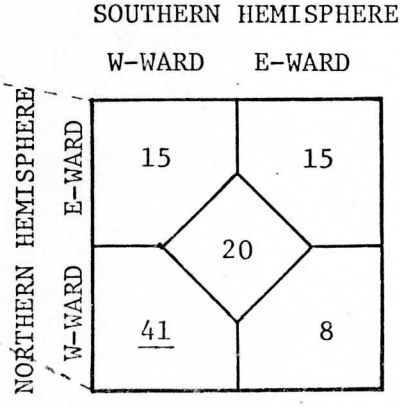

Figure 10c

A COMPARISON OF CLOUD MOTION WINDS EXTRACTED FROM SMS-I INFRARED IMAGES WITH COINCIDING RADIOSONDE WINDS OVER NORTH AMERICA

Kenneth G. Bauer

ABSTRACT

The relative capability of a wind derived from tracking the movement of clouds displayed in SMS-1 infrared image sequences and of a wind reported by a radiosonde to represent atmospheric motion was investigated. Cloud winds intercompared with radiosonde winds over North America gave mean absolute differences between a cloud wind and surrounding radiosonde winds of 4.4 $m \cdot s^{-1}$ for the u component and 4.6 $m \cdot s^{-1}$ for the v component. An intracomparison of radiosonde winds for the same periods gave mean absolute differences between a radiosonde wind and surrounding reports of 4.2 $m \cdot s^{-1}$ for the u component and 5.1 $m \cdot s^{-1}$ for the v component. These and associated results suggest a cloud wind and a radiosonde wind have a similar capability to represent atmospheric motions.

1. INTRODUCTION

A near continuous, detailed knowledge of atmospheric motion throughout the world will be an essential ingredient in the ultimate success of numerical modeling on a global basis. Presently the world's radiosonde network samples atmospheric structure and motion only twice each day over most land areas, while leaving the vast ocean areas essentially unsampled. Such sampling leaves spatial and temporal gaps in the knowledge of the changes taking place in the atmosphere. A significant portion of these sampling gaps can be filled by geostationary meteorological satellites. This, however, requires that data from the two different observation systems be effectively integrated into one data base, where at least the relative capability of the systems to represent the atmosphere must be known before they can be used synergistically for numerical modeling on a global basis.

A variety of time and space coincident comparisons over the most data-rich area of the world viewed by a Synchronous Meteorological

---

This article appeared in the July 1976 issue of the Monthly Weather Review, Vol. 104, No. 7, published by the American Meteorological Society, Boston.

Satellite (SMS)--the United States, Canada, and their environs--will be necessary to establish the relative capability of the two systems. This study investigates the relative capability of the two systems by comparing differences between each system's observations and a standard--the regional radiosonde network in the vicinity of the observation. It addresses (1) an intracomparison between wind reports from adjacent radiosonde stations, (2) an intercomparison between cloud motion winds extracted from SMS-1 infrared images and adjacent radiosonde wind reports, (3) an examination of cloud motion winds respective to their capabilities with regard to higher latitudes, the vertical, distances from the sub-point of a geostationary meteorological satellite, and (4) the speed of the cloud wind and the radiosonde wind. From these various investigations the degree to which a cloud motion wind and a radiosonde wind have a similar capability to represent atmospheric motion begins to emerge.

2. DATA BASE

Coinciding data in both time and space are essential to minimize, as much as possible, data extrapolation uncertainty. Such data were available for three synoptic times during the last two days of October 1974. Over that period SMS-1 images archived by the Space Science and Engineering Center (SSEC) spanned the radiosonde observations for most of North America made available to SSEC by the National Meteorological Center (NMC) of the National Weather Service (NWS). The 1200 GMT 30 October, and 0000 GMT and 1200 GMT 31 October 1974 data periods were chosen for this study. With North America in almost total darkness at 0000 GMT and 1200 GMT during the fall season only SMS-1 infrared images were used to obtain the cloud motion winds.

3. RADIOSONDE WIND INTRACOMPARISON

To measure the variation to be expected when comparing a wind report at one point in the atmosphere with wind reports in the surrounding atmosphere, a radiosonde wind to radiosonde wind intracomparison was made using the North America radiosonde data supplied by NMC. Each radiosonde was selected in turn as the base run for comparison with the three (minimum of two) closest radiosondes within a 660 km radius of the base location. Once the three comparison stations were identified, they were compared with the base station on a pressure level to pressure level and a height to height basis.

In the pressure level comparison the u and v components of a wind report at a standard pressure level at each of the comparison runs were extrapolated to the location of the base wind report by

fitting a plane through the three comparison reports and solving for the components at the location of the base station. The difference between the extrapolated u component and the base wind u component (u_{diff}) was then computed by subtracting the extrapolated u component from the base u component. The v_{diff} was computed in a similar fashion.

The height to height comparison was made by using the reported height of a standard pressure level of the base radiosonde run as the target height. The u and v components of the wind at this target height were derived for each of the comparison runs by matching the target height to the reported heights of the comparison radiosonde runs. Once the target height was bracketed between the two appropriate comparison heights, the u and v components of the wind at that target height were linearly interpolated from the u and v components of the bracketing wind reports. The comparison procedures from this point then followed those just described in the previous paragraph.

The results for the overall radiosonde intracomparison are summarized in Table 1. Both absolute values and algebraic values of u_{diff} and v_{diff} are shown. The pressure level and height comparison methods show little difference. For the height comparison the average value for the three cases of the mean absolute difference between a radiosonde wind report and other radiosonde wind reports extrapolated to the location of the target wind was 4.2 $m \cdot s^{-1}$ for the u_{diff} and 5.1 $m \cdot s^{-1}$ for the v_{diff}. The mean algebraic difference for the same comparison was 0 $m \cdot s^{-1}$ for the u_{diff} and .2 $m \cdot s^{-1}$ for the v_{diff}.

The results by latitude band are summarized in Table 2 for the height comparisons. Mean absolute u_{diff} values for the study range from 3.7 $m \cdot s^{-1}$ at 30°-35°N to 5.2 $m \cdot s^{-1}$ at 45°-50°N. The v_{diff} values range from 4.3 $m \cdot s^{-1}$ at 30°-35°N to 6.1 $m \cdot s^{-1}$ at 50°-55°N. Results in the vertical for the 35°-40°N latitude band given in Table 3 illustrate difference variations with altitude and time.

The results for latitude/longitude bounded zones for the height comparison method are summarized in Table 4. The locations of the bounded zones are shown in Figure 1. For meteorological reference, Figures 2 through 4 present the NMC 500 mb analysis for the periods considered. The considerable variation in mean absolute u_{diff} from 2.9 $m \cdot s^{-1}$ to 6.2 $m \cdot s^{-1}$ and in v_{diff} from 3.5 $m \cdot s^{-1}$ to 7.7 $m \cdot s^{-1}$, when compared with the 500 mb analyses, indicates the variability of the comparison results is linked to the weather pattern present during the comparison period.

4. CLOUD MOTION WIND

Cloud motion winds were extracted from SMS-1 infrared images using the SSEC developed Man-Computer Interactive Data Access System (McIDAS), a computer controlled, image storage, display, and processing device (Smith, 1975; Chatters and Suomi, 1975). Control of the McIDAS hardware and the execution of the scientist's commands were achieved through an integrated package of special computer software. The software allowed viewing of images via color television, navigation of images for geographical identification, variable rate "movie loop" display of image sequences, enlargement of selected features, black and white and/or false color enhancement, and rapid, exact operator-controlled cursor selection of areas within the data image. Although data were transformed to analog form for display (stored on an "instant replay" video disk), all computations were performed on untransformed digital data.

For the purposes of this investigation, a cloud distinguishable in a McIDAS black and white television display of SMS-1 infrared images was a candidate for tracking. Additionally, cloud movement was considered representative of atmospheric motion at cloud level. Only candidate clouds identifiable by the scientist throughout the picture sequence were tracked to determine their displacement with time. Image forms characteristically associated with orographic features were not included in the study. Gray-level enhancement was used to improve the definition of clouds in the pictures.

Correlation tracking was used to measure all cloud motions. This required the scientist to track each candidate cloud target by locating the cloud within a cursor-outlined, variable area rectangle in each picture of a time sequence. The computer then performed a correlation analysis to match the cloud image pattern in one picture with that in the next with the displacement of the pattern determining the cloud motion with time. Correlation tracking was the most accurate method available but required well defined clouds moving in a single layer flow pattern.

The height assigned to a cloud target was derived from the SMS-1 infrared data observed at the center of the cursor-defined rectangle with care being taken to center the rectangle on the cloud target. Assuming an emissivity of one for the target cloud, the blackbody temperature of the cloud was then estimated from the infrared data and converted to a cloud height by reference to standard atmospheric soundings corrected for latitude and date. Technical capability dictated the choice of this approach which does not consider variations in cloud emissivities or departures of the atmosphere from standard. Thus the effect of upwelling radiance from beneath could cause cloud temperatures to be overestimated (warmer) leading to underestimated

(lower) cloud heights. Also, the actual distribution of temperature showed (see Figure 3) a stronger east-west gradient than portrayed by the standard atmosphere implying additional uncertainty in the cloud height estimates. The detail of the study was not sufficient, however, to identify such effects.

A series of quality control measures was applied in deriving the cloud motion winds. Two consecutive, one-half hour duration cloud motion measurements were made using a sequence of three images to derive a cloud motion wind pair. Differences of greater than 4 $m \cdot s^{-1}$ between consecutive u components or v components caused measurements to be disregarded. Consecutive cloud height determinations were also made with the wind pair measurements disregarded if the first and second heights, represented by 100 mb layers, did not fall in the same or an adjacent layer. Cases where the point of highest correlation between consecutive cloud images occurred on the edge of the data during the correlation tracking were considered inconclusive and not used. Finally, cloud wind pairs meeting these control conditions were plotted as arrow vectors coincident in time and space with the sequence of SMS-1 infrared images. The cloud wind vector plots were grouped into four vertical layers with each layer displayed in a distinctive color to aid in rapid, positive identification. Cloud wind vectors found by the experienced meteorologist performing the investigation to be inconsistent with the atmospheric flow patterns portrayed by the clouds and other derived winds, as the composite images were viewed repetitively in sequence, were also eliminated from the study.

5. CLOUD WIND/RADIOSONDE WIND INTERCOMPARISON

During the intercomparison periods, clouds were present for tracking in the infrared over most of the central and eastern United States and southeast Canada at 1200 GMT on the 30th, with fewer present at 0000 GMT and 1200 GMT on the 31st. Three image sequences of full resolution SMS-1 infrared [(1130 GMT = T_1 (time 1), 1200 GMT = T_2, 1230 GMT = T_3) or (2330 GMT = T_1, 0000 GMT = T_2, 0030 GMT = T_3)] bracketing the 0000 GMT or 1200 GMT radiosonde observation times were used. The change in position of a selected cloud from T_1 to T_2 produced the first cloud motion wind and the change in position from T_2 to T_3 of the same cloud produced a second cloud motion wind. The averaged u and the averaged v components of the two cloud motion winds (meeting the quality control criteria), positioned at the averaged latitude and averaged longitude of the two cloud wind positions, were the cloud motion winds compared with the radiosonde wind reports.

The intercomparison between a cloud wind and radiosonde wind reports from the surrounding atmosphere was carried out in the same manner as used for a height comparison of a radiosonde wind described previously. The reported height of the cloud wind was the target height of the comparison. The difference between the u (v) component of the cloud wind and the u (v) component of the radiosonde interpolated/extrapolated wind was then computed in the form:

$$u_{diff} = u_{cloud} - u_{sonde} ,$$

$$v_{diff} = v_{cloud} - v_{sonde} .$$

In this formulation a positive difference indicates a stronger easterly (less westerly) u_{cloud} component or a stronger northerly (less southerly) v_{cloud} component.

For the 1200 GMT 30 October comparison 223 cloud winds meeting quality control criteria were measured from the SMS-1 infrared images. Only 61 cloud winds could be measured for the 0000 GMT 31 October comparisons--the number of cloud winds measured being directly related to the number, form, and distribution of target clouds. 112 cloud winds were measured for the 1200 GMT 31 October comparison.

The results for the overall cloud wind/radiosonde wind intercomparison are summarized in Table 5. When averaged over the three periods, the mean absolute cloud wind u_{diff} was 4.4 $m \cdot s^{-1}$ compared to 4.2 $m \cdot s^{-1}$ for the radiosonde intracomparison for the same period. The mean absolute cloud wind v_{diff} was 4.6 $m \cdot s^{-1}$ compared to 5.1 $m \cdot s^{-1}$ for the radiosonde intracomparison.

The results summarized by latitude band are given in Table 6. For the 1200 GMT 30 October comparison period the mean absolute cloud wind u_{diff} ranged from 3.0 $m \cdot s^{-1}$ at 35°-40°N to 7.3 $m \cdot s^{-1}$ at 25°-30°N. The v_{diff} values ranged from 2.6 $m \cdot s^{-1}$ at 50°-55°N to 4.9 $m \cdot s^{-1}$ at 30°-35°N. These results are comparable to those from the radiosonde intracomparison for the same period where u_{diff} ranged from 3.6 $m \cdot s^{-1}$ to 5.9 $m \cdot s^{-1}$ and v_{diff} ranged from 4.2 $m \cdot s^{-1}$ to 6.2 $m \cdot s^{-1}$.

The results for latitude/longitude bounded zones are summarized in Table 7. A comparison of the mean absolute differences found during the radiosonde intracomparison with those found during the cloud wind/radiosonde wind intercomparison for the 35°-45°N, 65-85°W zone at 1200 GMT 30 October is given in Figure 5. The mean absolute u_{diff} for all levels was 3.4 $m \cdot s^{-1}$ for the cloud wind intercomparison and 3.0 $m \cdot s^{-1}$ for the radiosonde intracomparison. The mean absolute v_{diff} for all levels was 3.3 $m \cdot s^{-1}$ for the cloud wind intercomparison and 3.4 $m \cdot s^{-1}$ for the radiosonde intracomparison. The variation with height of both

comparison techniques is quite pronounced. The relatively uniform distribution in the vertical of numbers of observed cloud winds illustrates the effectiveness of the system in tracking clouds at all levels.

6. INFLUENCE OF GEOGRAPHICAL AND METEOROLOGICAL FACTORS

To effectively use cloud motion winds derived from SMS-1 images, it is essential to know to what extent their relative capability with respect to radiosonde winds is influenced by geographical and meteorological factors; i.e., are atmospheric motions better represented in one location or situation than another? Examining the location factors, Figures 6 through 8 show plots of u_{diff} and v_{diff} versus latitude, height, and distance from satellite subpoint for the 365 cloud wind pairs discussed in Section 5. No discernible variations with latitude, height, or distance from satellite subpoint are evident in Figures 6 through 8. The distributions of u_{diff} and v_{diff} are similar indicating no systematic bias in cloud winds. These results suggest cloud winds can be effective at all levels for the United States, southern Canada, and adjoining oceans which, in turn, suggests their effective use for any region viewed by geostationary satellite having similar distance and latitude characteristics.

The meteorological situation may be a factor related to the utility of cloud winds. Figures 9 and 10 show plots of u_{diff} and v_{diff} versus cloud wind speed and sonde wind speed as indicators of the meteorological situation being sampled for the 365 cloud wind pairs. Figure 9 shows no discernible trends but this does not seem to be the case for Figure 10, however. There, some trend toward increasing positive values of u_{diff} as sonde wind speeds decrease (below approximately 15 $m \cdot s^{-1}$) and for increasing negative values of u_{diff} as sonde wind speeds increase (above approximately 15 $m \cdot s^{-1}$) may be indicated. In contrast, such a distribution with variations in sonde wind speed is not evident with respect to the v_{diff} plot in Figure 10. These results suggest further investigations must be made to establish if the height determination and/or some other factors, such as the complicated nature of cumulus motion (Fujita et al., 1975), may be influencing the cloud wind system.

7. VARIATION IN RADIOSONDE WINDS

In comparing cloud winds with radiosonde winds it is also necessary to have an estimate of how effectively radiosonde reports portray the motions of the atmosphere and the range of observational variability to be expected in them. One facet to be examined is, given a complete,

unprocessed radiosonde observation run, how much variation can be expected in wind reports determined from it by two different computational methods? Fuelberg (1974) presented such a comparison for radiosonde runs taken in May 1974 at three different sites in the midwestern United States (Peoria, IL; Flint, MI; St. Cloud, MN). He compared the results obtained from applying the computational method of the Atmospheric Variability Experiment (AVE), where additional tracking data and all pressure contact results were incorporated into the computation, with the routine wind reports transmitted by the National Weather Service. He found "... no large difference between results of the two procedures, even in areas of high wind speed." However, on a level by level comparison of the absolute difference between the u and v components of the NWS and AVE methods, results averaged over all levels for the three cases show a u_{diff} of 1.7 $m \cdot s^{-1}$ and a v_{diff} of 1.1 $m \cdot s^{-1}$. Plots of the u_{diff}, v_{diff}, and $speed_{diff}$, averaged for the three cases over selected levels, are given in Figure 11. They portray quite clearly the differences that can occur, particularly with increasing height.

Another facet to examine is measurement errors caused by uncertainty in the tracking procedures. These can exceed 20 $m \cdot s^{-1}$ under high wind conditions as illustrated in Table 8 which shows the RMS vector error determined for a AN/GMD-1A rawin set used at the Atlantic Missile Range (USAF, 1963).

A third facet to consider is atmospheric variability in the horizontal. Arnold (1956) provides (Table 9) values of the average magnitude of the vectorial difference in the winds measured by two radiosondes launched near simultaneously at different distances from each other. At 600 km, the maximum distance between comparison wind reports in this study, Arnold's values reach 8 $m \cdot s^{-1}$, illustrating the considerable increase in differences between two wind measurements as the horizontal distance between them increases. The data collected by Arnold contain several years of observations but extend only to 7 km eliminating effects of higher level jet stream winds.

8. SUMMARY

The relative capability of a cloud motion wind and a radiosonde wind to represent atmospheric motion was investigated. Radiosonde winds were intracompared over North America for three synoptic times resulting in mean absolute differences between a radiosonde wind and surrounding radiosonde wind reports of 4.2 $m \cdot s^{-1}$ for the u component and 5.1 $m \cdot s^{-1}$ for the v component. Cloud motion winds were derived from sequences of SMS-1 infrared images by the McIDAS cloud motion

tracking system for the same three synoptic times. The cloud motion winds were intercompared with radiosonde winds resulting in mean absolute differences between a cloud wind and surrounding radiosonde winds of 4.4 $m \cdot s^{-1}$ for the u component and 4.6 $m \cdot s^{-1}$ for the v component. Similar comparisons by latitude bands and latitude/longitude zones were presented as well as examples of variations in the vertical. The influence of geographical and meteorological factors on the relative capability of cloud winds with respect to radiosonde winds was examined. No systematic bias with respect to latitude, height, or distance from satellite subpoint was found. A possible variation of differences in the u component with changes in radiosonde wind speed was noted. Such a variation did not appear with respect to cloud wind speeds. Variations in radiosonde wind reports, as influenced by computational techniques, tracking uncertainties, and atmospheric variations, were found to be considerable.

The results of this investigation suggest that a cloud motion wind and a radiosonde wind have a similar capability to represent atmospheric motions. Over the area and times examined here it would seem the differences between cloud motion winds and radiosonde winds fall within the limits determined by computational techniques, observational methods, and atmospheric variability. This being the case, cloud motion winds should be capable of representing atmospheric motion at any level with distinguishable clouds over any region viewed by a geostationary satellite having similar latitude and distance characteristics to those represented in this study by the United States, Canada, and adjoining oceans.

ACKNOWLEDGEMENTS

Discussions with and comments by F. Mosher were most helpful. The McIDAS support of J. T. Young, G. Chatters, J. M. Benson, and E. Suomi is gratefully acknowledged. Programming support by B. Sawyer and R. Linn and consulting by T. Whittaker were key items. Drafting was done by D. Wooldridge with data preparation support provided by T. Schreiner. Radiosonde data were provided by the National Meteorological Center through the much appreciated efforts of H. O'Neil. The research was supported by the National Oceanic and Atmospheric Administration under Grant 04-3-158-61.

REFERENCES

Arnold, A., 1956: Representative Winds Aloft. BAMS, 37, 27-30.

Chatters, G. C. and V. E. Suomi, 1975: The Applications of McIDAS, IEEE Trans. on Geoscience Electronics, GE-13, 3, 137-146.

Fuelberg, H. E., 1974: Reduction and Error Analysis of the AVE II Pilot Experiment Data. NASA CR-120496. George C. Marshall Space Flight Center, AL, 97 pp.

Fujita, T. T., E. W. Pearl, and W. E. Shenk, 1975: Satellite-Tracked Cumulus Velocities. J. Appl. Meteor., 14, 407-413.

Smith, E., 1975: Man-Computer Interactive Data Access System. IEEE Trans. on Geoscience Electronics, GE-13, 3, 123-136.

Unites States Air Force, 1963: Meteorological Handbook. AFMTCP 105, Air Force Missile Test Center, Patrick AFB, FL, 12 pp.

TABLE 1. RADIOSONDE WIND REPORT INTRACOMPARISON--OVERALL

Date:	30 October		31 October		31 October		Average	
Time:	1200 GMT		0000 GMT		1200 GMT			
Radiosonde runs intracompared	90		87		93			
Comparison method	Pressure	Height	Pressure	Height	Pressure	Height	Pressure	Height
Radiosonde winds compared	757	719	740	700	808	765		
Mean absolute values ($m \cdot s^{-1}$)								
u_{diff}	4.2	4.3	4.1	4.2	4.1	4.2	4.1	4.2
v_{diff}	5.0	5.1	5.0	5.1	4.8	5.1	4.9	5.1
u_{diff} standard deviation	4.3	4.4	4.5	4.6	4.1	4.2	4.3	4.4
v_{diff} standard deviation	5.5	5.8	6.1	6.1	5.9	6.5	5.8	6.1
Mean algebraic values ($m \cdot s^{-1}$)								
u_{diff}	0.0	0.0	-0.2	-0.2	0.1	0.1	0.0	0.0
v_{diff}	0.4	0.5	0.6	0.6	-0.4	-0.4	0.2	0.2
u_{diff} standard deviation	6.1	6.1	6.1	6.2	5.8	6.0	6.0	6.1
v_{diff} standard deviation	7.4	7.7	7.8	7.9	7.6	8.2	7.6	7.9

TABLE 2. RADIOSONDE WIND REPORT INTRACOMPARISON--
LATITUDE BANDS (HEIGHT)

Date: / Time:	30 October 1200 GMT	31 October 0000 GMT	31 October 1200 GMT	Average
Band		25°-35°N		
Radiosonde runs intracompared	10	9	11	
Radiosonde winds compared	83	69	96	
Mean absolute u_{diff} ($m \cdot s^{-1}$)	5.9	4.3	3.8	4.7
Mean absolute v_{diff} ($m \cdot s^{-1}$)	5.0	5.7	3.9	4.9
Band		30°-35°N		
Radiosonde runs intracompared	15	14	16	
Radiosonde winds compared	122	113	126	
Mean absolute u_{diff} ($m \cdot s^{-1}$)	4.1	2.7	4.2	3.7
Mean absolute v_{diff} ($m \cdot s^{-1}$)	6.0	3.6	3.4	4.3
Band		35°-40°N		
Radiosonde runs intracompared	19	20	20	
Radiosonde winds compared	153	162	161	
Mean absolute u_{diff} ($m \cdot s^{-1}$)	3.6	3.5	4.3	3.8
Mean absolute v_{diff} ($m \cdot s^{-1}$)	4.8	4.7	5.1	4.9
Band		40°-45°N		
Radiosonde runs intracompared	20	20	21	
Radiosonde winds compared	159	151	175	
Mean absolute u_{diff} ($m \cdot s^{-1}$)	3.6	4.6	3.9	4.0
Mean absolute v_{diff} ($m \cdot s^{-1}$)	4.2	4.6	5.0	4.6
Band		45°-50°N		
Radiosonde runs intracompared	12	11	12	
Radiosonde winds compared	93	91	94	
Mean absolute u_{diff} ($m \cdot s^{-1}$)	4.9	6.3	4.3	5.2
Mean absolute v_{diff} ($m \cdot s^{-1}$)	5.1	6.5	6.5	6.0
Band		50°-55°N		
Radiosonde runs intracompared	9	9	8	
Radiosonde winds compared	73	79	68	
Mean absolute u_{diff} ($m \cdot s^{-1}$)	4.5	4.9	4.5	4.6
Mean absolute v_{diff} ($m \cdot s^{-1}$)	6.2	5.9	6.1	6.1

TABLE 3. RADIOSONDE WIND REPORT INTRACOMPARISON--VERTICAL COMPARISON FOR THE 35°-40°N LATITUDE BAND

Date:	30 October 1200 GMT		31 October 0000 GMT		31 October 1200 GMT		Average	
Time:								
Component ($m \cdot s^{-1}$):	u_{diff}	v_{diff}	u_{diff}	v_{diff}	u_{diff}	v_{diff}	u_{diff}	v_{diff}
Vertical Layer # winds								
13.0 to 13.9 km 19,17,17	3.5	1.9	2.7	4.6	3.9	3.4	3.4	3.3
12.0 to 12.9 km 13,11,11	3.0	2.4	2.8	4.2	2.3	3.6	2.7	3.4
11.0 to 11.9 km 6, 8, 9	3.9	9.8	4.4	7.9	5.6	5.1	4.6	7.6
10.0 to 10.9 km 19,19,20	4.8	7.8	3.8	6.8	4.9	6.7	4.5	7.1
9.0 to 9.9 km 19,19,20	3.2	6.0	4.8	8.0	5.4	7.2	4.5	7.1
8.0 to 8.9 km								
7.0 to 7.9 km 19,19,20	4.0	4.9	3.2	3.6	6.2	5.6	4.5	4.7
6.0 to 6.9 km								
5.0 to 5.9 km 19,20,20	4.1	4.6	3.1	3.3	3.2	5.6	3.5	4.5
4.0 to 4.9 km								
3.0 to 3.9 km 17,19,19	1.7	3.6	3.8	2.9	3.8	4.4	3.1	3.6
2.0 to 2.9 km								
1.0 to 1.9 km 14,16,15	2.6	2.7	4.0	3.5	3.3	3.9	3.3	3.4

TABLE 4. RADIOSONDE WIND REPORT INTRACOMPARISON--
LATITUDE/LONGITUDE BOUNDED ZONES (HEIGHT COMPARISON)

Date (October 1974):	30	31	31		30	31	31		30	31	31	
Time (GMT):	1200	0000	1200	avg	1200	0000	1200	avg	1200	0000	1200	avg
Zone:		25°-35°N 65°-85°W				25°-35°N 85°-105°W				25°-35°N 105°-125°W		
Radiosonde winds compared	55	40	54		105	97	105		45	45	63	
Mean absolute u_{diff} ($m \cdot s^{-1}$)	4.7	2.5	3.3	3.5	3.1	3.1	4.3	3.5	9.2	4.5	4.1	5.9
Mean absolute v_{diff} ($m \cdot s^{-1}$)	6.0	2.6	2.5	3.7	2.8	3.5	4.2	3.5	11.5	7.8	3.7	7.7
Zone:		35°-45°N 65°-85°W				35°-45°N 85°-105°W				35°-45°N 105°-125°W		
Radiosonde winds compared	113	116	120		118	102	119		81	95	90	
Mean absolute u_{diff} ($m \cdot s^{-1}$)	3.0	2.8	2.8	2.9	4.0	5.4	5.0	4.8	3.8	4.1	4.6	4.2
Mean absolute v_{diff} ($m \cdot s^{-1}$)	3.4	3.8	4.1	3.8	4.3	5.6	4.9	4.9	6.3	4.7	6.6	5.9
Zone:		45°-55°N 65°-85°W				45°-55°N 85°-105°W				45°-55°N 105°-125°W		
Radiosonde winds compared	55	50	56		37	32	19		47	59	60	
Mean absolute u_{diff} ($m \cdot s^{-1}$)	3.7	7.3	5.6	5.5	5.8	4.8	8.1	6.2	4.6	5.8	3.0	4.5
Mean absolute v_{diff} ($m \cdot s^{-1}$)	4.1	8.9	9.1	7.4	4.2	4.5	6.0	4.9	7.8	6.0	4.9	6.2

TABLE 5. CLOUD WIND/RADIOSONDE WIND INTERCOMPARISON--
OVERALL SUMMARY

Date: / Time:	30 October 1200 GMT	31 October 0000 GMT	31 October 1200 GMT	Average
Total Cloud Winds Compared	208	48	106	121
Mean Absolute Values ($m \cdot s^{-1}$)				
u_{diff}	4.3	4.3	4.5	4.4
v_{diff}	4.1	3.9	5.9	4.6
u_{diff} standard deviation	4.3	3.9	4.7	4.3
v_{diff} standard deviation	4.1	3.4	5.1	4.2
Mean Algebraic Values ($m \cdot s^{-1}$)				
u_{diff}	-0.4	-0.5	1.8	0.3
v_{diff}	-1.0	1.4	-0.1	0.1
u_{diff} standard deviation	6.1	5.8	6.3	6.1
v_{diff} standard deviation	5.7	4.9	7.9	6.2

TABLE 6. CLOUD WIND/RADIOSONDE WIND INTERCOMPARISON--LATITUDE BAND

Date: / Time:	30 October 1200 GMT	31 October 0000 GMT	31 October 1200 GMT	Average
Band		25°-30°N		
Cloud winds compared	26	2	17	15
Mean absolute u_{diff} ($m \cdot s^{-1}$)	7.3	4.2	7.1	7.1
Mean absolute v_{diff} ($m \cdot s^{-1}$)	4.8	0.7	3.7	4.2
Band		30°-35°N		
Cloud winds compared	31	10	17	19
Mean absolute u_{diff} ($m \cdot s^{-1}$)	3.4	4.5	3.5	3.6
Mean absolute v_{diff} ($m \cdot s^{-1}$)	4.9	2.2	3.5	4.0
Band		35°-40°N		
Cloud winds compared	47	11	23	27
Mean absolute u_{diff} ($m \cdot s^{-1}$)	3.0	2.1	4.3	3.2
Mean absolute v_{diff} ($m \cdot s^{-1}$)	3.1	3.3	8.4	4.6
Band		40°-45°N		
Cloud winds compared	44	11	27	27
Mean absolute u_{diff} ($m \cdot s^{-1}$)	4.3	6.6	3.0	4.2
Mean absolute v_{diff} ($m \cdot s^{-1}$)	4.6	4.9	7.4	5.6
Band		45°-50°N		
Cloud winds compared	44	10	9	21
Mean absolute u_{diff} ($m \cdot s^{-1}$)	5.1	4.0	4.5	4.8
Mean absolute v_{diff} ($m \cdot s^{-1}$)	4.1	6.0	4.8	4.5
Band		50°-55°N		
Cloud winds compared	10	0	8	6
Mean absolute u_{diff} ($m \cdot s^{-1}$)	4.1		3.6	3.9
Mean absolute v_{diff} ($m \cdot s^{-1}$)	2.6		4.2	3.3

TABLE 7. CLOUD WIND/RADIOSONDE WIND INTERCOMPARISON--
LATITUDE/LONGITUDE BOUNDED ZONES

Date (October 1974):	30	31	31		30	31	31		30	31	31	
Time (GMT):	1200	0000	1200	avg	1200	0000	1200	avg	1200	0000	1200	avg
Zone:		25°-35°N 65°-85°W				25°-35°N 85°-105°W				25°-35°N 105°-125°W		
Cloud winds compared	21	5	17	14	26	6	17	16	10	1	0	4
Mean absolute u_{diff} ($m \cdot s^{-1}$)	4.7	2.3	3.3	3.9	4.0	5.9	7.3	5.4	8.9	7.0		8.7
Mean absolute v_{diff} ($m \cdot s^{-1}$)	3.9	1.6	2.4	3.0	2.9	1.7	4.8	3.4	12.1	6.0		11.5
Zone:		35°-45°N 65°-85°W				35°-45°N 85°-105°W				35°-45°N 105°-125°W		
Cloud winds compared	68	6	28	34	16	14	19	16	4	2	0	2
Mean absolute u_{diff} ($m \cdot s^{-1}$)	3.4	3.7	3.5	3.5	3.7	4.9	3.7	4.0	4.8	1.2		3.6
Mean absolute v_{diff} ($m \cdot s^{-1}$)	3.3	4.1	6.7	4.3	5.9	4.0	10.1	7.0	6.8	4.5		6.0
Zone:		45°-55°N 65°-85°W				45°-55°N 85°-105°W				45°-55°N 105°-125°W		
Cloud winds compared	22	9	15	15	31	1	2	11	1	0	0	0
Mean absolute u_{diff} ($m \cdot s^{-1}$)	6.5	3.2	4.0	5.0	3.8	11.1	4.7	4.1	3.2			
Mean absolute v_{diff} ($m \cdot s^{-1}$)	4.1	6.1	4.4	4.6	3.7	5.5	5.0	3.8	1.3			

TABLE 8. RMS VECTOR ERROR OF UPPER AIR METEOROLOGICAL DATA USING AN AN/GMD-1A RAWIN SET (AFTER USAF, 1963)

	RMS Vector Error ($m \cdot s^{-1}$)		
	Magnitude of mean wind vector from surface to level in question		
Vertical Layer	Less than 15 $m \cdot s^{-1}$	15 - 30 $m \cdot s^{-1}$	30 - 45 $m \cdot s^{-1}$
0 - 6.6 km	1.5	3.5	7.5
6.6-13.1 km	2.0	7.0	15.0
13.1-19.7 km	3.0	10.5	22.5

TABLE 9. AVERAGE MAGNITUDE OF THE VECTORIAL DIFFERENCE IN THE WINDS MEASURED BY TWO RADIOSONDES LAUNCHED NEAR SIMULTANEOUSLY AT SELECTED DISTANCES FROM EACH OTHER (AFTER ARNOLD, 1956)

Distance between sites (km)	0.5	5	110	180	480	600	720	900
Average magnitude of differences ($m \cdot s^{-1}$)	0.6	0.9	3.4	4.3	7.8	8.0	8.9	10.1

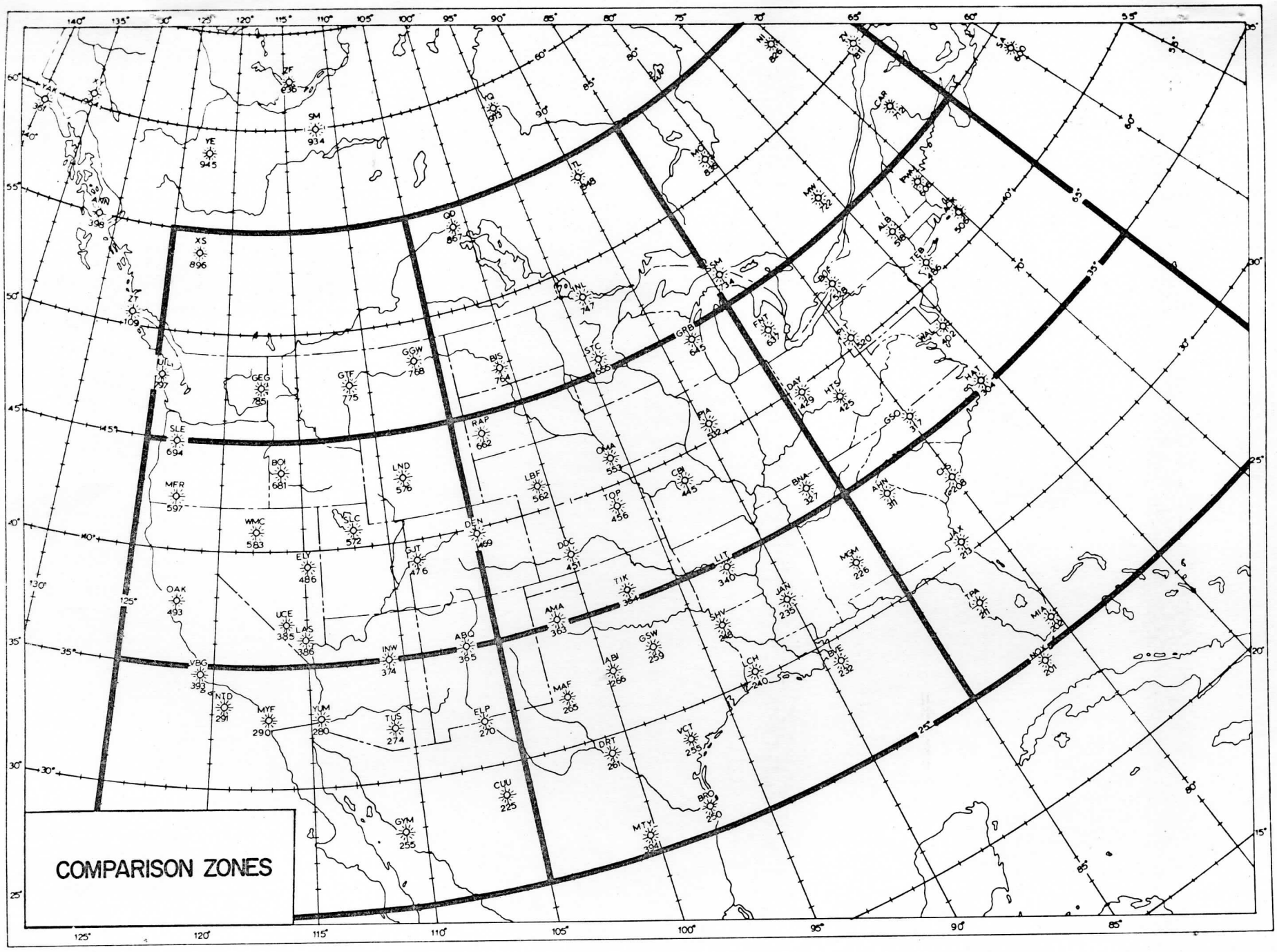

Figure 1. Location of the latitude/longitude bounded comparison zones.

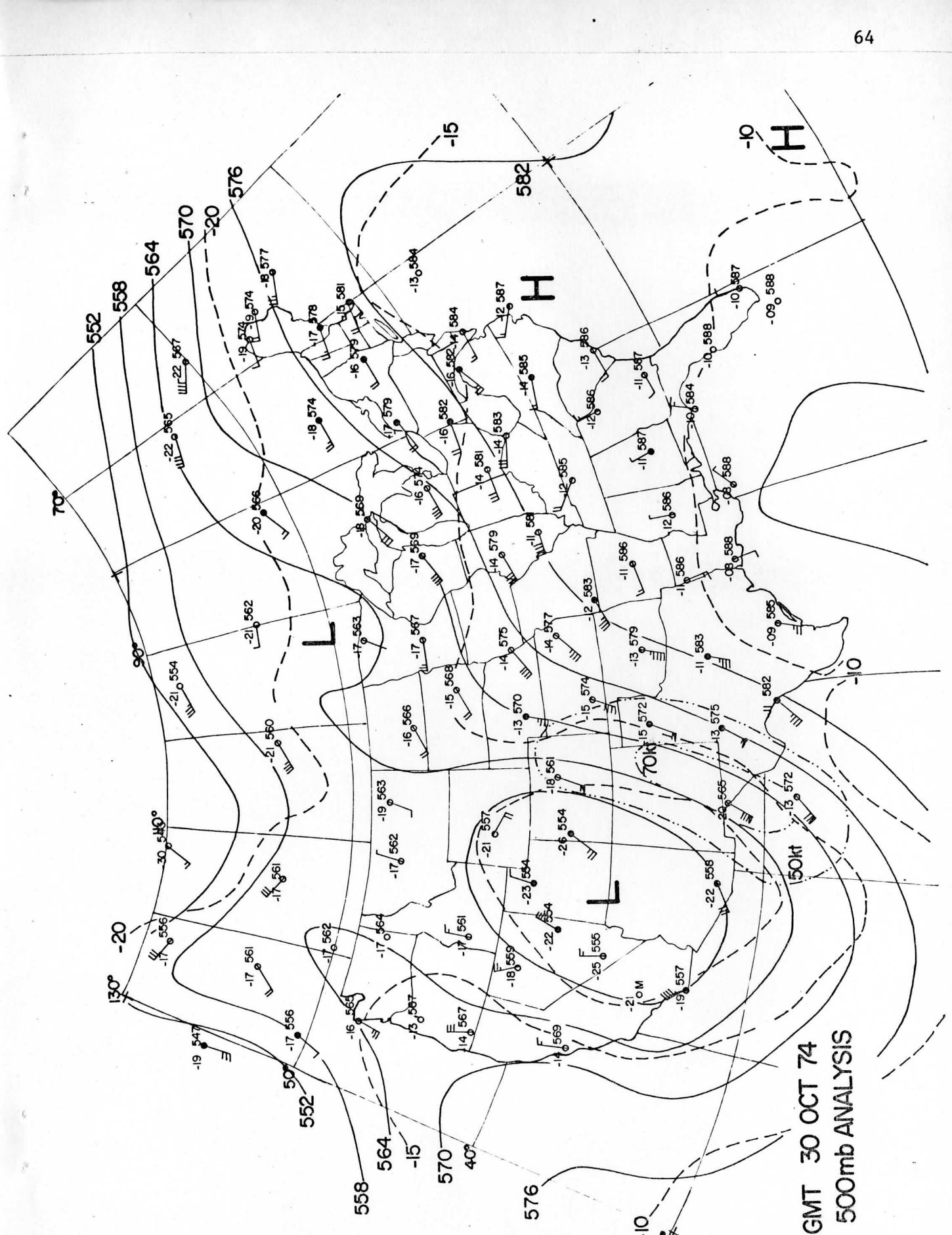

Figure 2. Representative upper air chart for 1200 GMT 30 October 1974 illustrating wind patterns over North America.

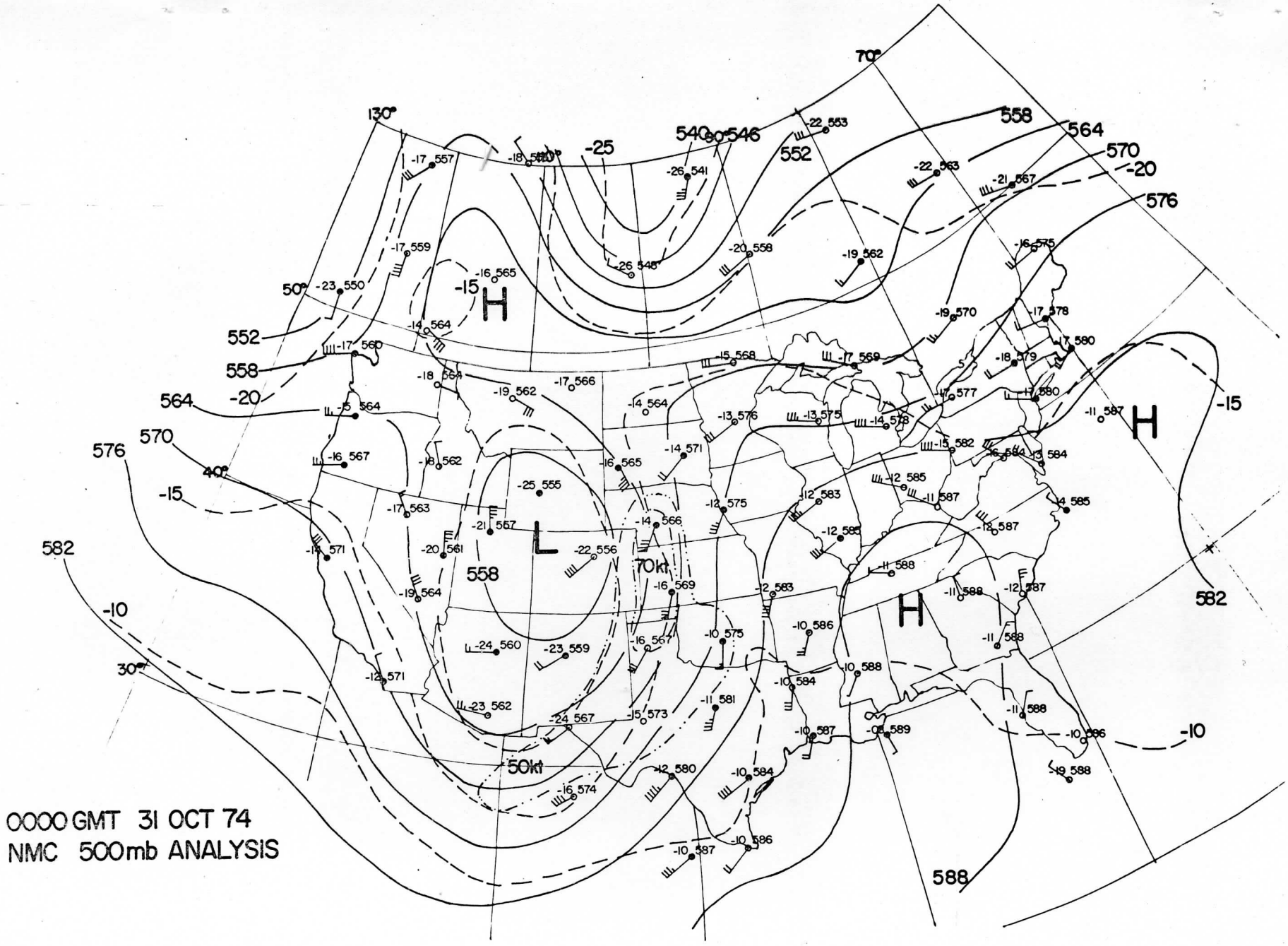

Figure 3. Representative upper air chart for 0000 GMT 31 October 1974 illustrating wind patterns over North America.

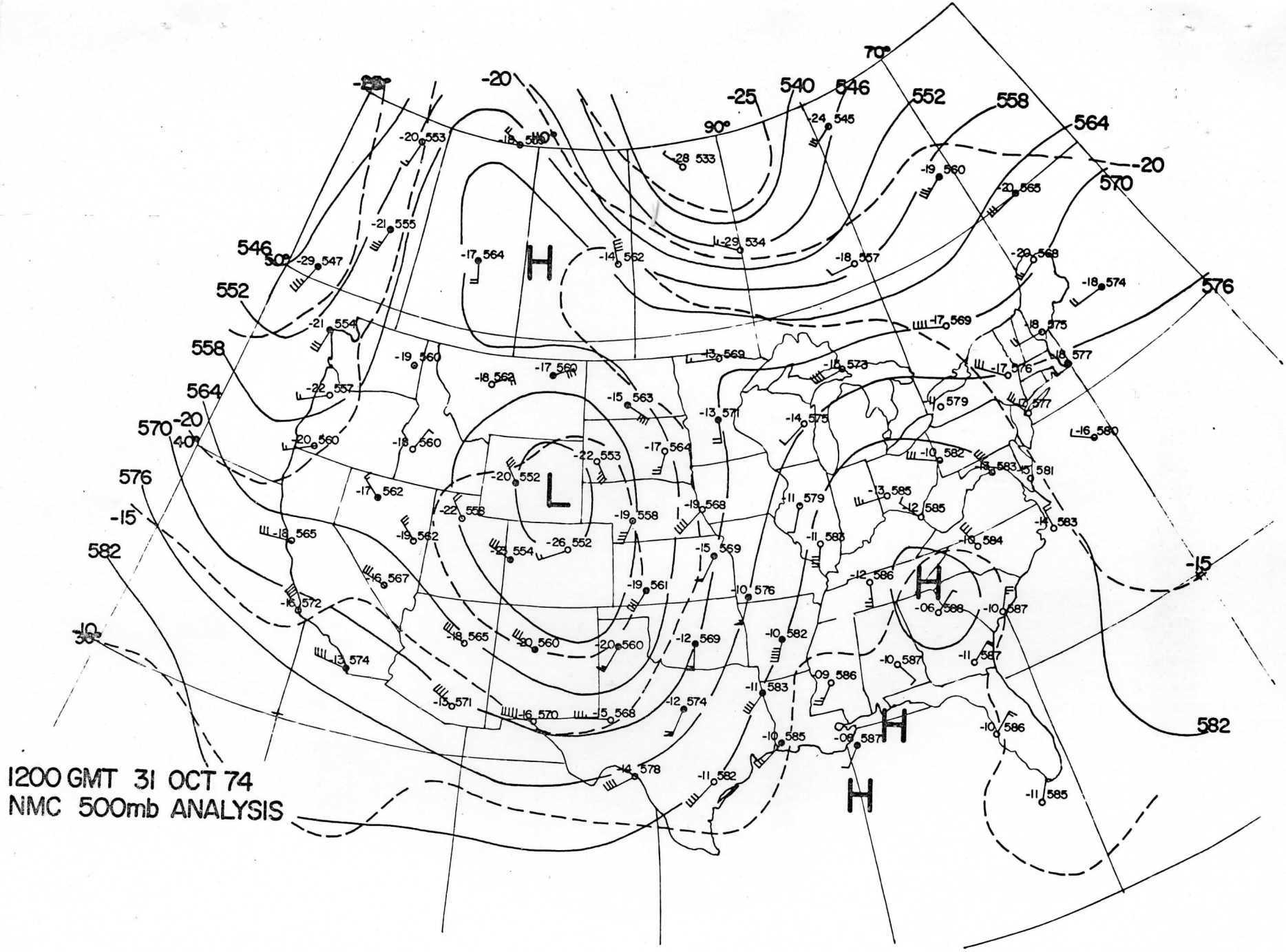

Figure 4. Representative upper air chart for 1200 GMT 31 October 1974 illustrating wind patterns over North America.

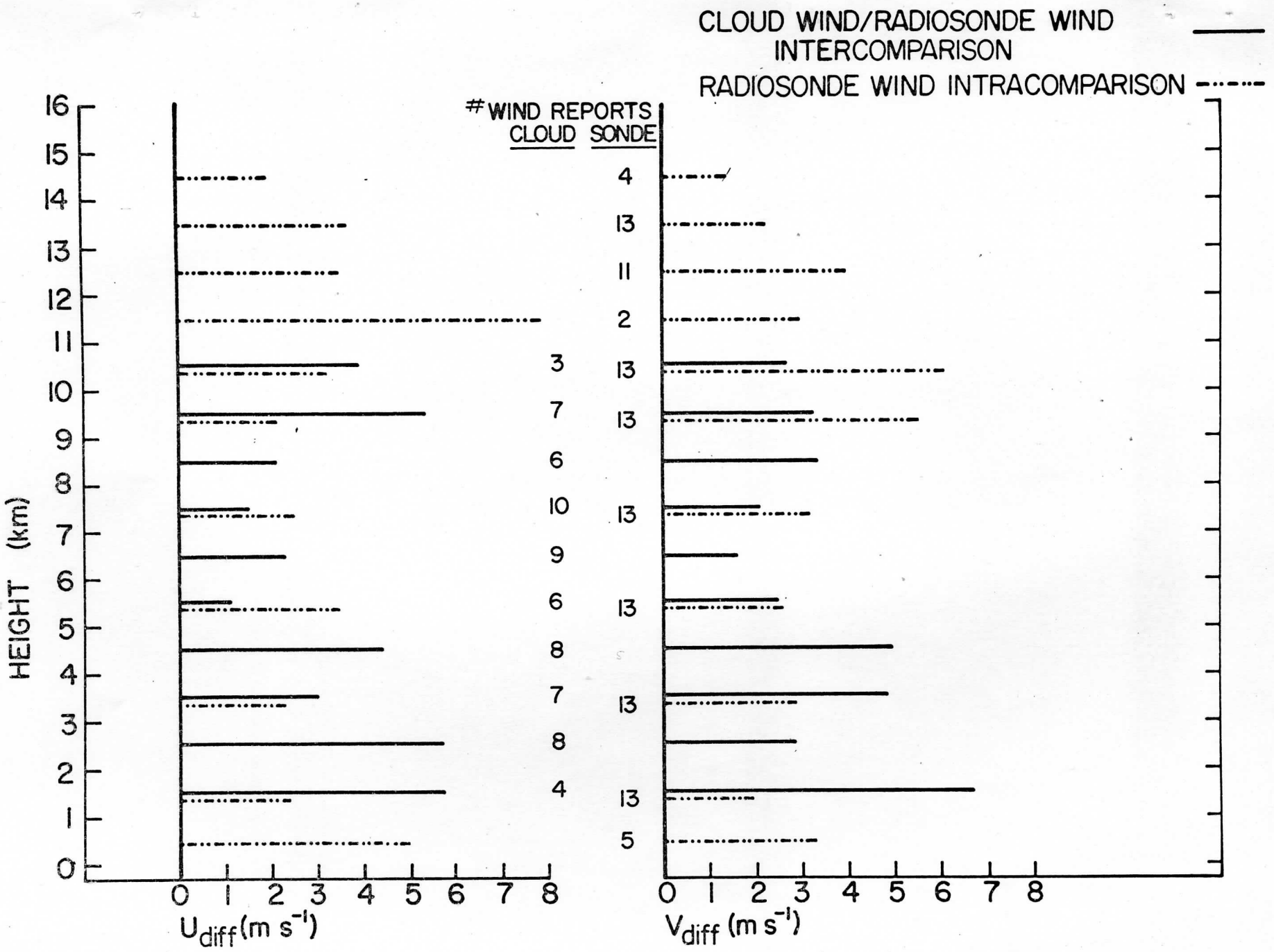

Figure 5. A comparison of the variation with height between the mean absolute differences found during the radiosonde intracomparison with those found during the cloud wind/radiosonde wind intercomparison at 1200 GMT 30 October for the 35° -45° N, 65°-85°W latitude/longitude bounded zone.

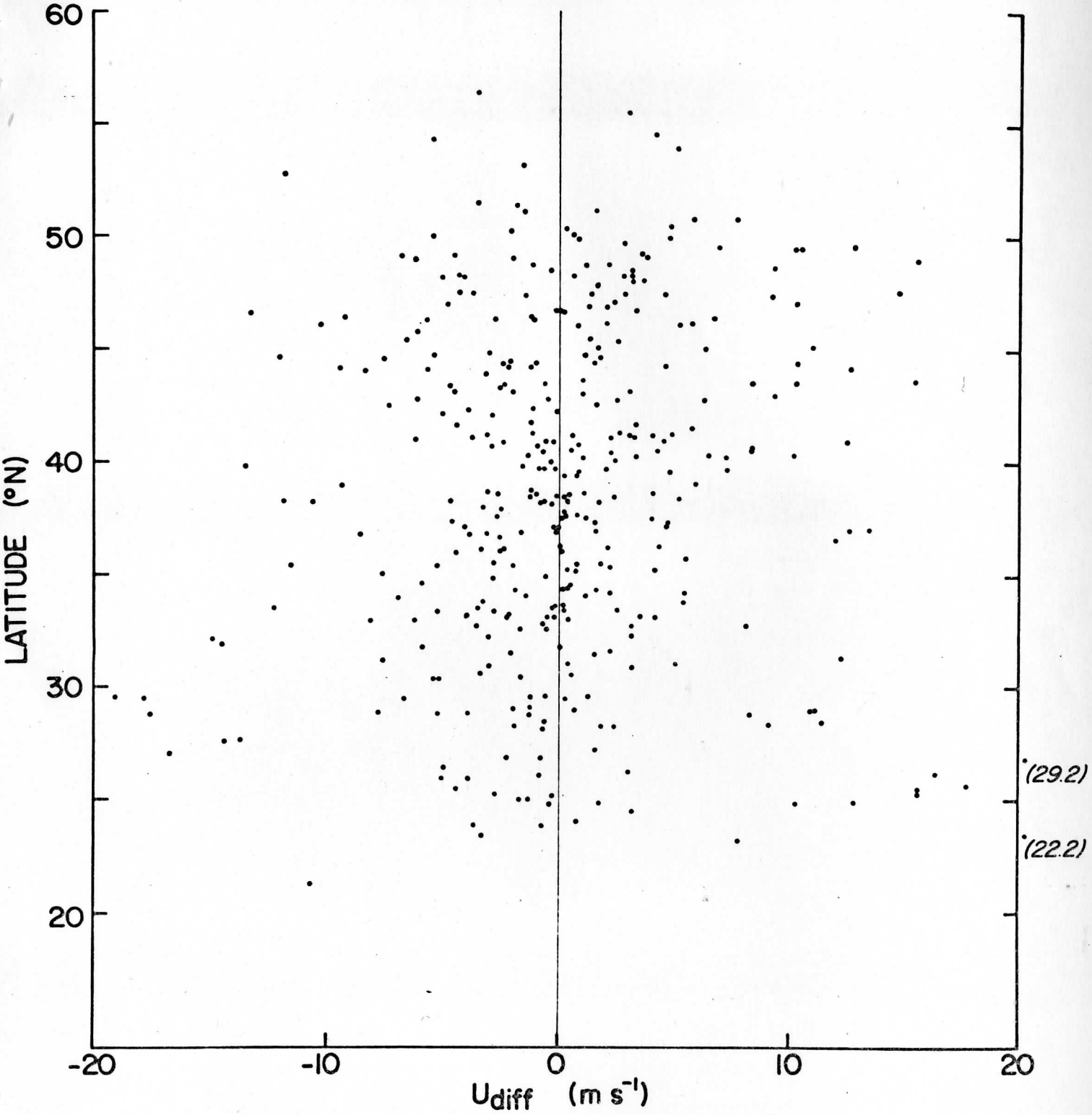

Figure 6a. Distribution of u_{diff} with respect to the latitude of the cloud wind of differences between cloud winds and radiosonde winds for the 365 averaged cloud wind pairs derived over the North American radiosonde network from SMS-1 infrared image sequences at 1200 GMT 30 October 1974 and 0000 GMT and 1200 GMT 31 October 1974.

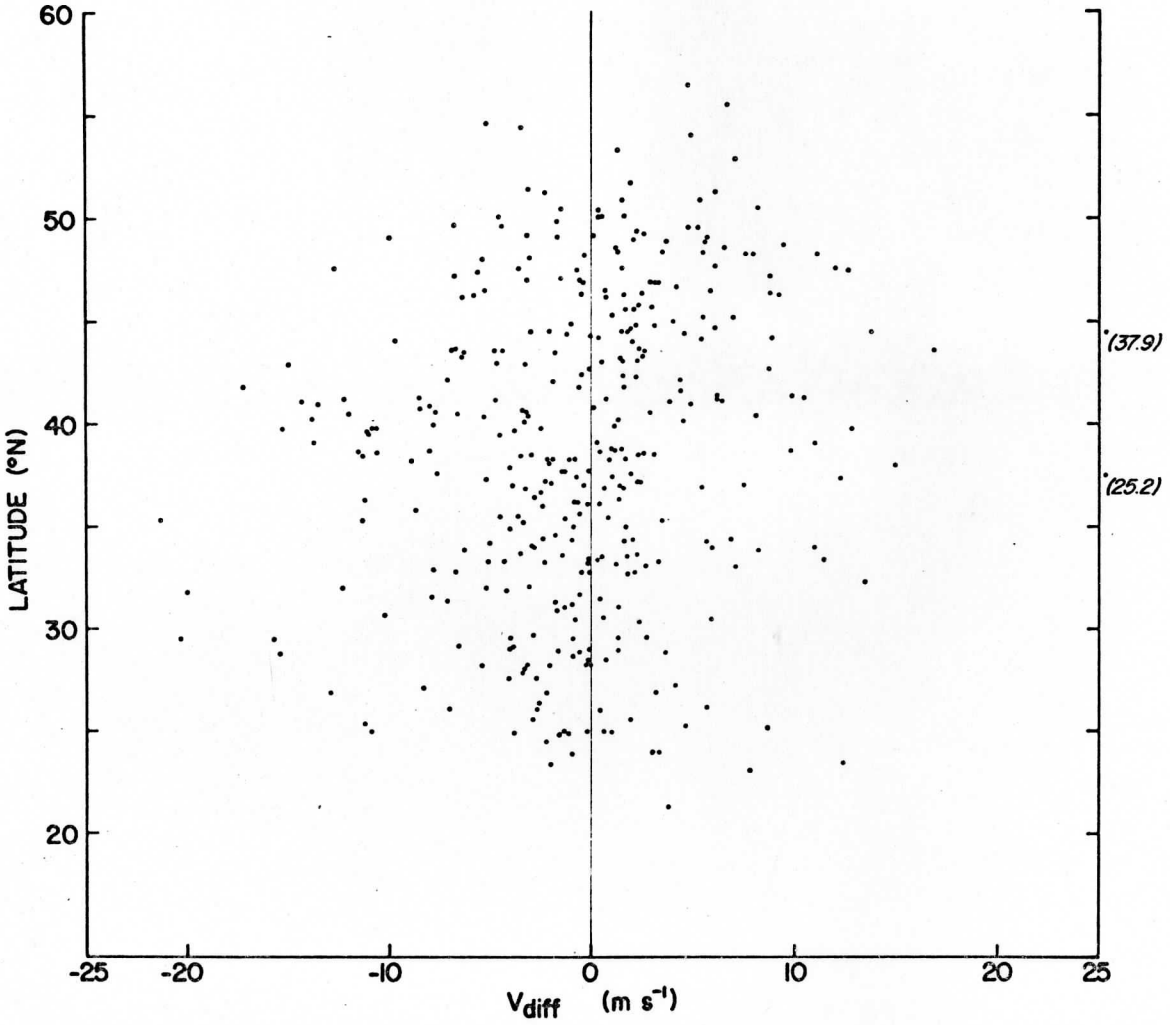

Figure 6b. Distribution of v_{diff} for details given in Figure 6a.

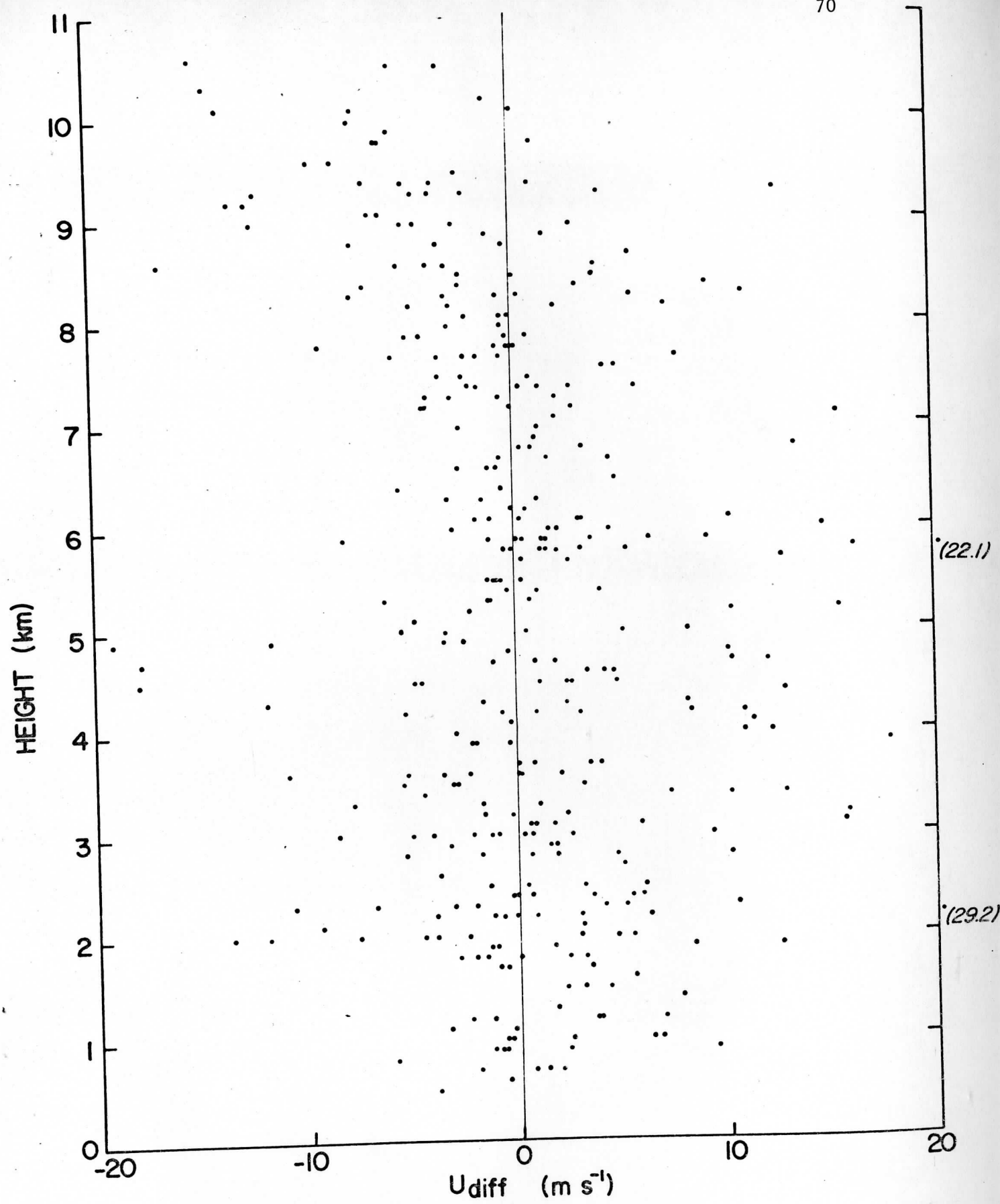

Figure 7a. Distribution of u_{diff} with respect to the height of the cloud wind of differences between cloud winds and radiosonde winds for the 365 averaged cloud wind pairs derived over the North American radiosonde network from SMS-I infrared image sequences at 1200 GMT 30 October 1974 and 0000 GMT and 1200 GMT 31 October 1974.

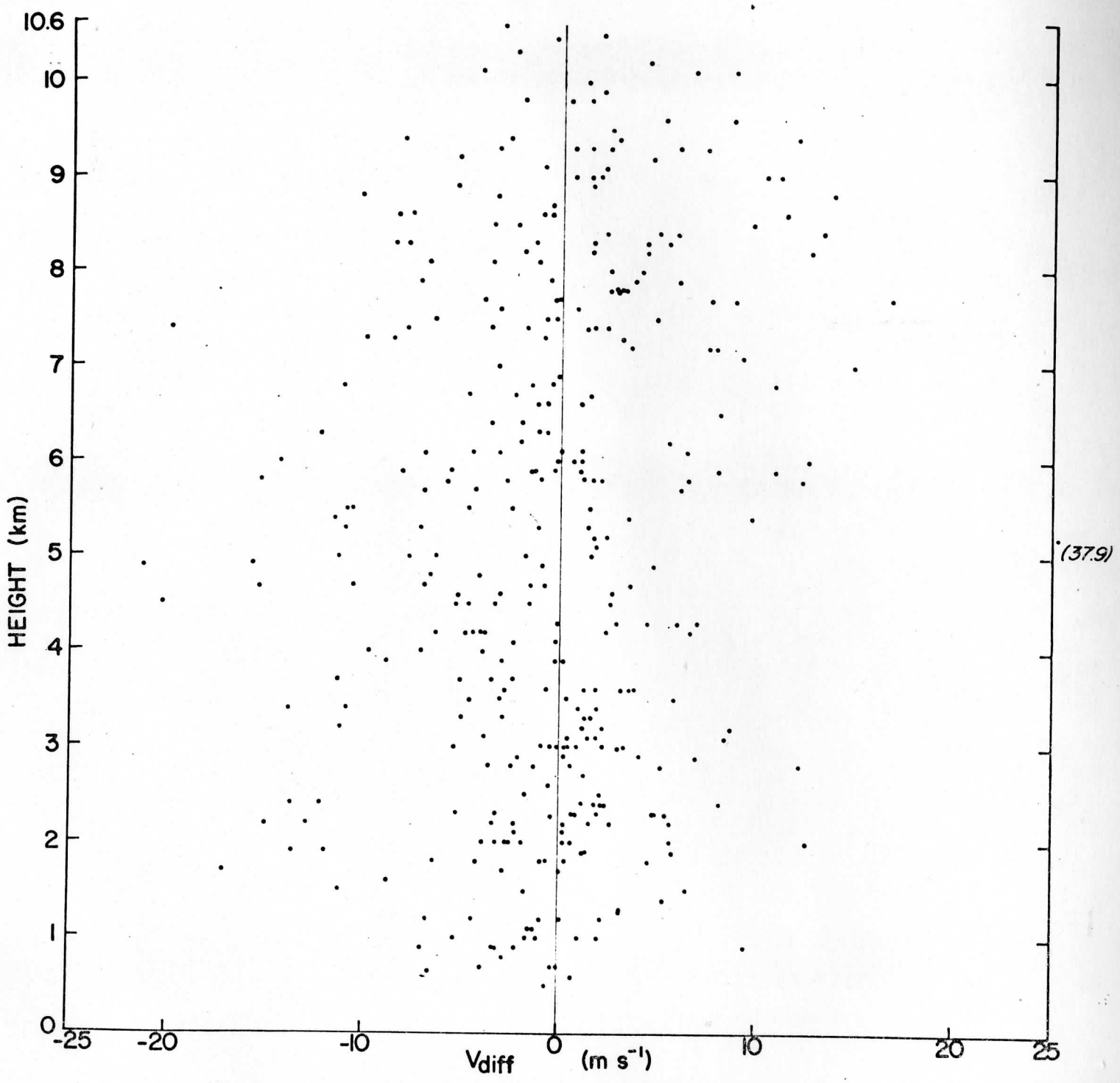

Figure 7b. Distribution of v_{diff} for details given in Figure 7a.

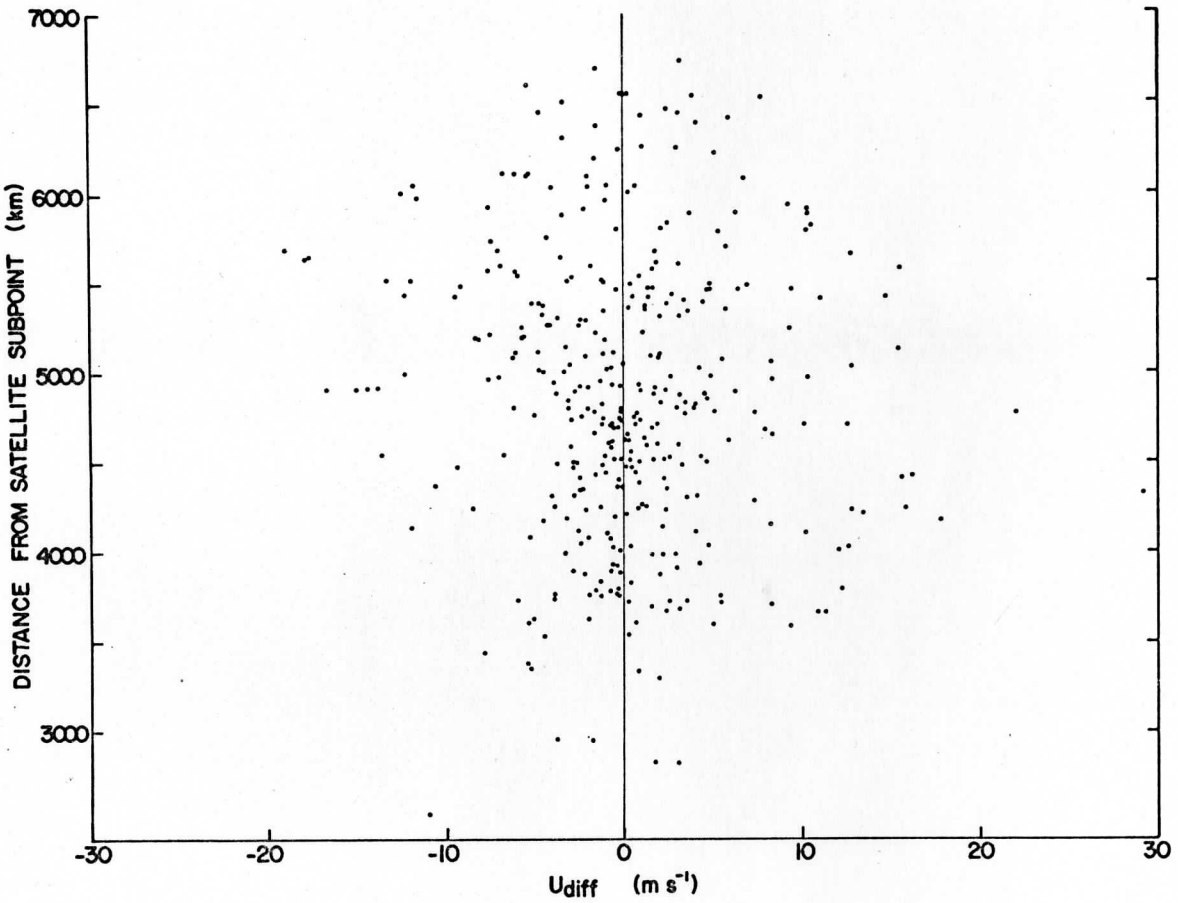

Figure 8a. Distribution of u_{diff} with respect to the distance of the cloud wind from the satellite subpoint of differences between cloud winds and radiosonde winds for the 365 averaged cloud wind pairs derived over the North American radiosonde network from SMS-I infrared image sequences at 1200 GMT 30 October 1974 and 0000 Gmt and 1200 GMT 31 October 1974.

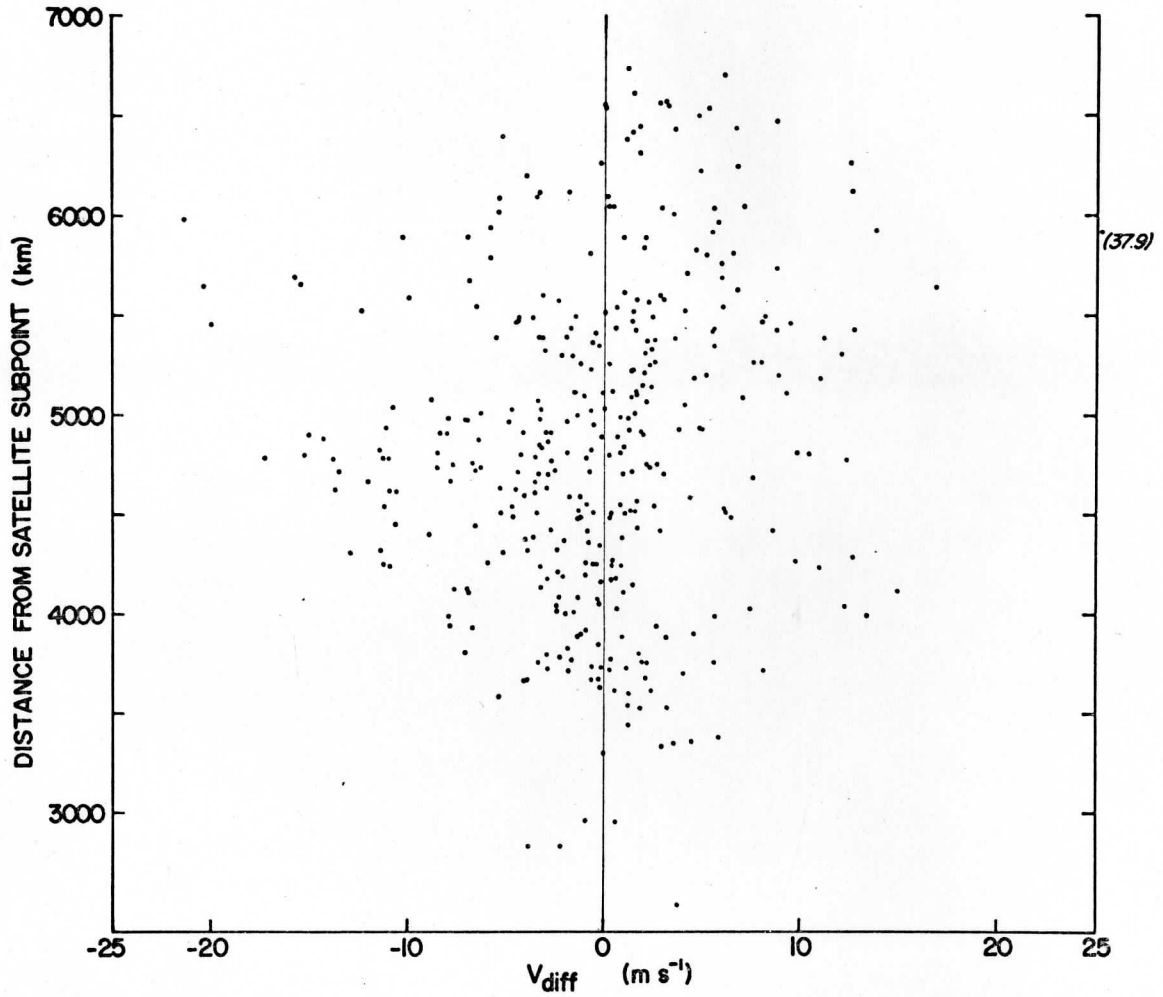

Figure 8b. Distribution of v_{diff} for details given in Figure 8a.

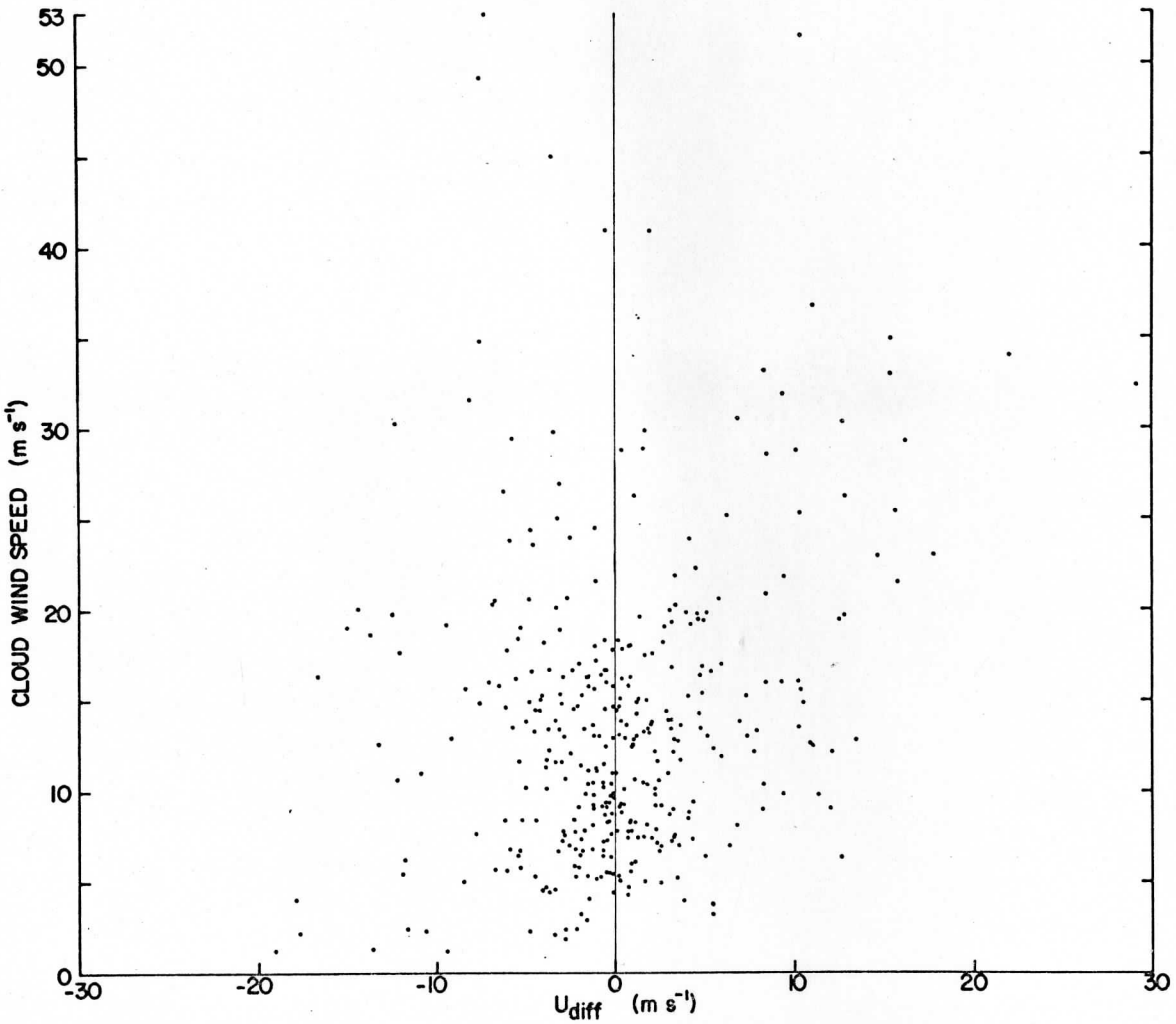

Figure 9a. Distribution of u_{diff} with respect to cloud wind speed of differences between cloud winds and radiosonde winds for the 365 averaged cloud wind pairs derived over the North American radiosonde network from SMS-I infrared image sequences at 1200 GMT 30 October 1974 and 0000 GMT and 1200 GMT 31 October 1974.

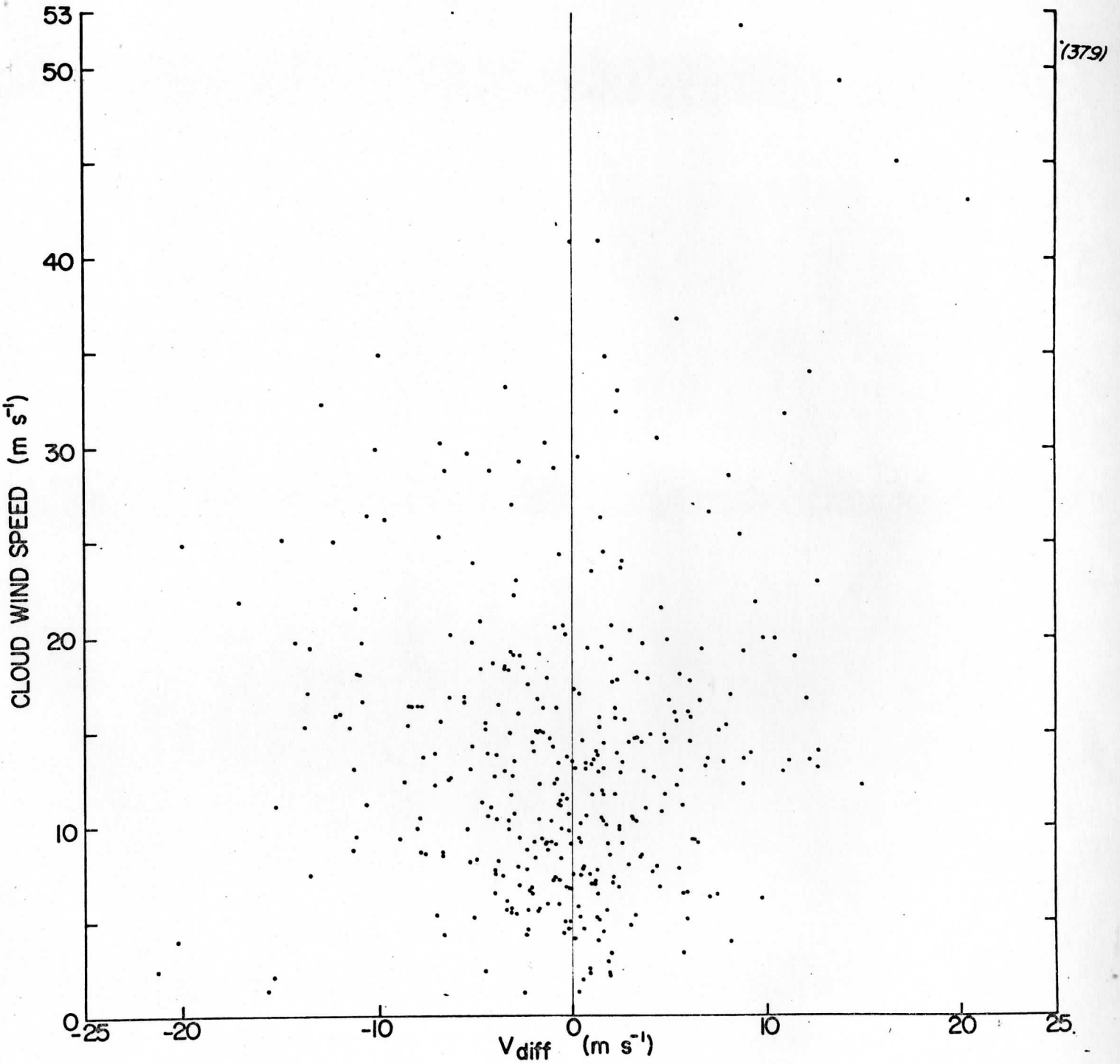

Figure 9b. Distribution of v_{diff} for details given in Figure 9a.

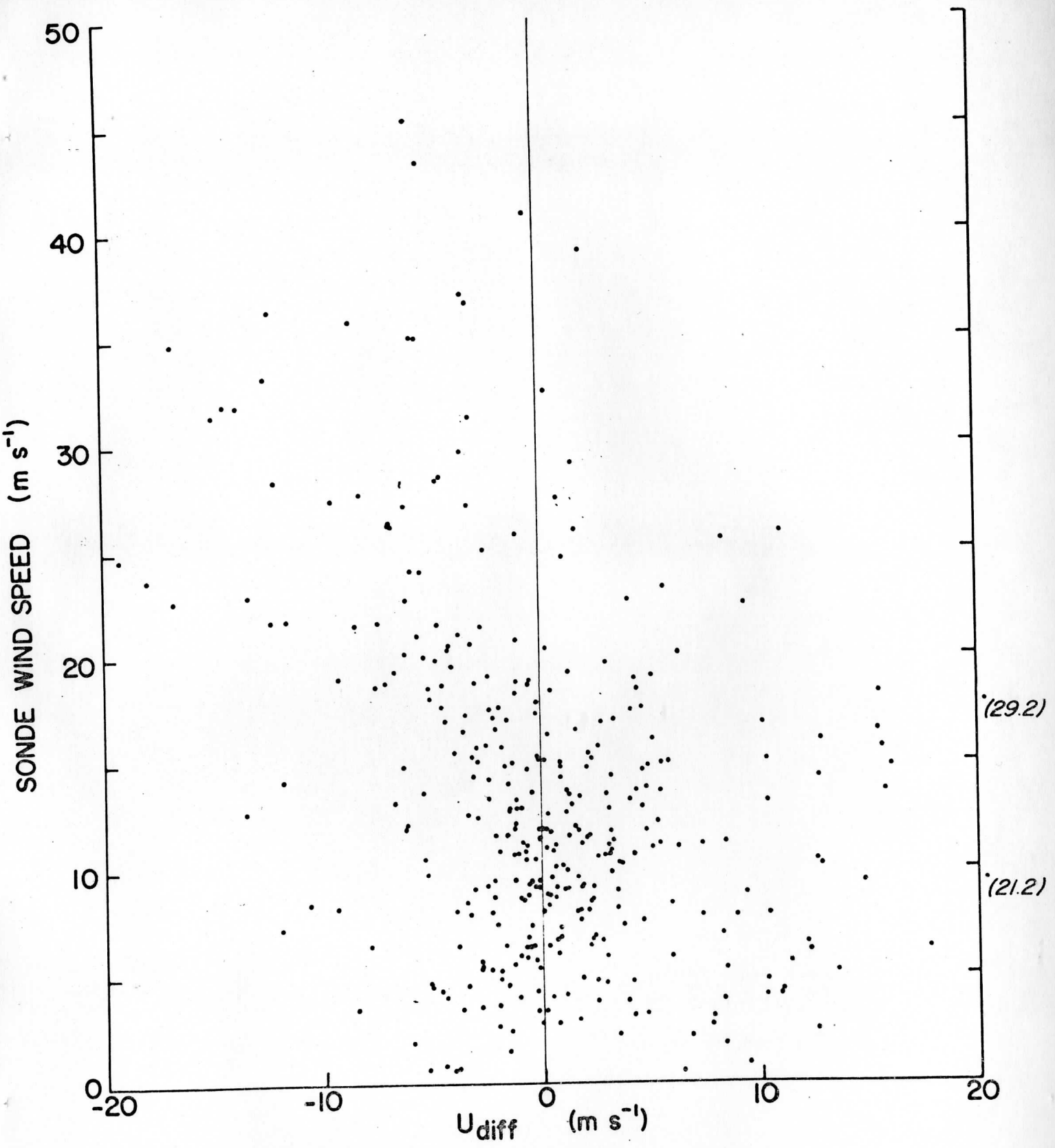

Figure 10a. Distribution of u_{diff} with respect to radiosonde wind speed of differences between cloud winds and radiosonde winds for the 365 averaged cloud wind pairs derived over the North American radiosonde network from SMS-I infrared image sequences at 1200 GMT 30 October 1974 and 0000 GMT and 1200 GMT 31 October 1974.

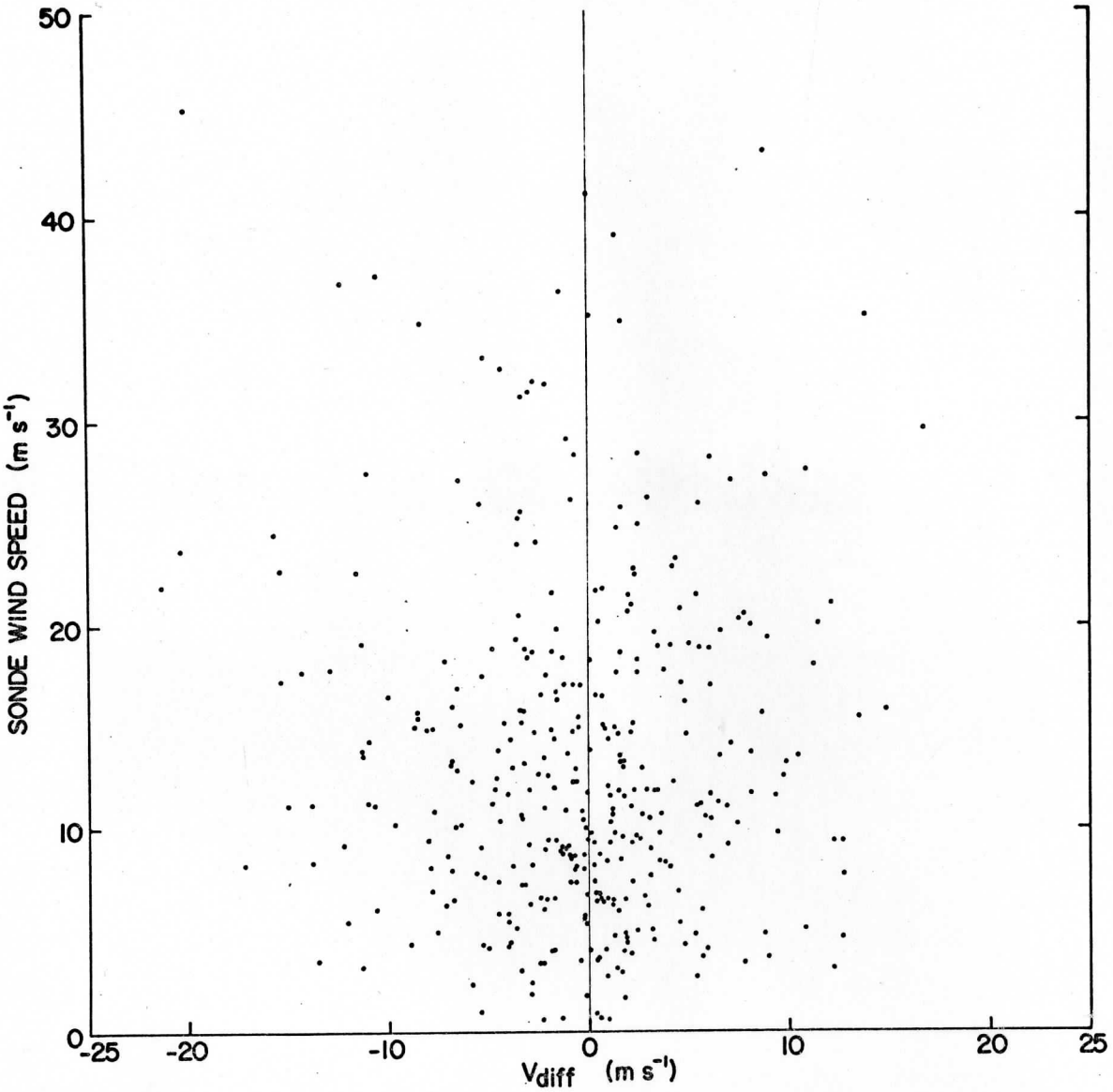

Figure 10b. Distribution of v_{diff} for details given in Figure 10a.

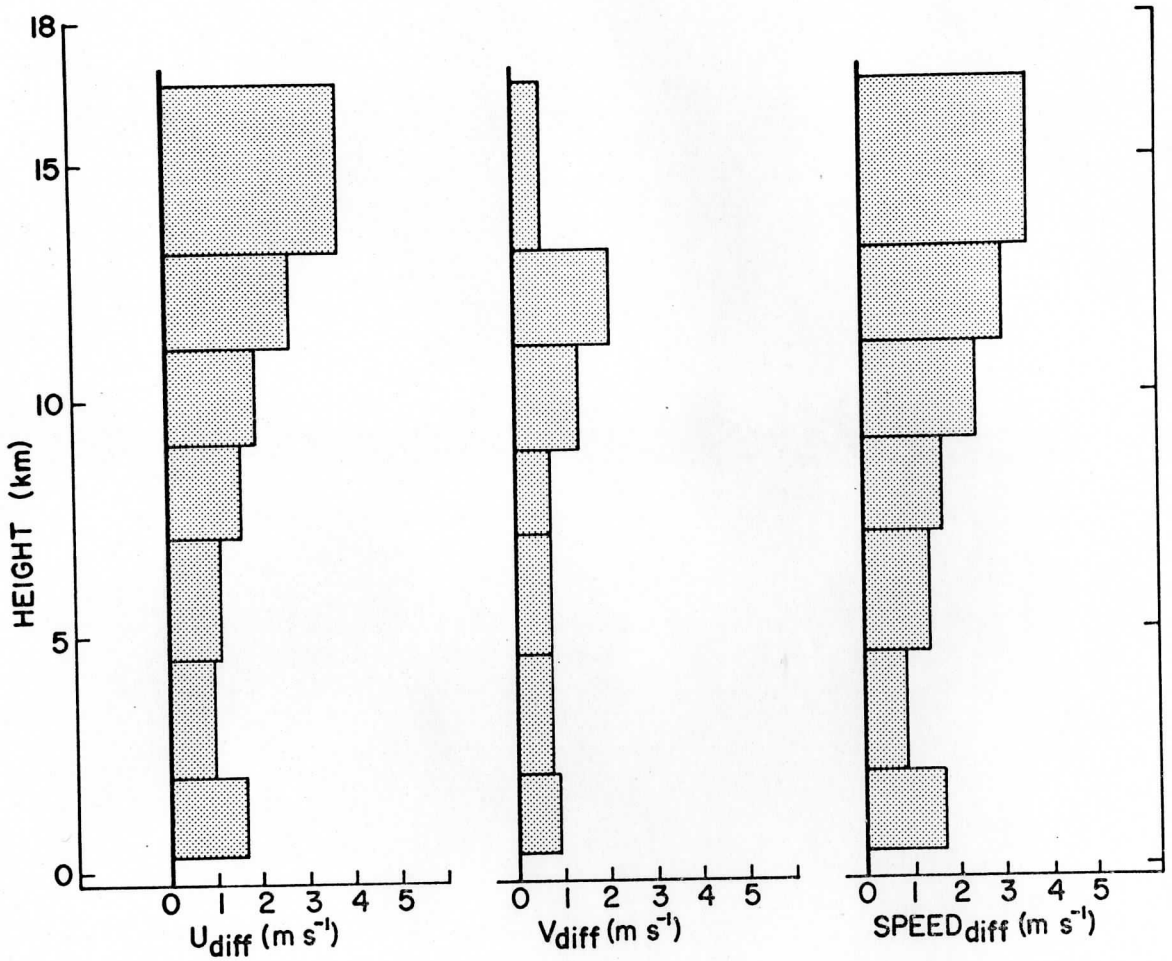

Figure 11. Differences in radiosonde winds produced from one radiosonde run by two different computational techniques: that used by the National Weather Service and that used by the Atmospheric Variability Experiment (absolute differences averaged over three cases.)

STABILITY OF THE LOWER ATMOSPHERE OF VENUS: A DRY ADIABATIC DIAGRAM BASED ON VAN DER WAAL'S EQUATION OF STATE*

Sanjay Limaye

ABSTRACT

The in situ measurements made by the Soviet atmospheric entry probes in recent years such as Venera 4, 6, 7, and 8 indicate that the surface pressure of the planet Venus is in excess of 90 atmospheres (atm) and the temperature is about 750°K. According to Staley (1970) the dry adiabatic lapse rate of temperature cannot be defined simply as the ratio of acceleration due to gravity and the specific heat of the atmosphere at constant pressure, since the ideal gas law on which the definition is based does not hold on Venus. At such high values of atmospheric pressure and temperature the specific heat of carbon dioxide, the predominant constituent of the Venus atmosphere, is a function of both pressure and temperature. Hence the magnitude of dry adiabatic lapse which determines the stability of the atmosphere excluding any phase changes, is no longer constant and varies with pressure and temperature.

A dry adiabatic diagram is constructed based on Van der Waal's equation of state in order to examine the stability of the lower atmosphere of Venus. Venera 8 observations of vertical profiles of temperature and horizontal wind are used to compute Richardson's number.

The computed values of Richardson's number are negative (as small as -11) below about 30 atm pressure and are positive (as large as 32) above 6.5 atm (approximately) pressure level. Between these two levels the Richardson number is close to zero. It is important to bear in mind here that these numbers are based on the particular equation of state employed to calculate the dry adiabatic lapse rate of temperature. But they do provide a useful idea of what the real gas situation might be.

---

*This research was done during 1974, with the first draft completed in August 1974. A follow-up report can be found in Report on NASA grant # NGR-50-002-189.

1. INTRODUCTION

Recently Venera 8, the Russian automatic inter-planetary probe, has measured the surface pressure and temperature on Venus to be about 93 atm and 741 $\pm$ 7°K respectively (Marov et al., 1973). Previous observations indicate that the atmosphere on Venus consists mostly of carbon dioxide (about 97%) and a small amount of nitrogen (2-3%). The high surface pressure and temperature values imply that the ideal gas equation is not applicable. To further complicate matters the specific heat at constant pressure of pure carbon dioxide varies considerably between the range of pressures and temperatures found in the atmosphere of Venus, (see Fig. 1).

It has been suggested previously (Marov, 1972) that since the entropy of carbon dioxide at pressures and temperatures encountered in the atmosphere of Venus does not vary appreciably, the atmosphere is isentropic or close to a state of adiabatic stratification. Lacking any other supportive data it is worthwhile to construct a dry adiabatic diagram to investigate the stability of the lower atmosphere of Venus for a given atmospheric composition.

For atmospheric (vertical) stability considerations the adiabatic lapse rate of temperature must be known accurately. As Staley (1970) has pointed out, the ideal gas definition of the adiabatic lapse rate $\gamma_{ad} = g/C_p$ is not suitable because of the high pressures and temperatures in the lower atmosphere of Venus. The dry adiabatic lapse rate is a function of both pressure and temperature since for a real gas the internal energy is not a function of temperature only. According to Staley (1970) the real gas dry adiabatic lapse rate can be expressed as:

$$\gamma_{ad} = \frac{-dT}{dz} = -\frac{T(\partial p/\partial T)}{\alpha(\partial p/\partial \alpha)_T}\left(\frac{g}{C_p}\right) = \frac{1}{Z}\left[\frac{\partial}{\partial T}(TZ)\right]_p \left(\frac{g}{C_p}\right) \qquad (1)$$

where $Z = Z(p,T) = pv/RT$ is the compressibility.

Calculation of the dry adiabatic lapse rates thus requires knowledge not only of the specific heat at constant pressure as a function of both pressure and temperature but also the compressibility factor of the gas.

An alternate solution seems possible, however. At moderate pressures the behavior of a real gas can be described through Van der Waal's equation of state, albeit only approximately compared to the virial equation of state. According to Van der Waal's equation of state:

$$(p + a/v^2)(v - b) = RT \qquad (2)$$

where the Van der Waal coefficients a and b are related through the relationship (Zemansky, 1957):

$$8a = \frac{27b}{R_c T_c} \quad .$$

Laboratory measurements of pressure, temperature, and density of carbon dioxide (Hilsenrath et al., 1960) indicate that between 200-1000°K the curves for the product $(p + a/v^2)(v - b)$ for values of pressure between 0.01 and 100 atm diverge only slightly (Fig. 2 top). For small pressure changes, the Van der Waal equation might perhaps be a good approximation at the relatively high values of temperature found in the atmosphere of Venus. When the pressure correction term is neglected one obtains a simpler equation of state often called the Clausius equation of state. In this case the agreement with experimental values is poorer (Fig. 2 bottom) but the correction required is almost the same over the range of temperatures and pressures found in the atmosphere of Venus.

For a Van der Waal gas in an isentropic process the temperature change dT accompanying a pressure change dp can be shown to be:

$$\frac{dT}{dp} = \frac{RTv^3(v - b)}{C_p\{RTv^3 - 2a(v - b)^2\}} \quad \text{(Zemansky, 1957).} \qquad (3)$$

Furthermore, provided the pressure correction term, which is significant at very high pressures and relatively lower temperatures, is ignored in comparison with the volume correction term (i.e. the Clausius equation of state, $p(v - b) = RT$) then Eq. (3) reduces to

$$\frac{dT}{dp} = \frac{RT}{C_p p} \qquad (4)$$

using the Clausius equation of state.

Equation (4) offers a simpler way to compute the dry adiabatic lapse rate compared to Eq. (1). The computed values are likely to be less accurate than the real case, however the aim here is to see if the stability of the lower atmosphere of Venus warrants a closer scrutiny.

2. THE DRY ADIABATIC DIAGRAM

Hilsenrath et al. (1960) have tabulated the value of C_p/R as a function of both pressure and temperature. Using these tabulated values an adiabatic diagram was prepared by linearly interpolating the value of C_p/R at the new values of T and p determined by the

initial values of p, T, and a predetermined pressure decrement value. The isentropes were constructed between 100 atm and 0.01 atm. The pressure decrement was 1 atm between 100 atm and 1 atm, 0.1 further on to 0.1 atm, and 0.01 up to 0.01 atm. Five such isentropes are shown in Fig. 3. The temperature profile for the atmosphere of Venus as measured by Venera 8 (Marov et al., 1973) is also shown in this figure.

The adiabatic lapse rate as computed is in °K per atmosphere and can be easily expressed in °K/meter through the use of the hydrostatic equation:

$$dp = -g\rho dz \tag{5}$$

From the simplified equation of state $p(v - b) = RT$, the density is given by:

$$\frac{1}{\rho} = \frac{RT}{p} + b \tag{6}$$

so that:

$$\frac{dT}{dz} = -g\rho \frac{dT}{dp} = -\frac{dT}{dp} \cdot \frac{gp}{(RT + bp)} \tag{7}$$

Values of the dry adiabatic lapse rate for certain selected pressures and temperatures are given in Table 1. For each value of pressure the numbers are given at three values of temperature. For pressures less than 100 atm the selected temperatures correspond to those reached under adiabatic expansion for the three initial temperatures 800°K, 750°K, and 700°K respectively. For comparison the values of the dry adiabatic lapse rate obtained by Staley (1970) are also given. It is seen that between 100 atm and 1 atm pressure the dry adiabatic lapse rate of temperature varies by as much as 20% or more. One consequence of this is that the differences in potential temperature are different from isobaric temperature differences. Thus a difference of 28°K in absolute temperature at 1 atm amounts to a difference of 50°K in the potential temperature were it defined with 100 atm as the reference value.

3. EXAMINATION OF THE VENERA 8 TEMPERATURE PROFILE

The Venera 8 temperature profile as reported by Marov et al. (1973) has been plotted in Fig. 3 (this is a skew T-log p plot) as a heavy solid line, up to 0.5 atm. From then on up to 0.01 atmospheres the Mariner 10 temperature profile as deduced from radio occultation measurements (from the signal received through the DSN-12 antenna; Howard et al., 1974) is also shown.

The error reported by Marov et al. in the surface temperature is $\pm$ 7°K, or about 1%. Allowing for this error, the most striking feature of this profile is the super-adiabatic lapse rate up to a pressure of about 15 atm and an altitude of approximately 25 km, as measured by Venera 8. From then on up about 7 atm ($\sim$31 km) the lapse rate is more nearly adiabatic. Above 32 km the lapse rate is strongly sub-adiabatic.

Using Venera 8 measurements for the horizontal wind as a function of altitude, the Richardson number ($= g/\theta\ [(\partial\theta/\partial z)/(\partial u/\partial z)^2]$) has been computed. The potential temperature was defined with reference to a pressure of 100 atm and was read off from the skew T-log p plot. The computed values of Ri are given in Table 2 along with the static stability ($\partial\theta/\partial z$) and vertical shear of the wind. A very large range of values is seen for Ri from -35.0 to about +32.4. The static stability and the Richardson's number are both shown as a function of pressure in Fig. 4. Ri is seen to be approximately zero from about 20 atm to 6 atm.

4. DISCUSSION

Based on the dry adiabatic lapse rate, computed through the simplified Van der Waal or Clausius equation of state for a 100% carbon dioxide atmosphere, the lower atmosphere of Venus does not seem to be adiabatic according to the Venera 8 temperature profile; rather the lower atmosphere exhibits a slightly super-adiabatic lapse rate. This is not meant to imply that in reality such a situation exists on the planet but suggests that there are some problems--either with the assumptions made in the computation of the lapse rate, or with the observations, or both.

The pressure correction term was ignored in the computations, however its retention does not change the computed lapse rate by an amount sufficient to make the Venera 8 temperature profile neutral. Thus use of the Clausius equation of state is not the main problem.

The next most logical source of error is that the atmosphere has been taken to be 100% carbon dioxide. It is known that there is a small amount of nitrogen (3-10%) present in the atmosphere. Preliminary calculations show that assuming the dry adiabatic lapse rate can be computed based on the calculated specific heat of the mixture of two gases, the Venera 8 profile is still unstable for a 10% nitrogen and 90% carbon dioxide atmosphere.

Lastly, one should consider the possibility that the measured profile could have errors larger than 1% of the temperature at a given level.

In conclusion, the use of Clausius equation of state allows a quick estimate of the dry adiabatic lapse rate which is generally a few percent larger in magnitude than the Van der Waalian value (i.e. with the pressure correction term).

The present work has shown the importance of the precise knowledge of the dry adiabatic lapse rates in the atmosphere of Venus, as the lower atmosphere is so close to a state of adiabaticity. The principle sources of uncertainty in the computed lapse rate are:

1. Uncertain atmospheric composition. In the present case a 100% carbon dioxide atmosphere is assumed. Observations indicate that some nitrogen is present ($\lesssim$ 8%, Marov, 1972).

2. Applicability of Van der Waals' or Clausius equation of state.

3. Errors in the tabulated and interpolated values of specific heats of the constituent gas.

In order to firmly ascertain the stability of the lower atmosphere of Venus an effort dealing with these uncertainties is necessary. Work is underway to refine the computations reported here by (1) using the virial equation of state following Staley (1970), (2) accounting for the presence of nitrogen, and (3) using a four-point Lagrangian interpolation scheme for obtaining intermediate point values from the tables of Hilsenrath et al. (1960). The results will be reported at a later date.

ACKNOWLEDGEMENTS

The author would like to thank Dr. Verner Suomi for inspiring the study and for constructive comments. Also, thanks are extended to Dr. Mike Belton and Mr. Robert Krauss for discussions on the study.

REFERENCES

Hilsenrath, J., C. W. Becket, W. S. Benedict, L. Farro, H. J. Hoge, J. F. Masi, R. L. Nuttal, Y. S. Toulobian, and H. W. Woolley, 1960: Tables of Thermodynamic and Transport Properties of Air, Argon, Carbon Dioxide, Carbon Monoxide, Nitrogen, Oxygen, and Steam. Pergamon Press, New York, pp. 191.

Howard, H. T., G. L. Tyler, G. Fjeldbo, A. J. Kliore, G. S. Levy, D. L. Brunn, R. Dickinson, R. E. Edelson, W. L. Martin, R. B. Postal, B. Seidel, T. T. Sesplauleis, D. L. Shirley, C. T. Stelzried, D. N. Sweetnam, Z. I. Zygielbaum, P. B. Esposito, J. D. Anderson, I. I. Shapiro, and R. D. Reasenberg, 1974: Venus: Mass, Gravity Field, Atmosphere, and Ionosphere as Measured by the Mariner 10 Dual Frequency Radio System. Science, (183), 1297-1306.

Marov, M. Y., 1972: A Perspective in the Beginning of Planetary Exploration. Icarus, (16), 415-461.

Marov, M. Y., V. S. Avduevsky, V. V. Kerizanovich, M. K. Rozhdestveusky, N. F. Borodin, and O. L. Ryabov, 1973: Preliminary Results on the Venus Atmosphere from the Venera 8 Descent Module. Icarus, (20), 407-421.

Staley, D. O., 1970: The Adiabatic Lapse Rate in the Venus Atmosphere. J. Atmos. Sci. (27), 219-223.

Zemansky, Mark W., 1957: Heat and Thermodynamics. McGraw Hill Book Co. Inc., New York.

FIGURE LEGENDS

Figure 1: Variation of specific heat of carbon dioxide at constant pressure with temperature for various pressures.

Figure 2: Variation product $(p + a/v^2)(v - b)$ (top) and $p(v - b)$ (bottom) (in atm·cm^3) for carbon dioxide for 0.01 atm and 100 atm pressure with temperature. The curves diverge by a relatively small amount at high temperatures. This is interpreted to mean that use of the Van der Waal's equation of state, and perhaps its simplified form, may not be too unreasonable.

Figure 3: The dry adiabatic diagram constructed with a skew-T axis. The temperature profiles from Venera 8 and Mariner 10 radio occultation measurements are also shown.

Figure 4: Profiles of Richardson number and vertical stability from Venera 8 measurements of temperature and horizontal wind.

TABLE 1

ADIABATIC LAPSE RATES

Based on simplified Van der Waal Equation of State (a = 0)
for 100% carbon dioxide atmosphere

Pressure	Temperature	R/c_p	°K/Atm	°K/km	Staley (1970)
100 Atm	1) 800.0°K	6.387	1.25	-7.59	-7.62
	2) 750°	6.326	1.18	-7.69	-7.85
	3) 700°	6.267	1.12	-7.79	-8.11
75 Atm	1) 765°K	6.331	1.61	-7.58	--
	2) 718°	6.266	1.52	-7.68	--
	3) 669°	6.205	1.43	-7.78	--
50 Atm	1) 718°K	6.160	2.33	-7.69	--
	2) 672°	6.102	2.20	-7.78	--
	3) 626°	6.009	2.08	-7.92	--
25 Atm	1) 641°K	5.920	4.32	-7.85	--
	2) 599°	5.7838	4.14	-8.05	--
	3) 557°	5.691	3.91	-8.19	--
10 Atm	1) 550°K	5.564	9.88	-8.08	-8.45
	2) 513°	5.494	9.33	-8.19	-8.65
	3) 476°	5.358	8.88	-8.88	-8.91
1 Atm	1) 377°K	4.864	7.76	-9.28	-9.55
	2) 349°	4.716	7.40	-9.58	-9.78
	3) 321°	4.659	6.88	-9.71	-10.11
0.5 Atm	1) 329°K	4.606	14.2	-9.32	--
	2) 303°	4.534	13.37	-9.48	--
	3) 277°	4.354	12.74	-9.89	--
0.1 Atm	1) 244°K	4.199	58.0	-10.8	--
	2) 223°	4.097	54.3	-11.1	--
	3) 201°	4.009	50.1	-11.37	--

TABLE 2

Pressure (Atm)	Altitude km	Temperature °K	Potential Temperature °K	$\partial\Theta/\partial z$ °K/meter	$(\partial u/\partial z)$ sec^{-1}	Ri*
80.0	3.6	721.5	748.6	-0.78125	X	X
78.0	4.0	713	743	-14.70	X	X
75.0	4.5	709	~743	0.009	X	X
70.0	5.5	703	744	0.969	X	X
60.0	8.0	684	741.5	-1.1	X	X
55.0	9.1	673	740.5	-0.792	X	X
50.0	10.5	660	740	-0.37	$6.3 \cdot 10^{-4}$	-11.0
45.0	12.0	648	738	-1.34	$2.5 \cdot 10^{-3}$	-2.5
40.0	14.0	635	736.5	-0.911	$5.0 \cdot 10^{-3}$	-0.43
35.0	15.5	617	732.0	-2.45	$3.8 \cdot 10^{-3}$	-2.0
30.0	17.5	600	733.0	+0.53	0	0
25.0	20.0	579	730.0	-1.24	0	0
20.0	22.5	562	720.0	-1.74	$8.33 \cdot 10^{-4}$	-30.3
15.0	27.0	520	720.0	0	$1.39 \cdot 10^{-3}$	0
9.0	32.5	480	718.6	0	$-2.8 \cdot 10^{-4}$	0
7.0	35.0	442	719	0	0	0
6.0	37.5	424	719.5	X	$1.39 \cdot 10^{-4}$	X
5.8	40.0	430	720	X	$1.4 \cdot 10^{-3}$	0.87
4.0	42.5	401	728	1.82	$8.8 \cdot 10^{-3}$	X
3.0	45.0	382	740	3.34	$1.1 \cdot 10^{-3}$	+32.5
2.0	50.0	359	820			

X -- Represents uncertain values due to rapid changes in the velocity profile.

*$Ri = \frac{g}{\theta} \cdot \frac{\partial\theta/\partial z}{(\partial u/\partial z)^2}$

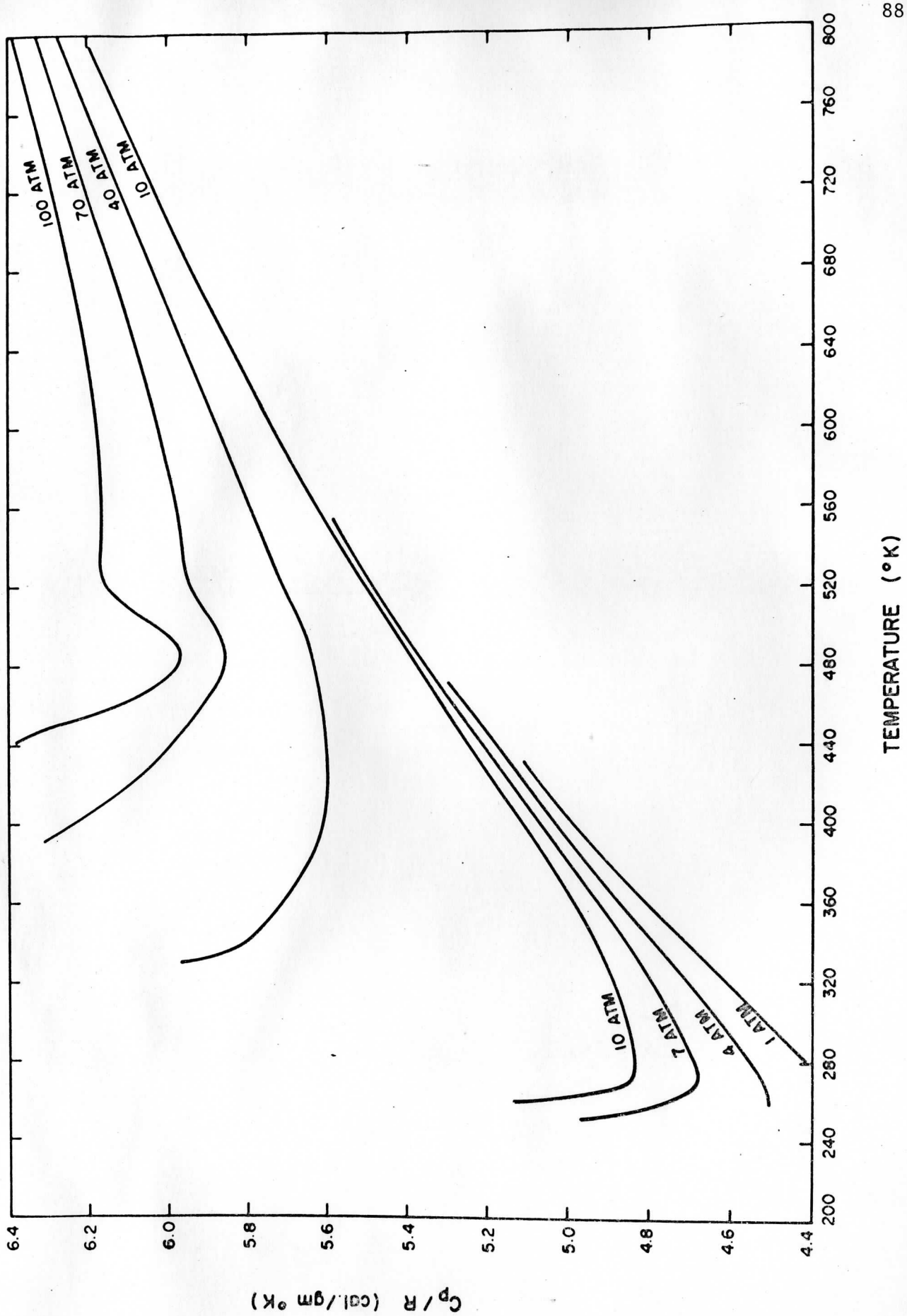
100 ATM
70 ATM
40 ATM
10 ATM
10 ATM
7 ATM
4 ATM
1 ATM
C_p / R (cal./gm °K)
TEMPERATURE (°K)
6.4
6.2
6.0
5.8
5.6
5.4
5.2
5.0
4.8
4.6
4.4
200
240
280
320
360
400
440
480
520
560
600
640
680
720
760
800

Figure 1

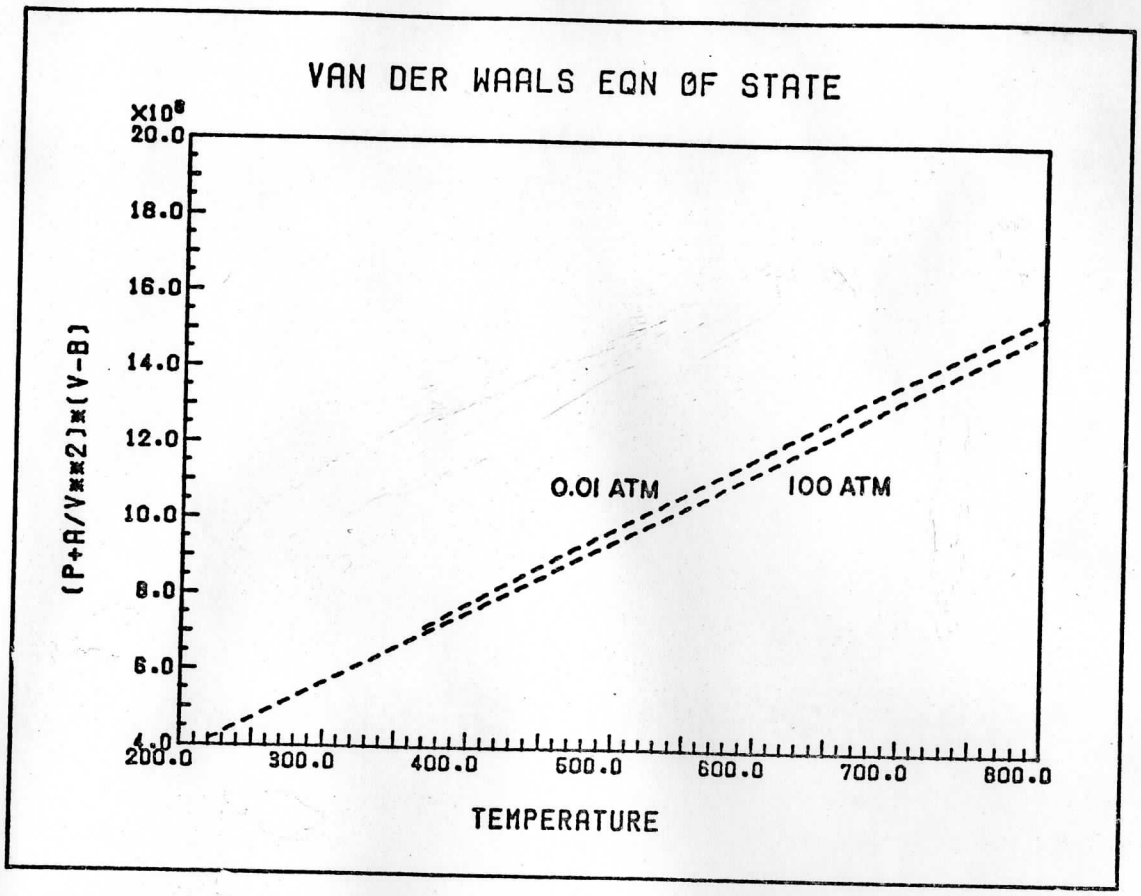
VAN DER WAALS EQN OF STATE
X10⁶
20.0
18.0
16.0
14.0
12.0
10.0
8.0
6.0
4.0
(P+A/V**2)*(V-B)
0.01 ATM
100 ATM
200.0
300.0
400.0
500.0
600.0
700.0
800.0
TEMPERATURE

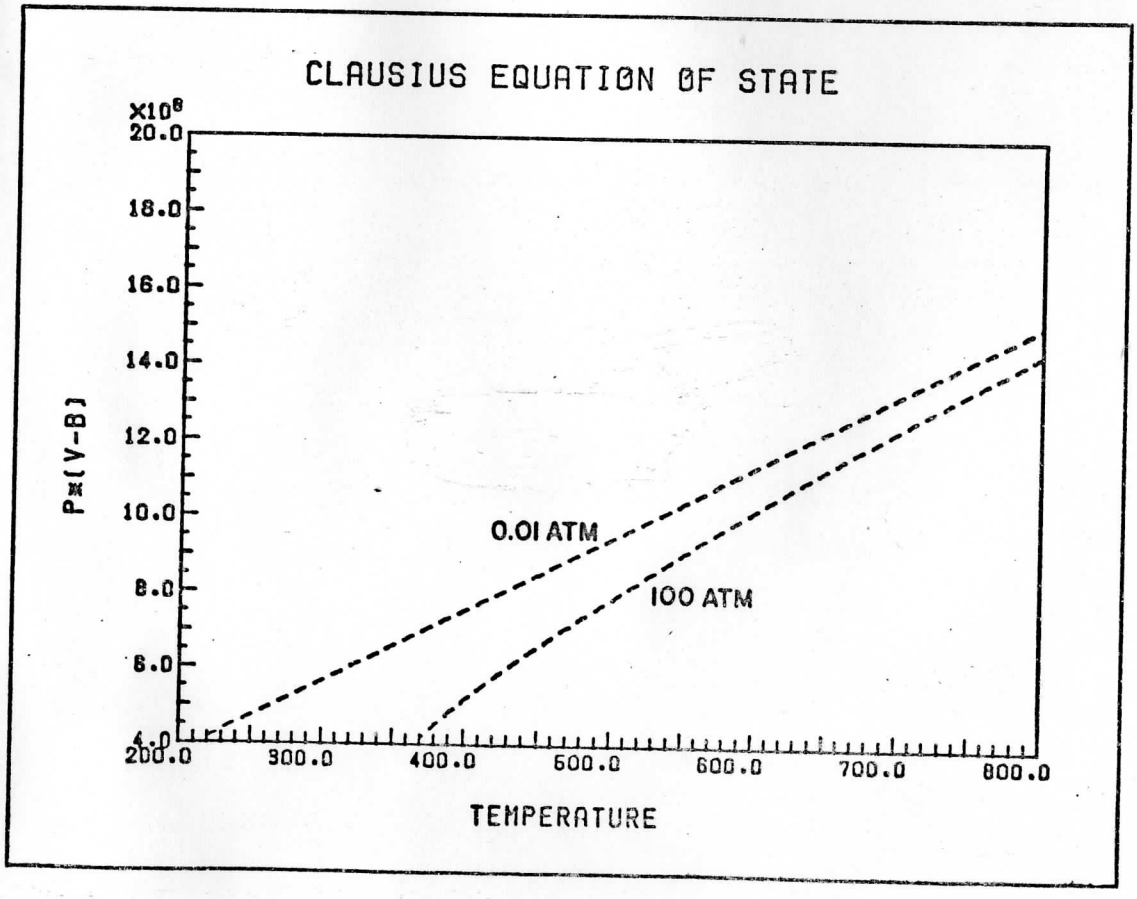
CLAUSIUS EQUATION OF STATE
X10⁶
20.0
18.0
16.0
14.0
12.0
10.0
8.0
6.0
4.0
P*(V-B)
0.01 ATM
100 ATM
200.0
300.0
400.0
500.0
600.0
700.0
800.0
TEMPERATURE

Figure 2

DRY ADIABATIC DIAGRAM FOR 100 PERCENT CARBON DIOXIDE ATMOSPHERE AND CLAUSIUS EQN. OF STATE

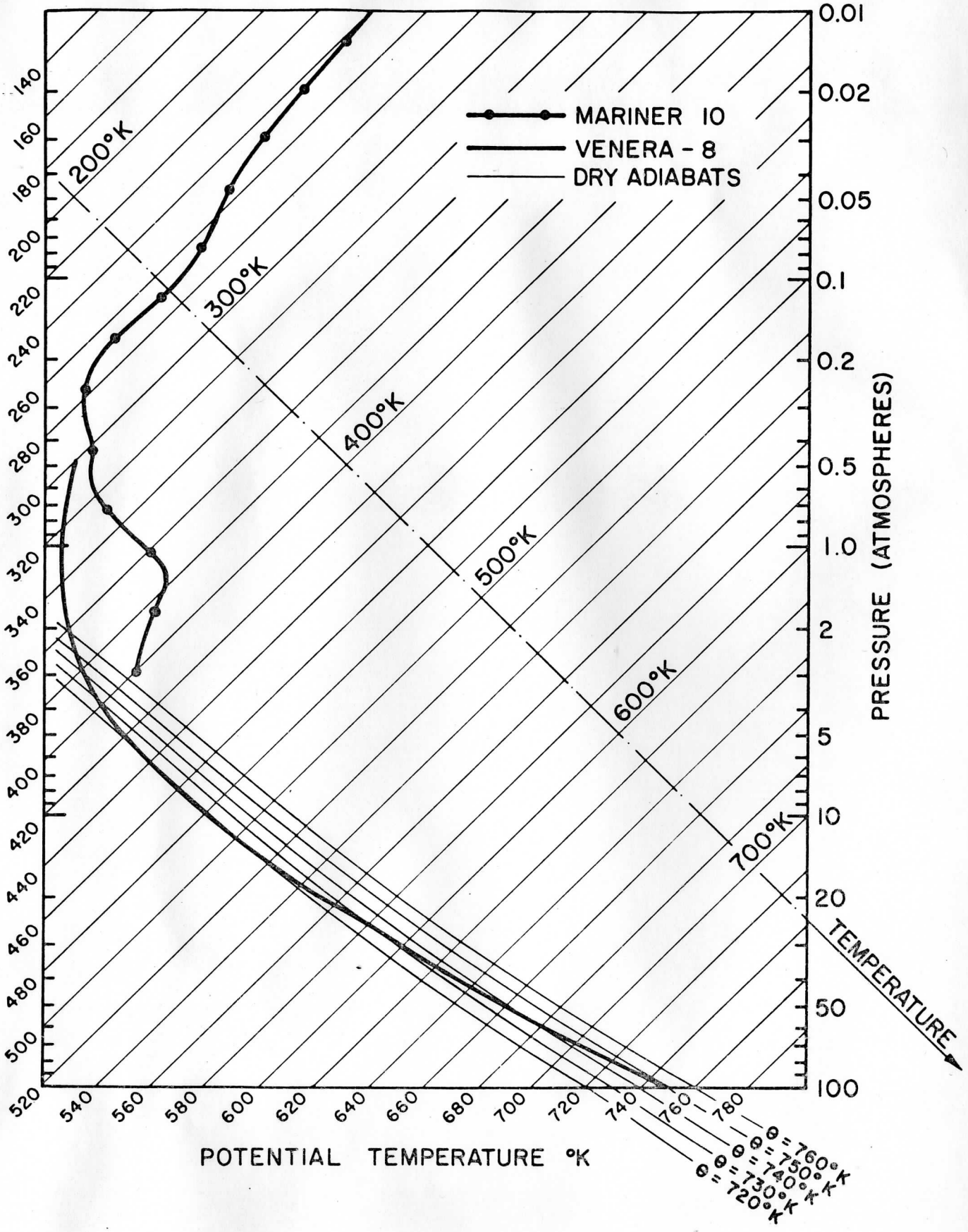

Figure 3

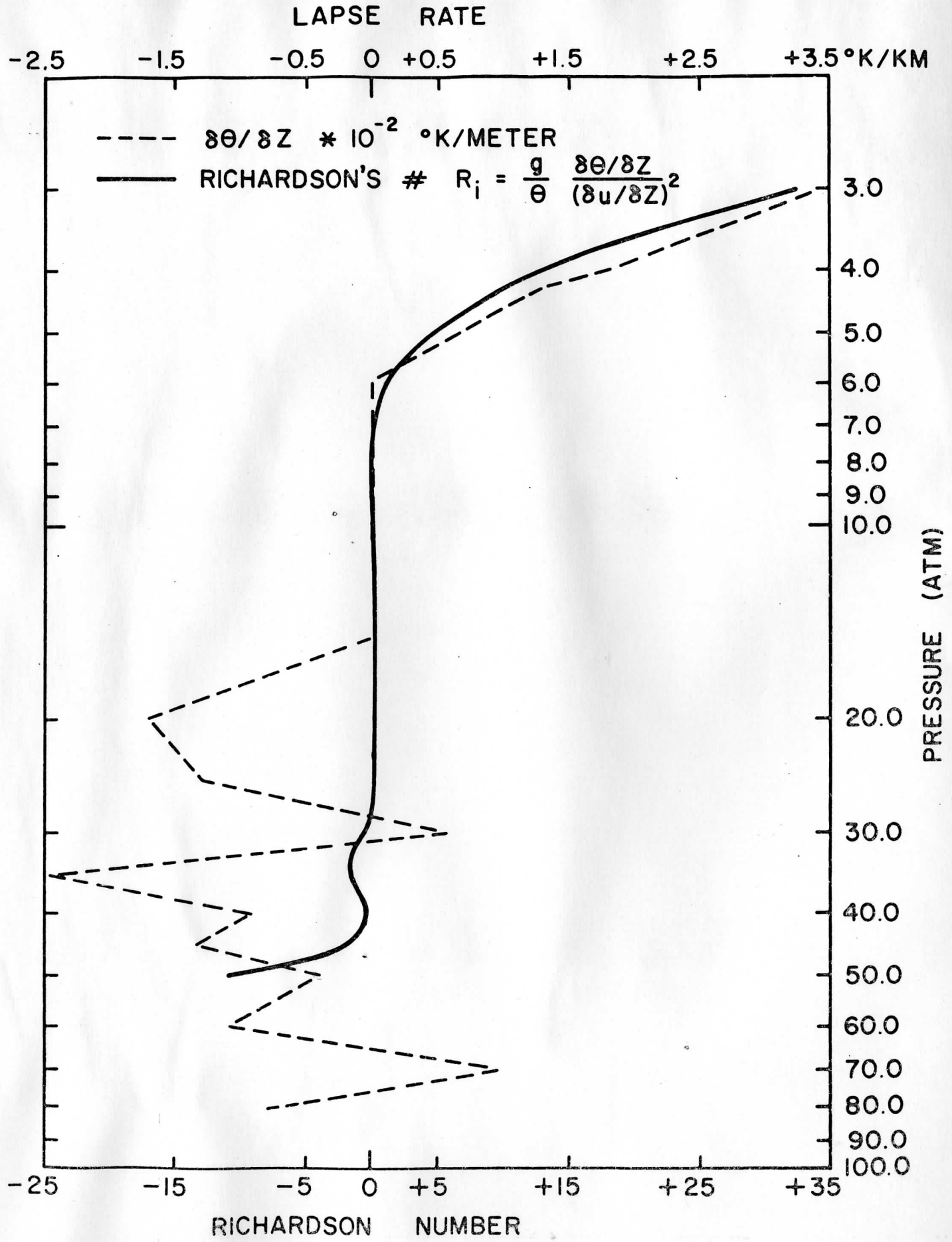
LAPSE RATE
-2.5 -1.5 -0.5 0 +0.5 +1.5 +2.5 +3.5 °K/KM
---- δθ/δZ * 10^-2 °K/METER
—— RICHARDSON'S # R_i = g/θ (δθ/δZ)/(δu/δZ)^2
3.0
4.0
5.0
6.0
7.0
8.0
9.0
10.0
20.0
30.0
40.0
50.0
60.0
70.0
80.0
90.0
100.0
PRESSURE (ATM)
-25 -15 -5 0 +5 +15 +25 +35
RICHARDSON NUMBER

Figure 4